On the improvement of regional hyperthermia treatment

Hugo Kroeze

ii

Colofon:
This text was set using the freely available LaTeX 2$_\varepsilon$ typesetting and text formatting system. The line drawings were made using the freely available METAPOST program.

The cover shows two slices of the anatomy and the temperature distribution in a patient model in the cavity slot applicator. The isotemperature surface indicates a temperature of 42°C.

On the improvement of regional hyperthermia treatment

Over de verbetering van regionale hyperthermie behandeling
(met een samenvatting in het Nederlands)

door
Hugo Kroeze
geboren op 4 augustus 1955 te Naarden

Contents

Chapter 1

General introduction

The treatment of cancer, i.e. malignant cell growth, aims at removal or killing of the malignant cells with minimal damage to the normal, healthy tissues. Standard modalities for cancer treatment are surgery, radiotherapy and chemotherapy. The results of these standard treatments are not always adequate; in 1992 the relative five year survival for adult cancer patients in the Netherlands was $47 \pm 26\%$ (Cleton et al., 1999), with a maximum of 82% for ovarian cancer and a minimum of 6.8% for pancreatic cancer. Consequently there is ongoing research into new and additional treatment modalities with the aim of improving long time cancer survival. An auspicious candidate for the improvement of cancer therapy is hyperthermia. Clinical Hyperthermia is defined as the artificial increase of tissue temperature to a value ranging from 40°C to 45°C. It is primarily administered in combination with other treatment modalities, like radiotherapy and chemotherapy. The biological rationale of these combined therapies has been studied extensively (Konings, 1995; Dahl, 1995), and is subject of ongoing research.

Virtually all physical means available for the *in vivo* heating of tissue have been investigated, leading to the development of a wide variety of clinical heating devices. However, these devices are still characterized by unsatisfactory thermal dose distributions (Lagendijk, 2000). Most tumour sites are difficult to treat with present day hyperthermia devices, while dosimetry studies indicate that the temperature distributions reached are highly inhomogeneous and that it is almost impossible to obtain the protocol temperature goals (among many others: Oleson et al. (1993); Seegenschmiedt *et al.* (1994); Prionas *et al.* (1994); Ryan *et al.* (1994); Emami *et al.* (1996); Hand *et al.* (1997); Wust *et al.* (1998b); Raaymakers *et al.* (2001)).

Most clinical studies and trials that have been executed with favourable results concern the application of superficial and regional radio-frequent heating techniques (Overgaard *et al.*, 1995; Vernon *et al.*, 1996; Van der Zee *et al.*, 2000; Harima *et al.*, 2001).

Major progress has been made in the development of computer models that can be used to simulate the power deposition of heating techniques and the induced temperature elevation in the human body (Lagendijk, 2000). Due to the limited in vivo temperature data (thermometry) available, the clinical limitations and potentials of hyperthermia can only be understood with the help of hyperthermia treatment planning. Hyperthermia treatment planning is needed to design, control, document and evaluate a treatment and thus to provide the data for treatment optimization and to provide the insight to design better heating equipment (Emami *et al.*, 1991b; Raskmark *et al.*, 1994a; Lagendijk *et al.*, 1995a; Hornsleth, 1996; Wust *et al.*, 1996; Sneed *et al.*, 1998).

This thesis addresses the use of electromagnetic and thermal simulation tools in order to investigate improvements in radio-frequent regional hyperthermia applicator devices and treatment techniques.

1.1   Hyperthermia physics

Various modalities are available to heat tissue *in vivo*. The selected method depends on the location and the volume to be treated.

Whole body hyperthermia can be initiated using infra-red radiation, whereupon the increased metabolism and isolating blankets further elevate and maintain the increased body temperature (Berry *et al.*, 1997; Robins *et al.*, 1997; Westermann *et al.*, 2001). Extremities can be heated by isolating the perfusion in a limb and recirculating the blood through a heating device (Gantenberg *et al.*, 2001).

The most straight forward method to induce a local temperature elevation in tissue is by means of thermal conduction. Catheters circulated with hot water can be inserted in the target region (Brezovich *et al.*, 1989; Schreier *et al.*, 1990). It is also possible to introduce ferro-magnetic seeds in a tumour, that are heated by an externally applied RF magnetic field with a typical frequency of 500 kHz (Stauffer *et al.*, 1984; Mack *et al.*, 1993; Van Wieringen *et al.*, 1997). This interstitial heating can also be obtained by microwave, radio frequent or ultrasonic electrodes (Corry *et al.*, 1982; Prionas *et al.*, 1989; Ryan, 1991; Diederich and Hynynen, 1993). Interstitial hyperthermia (IHT) techniques are, however, limited to very small regions and produce extreme heterogeneous temperature distributions (Crezee *et al.*, 1991; Van der Koijk *et al.*, 1997; Van Wieringen *et al.*, 1998). IHT systems without spatial control of the temperature distribution dramatically failed in the phase III RTOG trial on persistent tumours (Emami *et al.*, 1996). New 3D controlled IHT systems based on capacitively coupled segmented RF electrodes (Lagendijk *et al.*, 1995b; Van der Koijk *et al.*, 1996), segmented ultrasound electrodes (Deardorff *et al.*, 1998) or Curie point controlled thermal seed systems (Van Wieringen *et al.*,

1996; Cetas *et al.*, 1998) are being tested. These 3D interstitial systems may provide better temperature control provided that the perfusion is not too high and at the cost of severe invasiveness (Raaymakers *et al.*, 2001; Van Vulpen *et al.*, 2002c).

Mechanical resonation, induced by ultra-sound applicators that are located externally of the body (Corry *et al.*, 1982; Hynynen, 1995) is also applied as heating modality. The technique is, however, limited by a poor penetration depth, especially in bone, and restricted to very small volumes (McGough *et al.*, 1992).

Radio frequent electromagnetic radiation is one of the most versatile hyperthermia modalities; absorption of the electromagnetic energy in tissue causes a temperature elevation. Unfortunately, the spatial control of microwave and radio frequency systems is limited due to physics. At higher frequencies (434-915 MHz) some control is possible but penetration depth is extremely limited (1-2 cm) while at the lower frequencies (f<150 MHz) with higher penetration depths, spatial control is limited due to the significant wavelength (Lee et al. 1995); control is impossible at a scale less then half a wavelength, with the wavelength in muscle tissue at 146 MHz of about 23 cm.

As a consequence microwave radiation is suitable for heating superficial tumours (Lee, 1995), where frequencies from 70 MHz up to 110 MHz are used to heat more deeply located tumours with an external antenna array. Due to the longer wavelength used in the latter method, a relatively large region is heated, hence the method is called regional hyperthermia. At still lower frequencies the coupling mode between the applicator and the patient becomes capacitive. By placing the patient between two or more capacitor plates connected to a low frequency (8-27 MHz) generator, a larger region can be heated (Kato *et al.*, 1985; Van Rhoon *et al.*, 1992).

1.2   Regional hyperthermia

Regional hyperthermia applies mainly to tumours in the pelvic region, like cervix, bladder, prostate and rectal carcinomas. The tumour target temperature in regional hyperthermia treatments is 42-43°C (Lagendijk *et al.*, 1998), the typical treatment duration is one hour. The feasibility of regional hyperthermia in the pelvic region has been confirmed in several clinical studies (Van Es *et al.*, 1995; Rietbroek *et al.*, 1996, 1997; Rau *et al.*, 1998; Harima *et al.*, 2001). In a randomized trial accomplished by the Dutch Deep Hyperthermia Group a significant increase in the 3-year overall survival and 3-year local control was found in patients with advanced cervical tumours treated with a combination of radiotherapy and hyperthermia (Van der Zee *et al.*, 2000; Van der Zee and Gonzalez Gonzalez, 2002). Clinical regional hyperthermia is restricted by the occurrence of acute toxicities,

that limit the attaining of the tumour target temperatures. Hot spots, i.e. small regions that reach very high temperatures, cause local pain that can be treatment limiting (Emami *et al.*, 1991a; Anscher *et al.*, 1997). Subcutaneous burns and skin blistering (Van der Zee *et al.*, 2000) and peripheral neuropathy and myonecrosis (Ben-Yosef *et al.*, 1992) have been reported as regional hyperthermia toxicities. Due to the large heated volume, a rise of the systemic temperature can not be avoided. Although this sustains the elevation of the tumour temperature, it can also cause general discomfort and systemic stress of the patient (Van Es *et al.*, 1995), that might limit the treatment temperature or duration. Both local and systemic problems limit regional hyperthermia treatment.

1.3   Regional hyperthermia techniques

Regional hyperthermia can be applied by radiative and capacitive techniques.

The Thermotron RF8 system (Yamamoto VINITA Co., Osaka, Japan) is a capacitive heating device operating at 8 MHz, where the patient is placed between two electrodes connected to a high power RF generator (Tanaka *et al.*, 1981; Kato *et al.*, 1985; Song *et al.*, 1986). The patient is coupled to the electrodes with bolus bags, containing saline water at low temperature. Capacitive regional hyperthermia is characterized by a limited steering capacity and due to its $\vec{E}$-field orientation by extensive heating of superficial fat layers (Hiraoka *et al.*, 1987; Rhee *et al.*, 1991; Tomimatsu *et al.*, 1999a,b). The Thermotron RF8 device is mainly in use in Asian countries

Radiative applicators for regional hyperthermia create an $\vec{E}$-field parallel to the long body axis. In these devices the patient is coupled to one or more radiating antennas by means of a water bolus. The BSD-2000 SIGMA 60 applicator (Turner and Schaeffermeyer, 1989) and the the Amsterdam 4 Waveguide applicator (Van Dijk *et al.*, 1989) are systems with a single ring of antennas, that is positioned around the tumour. Water filled bags are placed between the antenna ring and the patient, comprising a closed water bolus. The Utrecht Coaxial TEM system (De Leeuw and Lagendijk, 1987) consists of a single, ring shaped antenna that is located around a water filled tube that contains the patient. This type of applicator is called an open water bolus system. The limited length of the water bolus of closed systems can cause local pain in the upper thighs due to fringing fields at the bolus edge (Jia *et al.*, 1994). The absence of cooling water between the legs and other air pockets between the skin and the bolus bags can give rise to local hot spots, especially in the perineal area. The weight of the bolus bags might also cause patient discomfort. In close water bolus systems, the patient is in a comfortable, horizontal position. In an open water bolus, the free flowing water provides an optimal skin cooling, avoids air pockets and eliminates the pressure

from the bolus bags. The large skin contact area allows influencing the systemic temperature by changing the bolus temperature (De Leeuw *et al.*, 1999). The half erect position of the patient can, however, cause fatigue in the legs and attribute to general discomfort. Due to the confinement of the patient in the tube holding the water bolus, some patients may experience claustrophobia.

The radiative field orientation avoids heating of the superficial fat layer (Johnson and Guy, 1972). It also allows optimal interference of the wave fronts centrally in the body. Systems with more than one antenna can relocate the interference maximum, i.e. focusing of the absorbed power in the tumour, by changing the relative phase and amplitude of the exiting voltages of the individual antennas (Paulsen *et al.*, 1984; Turner and Schaeffermeyer, 1989). In this case the applicator behaves as a phased array antenna. Phase/amplitude control of the power deposition pattern can also be used to avoid treatment limiting hot spots in normal tissue (Sullivan *et al.*, 1993; Wust *et al.*, 1996). The Coaxial TEM applicator has only one antenna, phase/amplitude control of the power deposition pattern is not feasible; transversal steering can be accomplished by shifting the patient (De Leeuw *et al.*, 1991).

1.4   Hyperthermia modelling techniques

Correct selection of the phase parameters of the antennas for optimal tumour heating can not be done with simple path length calculation (Sullivan *et al.*, 1993), due to the complex dielectric structure of the body. A numerical model, based on the Maxwell equations, has to be used to compute the $\vec{E}$-field of the individual antennas (Paulsen, 1990; Sullivan, 1991; Zwamborn *et al.*, 1991; Wust *et al.*, 1993; Van de Kamer *et al.*, 2001a) and derive an optimal phase/amplitude setting (Nikita *et al.*, 1993; Bardati *et al.*, 1995). After complex addition of the $\vec{E}$-fields, the power density (in $\mathrm{W\,m^{-3}}$) or the Specific Absorption Rate (SAR, in $\mathrm{W\,kg^{-1}}$) distribution can be calculated in the patient volume. In the next step the temperature distribution can be computed from the power density distribution, using a thermal model (Pennes, 1948; Mooibroek *et al.*, 1993; Kotte, 1998).

The combined use of these numerical models allow the planning of a hyperthermia treatment, including the possibility of optimizing the treatment by adjusting treatment parameters. At our institute such an integrated treatment planning system has been developed (Kotte, 1998; Van de Kamer *et al.*, 2001a) and is regularly used to evaluate hyperthermia treatments with the Coaxial TEM system, to guide the spatially controlled interstitial hyperthermia treatments (Raaymakers *et al.*, 2001; Van Vulpen *et al.*, 2002c)and to act as an evaluation tool in various design and (mobile telephone and MRI) safety studies (Van Leeuwen *et al.*, 1999, 2000a; Hand *et al.*, 2000, 2001). The electromagnetic simulation tool is based on the

FDTD method (Yee, 1966; Taflove, 1995), extended with a quasi static zooming option to allow high resolution modelling (Van de Kamer *et al.*, 2001b, 2002a). The thermal simulation tool is based on a finite difference solution of the bioheat equation including all relevant vasculature (Kotte *et al.*, 1999; Raaymakers *et al.*, 2000; Van Leeuwen *et al.*, 2000b; Craciunescu *et al.*, 2001).

Hyperthermia treatment planning systems are of major importance in the design and evaluation of new applicator types, modifications of existing types and comparison of competing heating modalities. Without numeric modelling this is only possible in homogeneous phantoms and after the cumbersome construction of a prototype applicator.

3-D simulations, especially the electromagnetic models, require a large computational effort and a considerable amount of RAM, when executed at a resolution better than 1 cm^3. Developments in recent years, however, have enabled hyperthermia treatment planning with desktop computers. Hyperthermia treatment planning is still hampered by inherent restrictions in imaging devices, like the limited slice thickness in CT imagers and the difficulty of obtaining reliable perfusion data and the tracking of vessels with any imaging modality. Even with correct perfusion data, one has to deal with the change in perfusion rate due to the local and systemic effect of the temperature elevation. None of the imaging modalities make a direct measurement of the dielectric properties of the patient tissues, so they have to be attributed to the several tissue types based on literature data (Gabriel *et al.*, 1996). This data shows a large variety, however, this is only of limited influence on the simulated SAR distribution (Van de Kamer *et al.*, 2001e). The difference in patient posture in the imaging device and in the hyperthermia applicator is a further cause of deviations between simulation results and physical reality.

1.5   Development and improvement of regional hyperthermia

The first generation phased array regional hyperthermia applicators were single ring systems without any phase control (Turner, 1984). Newer versions allowed transversal control of the interference maximum only (Turner and Schaeffermeyer, 1989). Longitudinal control of the power deposition could only be accomplished by shifting the patient in the applicator. Several authors have shown that adding more rings of antennas to the applicator can improve longitudinal SAR control and enhance the ratio of SAR in the target volume with respect to the rest of the patient (Paulsen *et al.*, 1999) (this thesis) and increase the tumour temperature (Wust *et al.*, 1996). A three ring applicator with four dipole pairs per ring and a closed water bolus is commercially available as the BSD-2000 SIGMA Eye system (Turner, 1999; Turner *et al.*, 2000).

The operating frequency of regional hyperthermia applicators was selected as a compromise between penetration depth and the size of the interference maximum. Low frequency waves have a better penetration (Johnson and Guy, 1972), where a high frequency, i.e. a lower wavelength results in a smaller central maximum. Paulsen *et al.* (1999) investigated the use of frequencies up to 200 MHz and found advantageous performance at 150 MHz for central locations and at 200 MHz for more superficial tumour sites.

Successful regional hyperthermia treatment depends equally on the ability to heat the tumour and to avoid hot spots in normal tissue. Hot spots originate in tissue inhomogeneities and can only be studied in a structured patient model. Wust *et al.* (1996) found that in a three ring applicator system a significant hot spot reduction is possible without reduction of the tumour temperature.

A useful technique to reduce the treatment limiting effects of superficial hot spots in applicators without phase/amplitude control options is the use of absorbing structures (De Leeuw *et al.*, 1994; Van Vulpen *et al.*, 2002a). Detailed analysis of the effects of an absorbing structure, using simulation tools, might lead to improvement of its efficacy by modification of shape and/or composition.

Despite the ongoing development in radiative regional hyperthermia, the Thermotron RF8 capacitive applicator remains in wide use. In Japan alone more than 40 devices are in function. The performance of the RF8 applicator has been analyzed mainly in homogeneous agar phantoms (Kato *et al.*, 1985, 1997; Tomimatsu *et al.*, 1999a,b). No treatment planning system for capacitive regional hyperthermia is readily available. This implies that no comparison can be made in a heterogeneous patient model between capacitive and radiative applicators. This matter is of importance to guide the development of a new applicator type for the Asian market.

1.6   Outline of this thesis

The aim of this thesis is to address some issues that are connected to the improvement of regional hyperthermia treatment with the use of numerical simulation tools.

Absorbers may be useful in reducing treatment limiting hot spots. Basic aspects of the effect of rectangular, homogeneous absorbers are discussed in Chapter 2. The influence of the size and the salinity of the absorbers is investigated, both on a phantom and on a patient model.

In Chapter 3 design aspects of an improved applicator with a multi ring annular array of antennas and an open water bolus are treated. The structure of the

new applicator is aimed at a more comfortable posture of the patient and optimal use of phase/amplitude control of the SAR distribution. A cavity slot antenna is introduced to enhance the directivity and reduce mutual coupling between the antennas. Several design parameters, i.e. dimensions, number of antennas and operating frequency, are evaluated using several patient models. The influence of the patient posture on the development of hot spots is investigated.

The absorber described in Chapter 2 couples a reduction of the SAR centrally under the absorber to an increase of SAR under its edge. Reduction of this edge effect of absorbers by modification of its shape, position and composition is discussed in Chapter 4.

In Chapter 5 a treatment planning system for capacitive hyperthermia, based on previously designed simulation tools is introduced. The planning system is validated by comparison to the analytic solution of a phantom problem. Comparison of SAR distributions in a patient shaped agar phantom and a structured patient model reveals a shielding effect of the bony structures. It is shown that evaluation of capacitive hyperthermia with agar phantoms leads to overly optimistic conclusions.

In Chapter 6 the performance of the Thermotron RF8 applicator and the proposed open water bolus, cavity slot applicator operating at 150 MHz, is compared, using an Asian patient model. The performance of the RF8 applicator is improved by the use of very cold overlay boli with a suitable salinity. Both SAR and temperature distributions demonstrate the improved performance of the radiative applicator and the advantages of phase/amplitude control.

A summary and general conclusion are presented in Chapter 7.

Chapter 2

The Use of Absorbing Structures During Regional Hyperthermia Treatment

Abstract Local pain is the main factor that limits regional hyperthermia treatment. Using the SAR model of the regional hyperthermia treatment planning system, the capability of absorbing blocks to reduce peripheral hot spots was investigated. The effect of rectangular absorbers of various size and salinity on an elliptical phantom in the Coaxial TEM was evaluated. The computed results were compared with SAR values measured in the phantom. Absorbers of $9 \times 9 \times 4$ cm^3 and a salinity of 18 gram$\,l^{-1}$ provide a SAR reduction in the muscle equivalent material, centrally under the absorber of at least 50% at a depth of up to 3 cm. The effect on the central (i.e. tumour) region is less than 20%. Larger absorbers have a more global effect and cause more attenuation in the central region. The attenuating effect depends strongly on the thickness of the fat layer between muscle and absorber. More than 2 cm fat limits the effective use of absorbers. Absorbers can induce a significant increase of SAR in muscle and fat near their edges. This effect also depends on absorber size and salinity and the thickness of the fat layer. The effect of an absorber was also evaluated with a patient anatomy, yielding results in agreement with the phantom experiments.

2.1   Introduction

The beneficial effect of regional hyperthermia combined with external radiotherapy on pelvic tumours was recently confirmed in randomized trials (Harima *et al.*, 2000; Van der Zee *et al.*, 2000). This major result was obtained despite the fact that other studies show that the majority of hyperthermia treatment sessions are still power limited, mainly due to discomfort (Rau *et al.*, 1998) or localized pain (Dinges *et al.*, 1998) caused by hot spots. Wust *et al.* (1999) reported that in more than 80% of all patients, treatment limiting hot spots occur. The hot spots are mainly located peripherally, inducing for instance subcutaneous burns and skin blistering (Van der Zee *et al.*, 2000) or pain at the symphysis pubica, the crest of the pelvic bone or the lumbo-sacral region (Wust *et al.*, 1999), or peripheral neuropathy and myonecrosis (Ben-Yosef *et al.*, 1992).

The hot spot phenomenon occurs in various intensities with all type of applicators: the BSD-2000 SIGMA 60 applicator (Turner and Schaeffermeyer, 1989), the Amsterdam 4 Waveguide system (Van Dijk *et al.*, 1989) and the Utrecht Coaxial TEM (De Leeuw and Lagendijk, 1987). The Coaxial TEM is a single antenna applicator with limited Specific Absorption Rate (SAR) steering capacity (De Leeuw *et al.*, 1991). By shifting the patient in the aperture area, the SAR pattern can be globally changed, but not fine enough to avoid hot spots without seriously affecting the SAR in the tumour. The Coaxial TEM system reduces the occurrence of water bolus edge related hot spots by its open water bolus at the cost of more systemic stress (Van Es *et al.*, 1995). Phased array applicators with a multi ring antenna arrangement have the theoretical potential to optimize the SAR distribution. This phase amplitude control can to some extent be used to diminish hot spots (Wust *et al.* (1996); Paulsen *et al.* (1999) and Chapter 3). Compared to phase amplitude controlled systems, our Coaxial TEM system has a more limited SAR steering capacity due to its uniform aperture field (De Leeuw and Lagendijk, 1987).

Because hot spots are highly anatomy dependent (Van de Kamer *et al.*, 2001d) and mainly superficial, it is argued that 'manipulation' of the outer patient anatomy might serve as an alternative means to suppress hot spots. With manipulation is meant the placement of pieces of absorbing material at or near the skin. Clinical experience shows that positioning of small plastic bags filled with a saline solution or solidified blocks of saline water on the 'hot spots' in most cases resulted in pain relief (Van Vulpen *et al.*, 2000), allowing treatment continuation at the same power level without affecting the tumour temperature. The open water bolus of the Coaxial TEM system allows easy placement of these absorbing structures inside the water bolus during treatment. Absorbers can be placed, on an *ad hoc* basis, if the patient experiences pain. The absorbing structures used in this study might also have applications in phase amplitude controlled applicator systems.

This study investigates the effect of absorbing structures, placed on the skin of

the patient, on the SAR distribution locally, near the absorber, and globally, with emphasis on the central tumour location.

To study the effect of absorbers quantitatively, the absorbed power distributions were studied using the FDTD SAR model of the hyperthermia treatment planning system (Van de Kamer *et al.*, 2001a). Results were verified by comparing the measured E-field in a phantom along a track under an absorber with an FDTD computation. Finally, the use of an absorber was demonstrated on a realistic patient anatomy with the FDTD SAR model.

2.2   Methods

2.2.1   Coaxial TEM

The Coaxial TEM system has been described extensively by De Leeuw and Lagendijk (1987). The system is characterized by a circumferential radiating aperture surrounding a water filled plastic tube with a diameter of 60 cm. The patient is inserted into the open end of the tube laying on a stretcher and is positioned with the pelvic area in the central aperture plane using a shifting mechanism. The open end of the bolus allows easy access for placement of absorbing elements during treatment. The Coaxial TEM operates at 70 MHz.

2.2.2   Absorbing structures

The absorbers described in this paper are blocks of saline water that is solidified with agar. Agar is a polysaccharide complex made out of dried seaweed (gracilaria or gelidium) and is available in powder form as food additive (E406). Absorber blocks are made by boiling a sufficient amount of distilled water, and adding the required amount of NaCl and 40 gram l^{-1} agar under continuous stirring. The mixture is poured in a suitable mould to cure. The material has a soft, solid appearance and can be cut to the desired size. To prevent migration of NaCl to the surrounding bolus water, the absorber is wrapped in a thin polyethylene cover.

Table 2.1: Dielectric properties of absorbers at 30°C and 70 MHz.

Salinity (gram l^{-1})	Dielectric properties	
	ε_{r}	σ(S m^{-1})
9	73.7	1.71
18	70.9	3.33
36	65.7	6.33
72	56.8	11.7
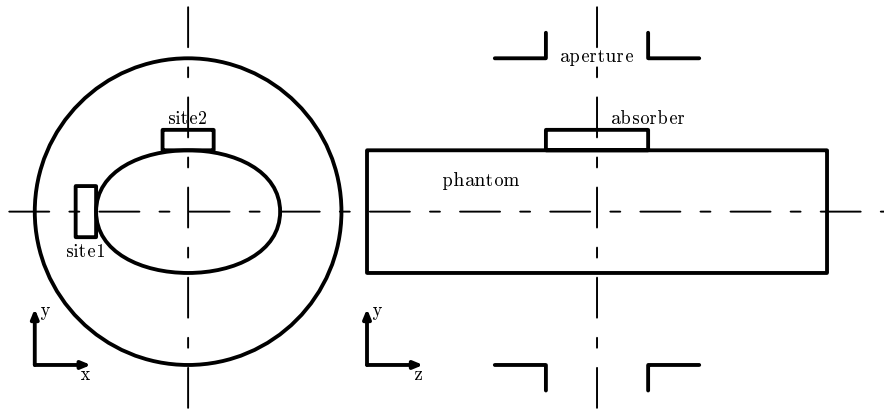
Figure 2.1: Position of phantom and absorbers in the Coaxial
TEM in computational experiments.

The dielectric properties can be calculated according to Stogryn (1971), presuming
it is saline water and disregarding any dielectric effect from the agar (see table 2.1).
In this calculation, the temperature of the absorber was set at 30 °C; close to the
usual bolus temperature.

The experiments were performed with absorbers of 9 cm and 21 cm length (along z-
axis, see figure 2.1), a width of 9 cm, and a thickness of 2 cm and 4 cm, respectively.
Absorbers of 9 cm and 21 cm are also referred to as 'short' and 'long'. The salinity
of the absorbers was varied from 9–72 gram l^{-1}.

2.2.3 Hyperthermia Treatment Planning system

The regional Hyperthermia Treatment Planning (HTP) system (Van de Kamer
et al., 2001a) was used to compute SAR distributions in a phantom and a patient
anatomy with various absorbers.

The regional HTP system uses a symmetric implementation of the FDTD method
(Van de Kamer *et al.*, 2001a) using Retarded Time Absorbing Boundary Condi-
tions (RT-ABC) (Berntsen and Hornsleth, 1994). The resolution was set at 1 cm,
the time step $\delta t = 1.67 \times 10^{-11}$ s follows from the resolution and the use of the
RT-ABC. The number of iterations was set at 7000; convergence was tested by
observing the time evolution of $|\vec{E}|$ at test points in the phantom. The phantom
used in the simulations is an elliptical cylinder with a cross section of 36×24 cm^2
and a length of 97 cm (Schneider *et al.*, 1994). The dielectric properties are set at
$\varepsilon_r = 75.8$ and $\sigma = 0.48$ S m^{-1}, corresponding to a saline solution with 3 gram l^{-1}
NaCl (Stogryn, 1971). In some of the computations, the phantom was surrounded
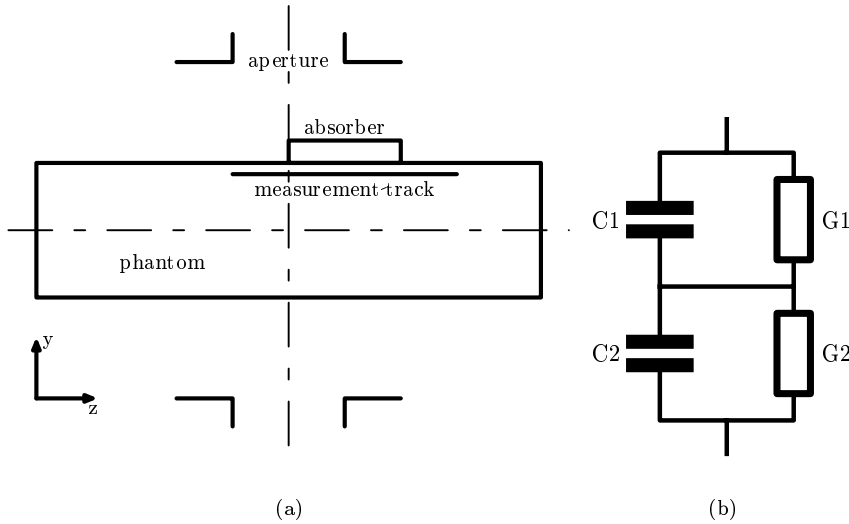
Figure 2.2: Setup of verification measurement in phantom, (a) position of absorber and measurement track, (b) representation of composite material.

by a fat equivalent layer with a thickness of 1, 2 or 3 cm, and dielectric properties of $\varepsilon_r = 10$ and $\sigma = 0.06$ S m^{-1}. Absorbing structures were placed at two locations at the phantom, called site 1 and site 2 (see figure 2.1). The patient anatomy is obtained from a 40 cm CT data set (slice thickness 5 mm) by Hounsfield Unit thresholding (Hornsleth *et al.*, 1996) and down scaling to 1 cm resolution, using the 'winner take all' algorithm (James and Sullivan, 1992). The tumour is manually outlined by a physician, as well as a volume of interest in front of the symphysis pubica, where local pain is expected. The definition of applicator, phantom and absorbing elements is done using our Generic Object Format (De Bree, 1998).

2.2.4 Phantom-absorber experiments

For verification, the axial and radial components of the $\vec{E}$-field were measured in the elliptical phantom along a track $\sim$2 cm below the anterior edge of the phantom-cover (figure 2.2(a)). The E-field measurements were performed using a diode probe (De Leeuw, 1993). The values were corrected for probe response, squared and normalized to obtain a SAR profile.

The measurement was performed with the phantom alone and with an absorber

of $21 \times 9 \times 2$ cm^3 and a salinity of 36 gram l^{-1} NaCl placed on top of the phantom, with the lower edge at the aperture mid-plane.

The measured values were compared with FDTD computations, with and without absorber. In order to create a better model of the phantom wall for the FDTD computation, the outer layer of the phantom was modelled as a composite material consisting of 2 mm plastic and 8 mm saline water. The presence of the absorber causes a local distortion of the dominant E_z-field at the edges of the absorber in the z-direction. At these locations the major $\vec{E}$-field component is normal to the plastic layer. Therefore, the composite material was considered to be equivalent to a circuit (figure 2.2(b)) of two capacitors (representing ε_r) and two conductances (representing σ). The dielectric properties of the composite material were calculated to be $\varepsilon_r = 9.86$ and $\sigma = 0.02$ S m^{-1}.

2.3   Results

2.3.1   Attenuating effect of absorbers on a phantom

Figure 2.3 shows the computed effect of a $21 \times 9 \times 4$ cm^3 absorber with a salinity of 36 gram l^{-1} at site 1 of the phantom in the transversal plane centrally under the absorber. The SAR distribution, normalized to the central maximum is shown in figure 2.3(a). The slight asymmetry in the y-direction is caused by the presence of the stretcher. Figure 2.3(b) is the SAR distribution with the absorber, normalized to the SAR without absorber. To emphasize the effect of the absorber, the ratio of the SAR distributions with absorber and without absorber is also given (figure 2.3(c)). The contour lines in the SAR ratio plot show the attenuation caused by the absorber numerically. It can be seen that directly under the absorber the local SAR is lowered to 10% of the value without absorber. About 7 cm under the absorber an attenuation of 50% is obtained. The SAR in the central region of the phantom is reduced to $80 - 90\%$. The central maximum is shifted 4 cm to the right and decreased by 10%. A slight increase of 20 % is observed 10 cm right of the central axis.

Figure 2.4 shows the effect of a $21 \times 9 \times 4$ cm^3 absorber at site 2 of the phantom. Again, one can see directly under the absorber a substantial reduction of SAR to $\sim 20\%$, gradually changing to $\sim 75\%$ centrally in the phantom. The central maximum is shifted 3 cm posterior and reduced to 77% of the central maximum without absorber (figure 2.3(a)). A remarkable increase of the SAR, up to a factor 1.7 can be observed at the lateral sides of the phantom.

Comparison with a simulation of a $9 \times 9 \times 4$ cm^3 absorber at site 2 (figures 2.5(a) and 2.5(b)) shows an equal attenuation directly under the absorber, but a more steep slope towards the centre and an absence of a significant SAR increase at
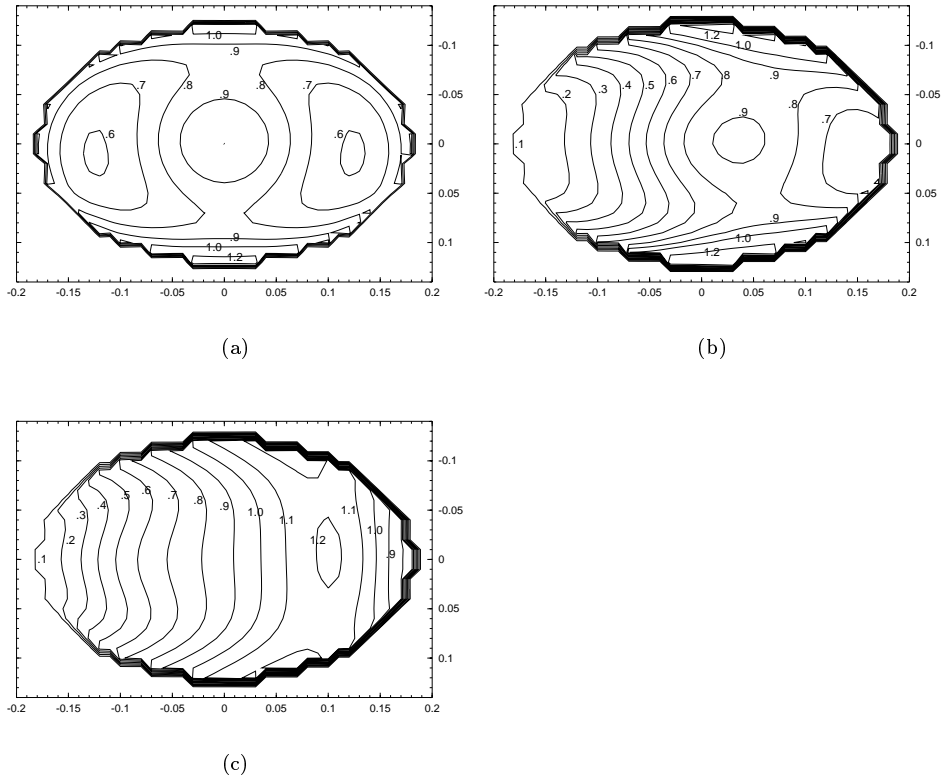
Figure 2.3: Transversal slice in the central plane of a phantom without fat layer, (a) normalized SAR distribution without absorber, (b) normalized SAR with $21 \times 9 \times 4$ cm^3 absorber (36 gram l^{-1}) at site 1, and (c) ratio of SAR with and without absorber.

(a)   (b)
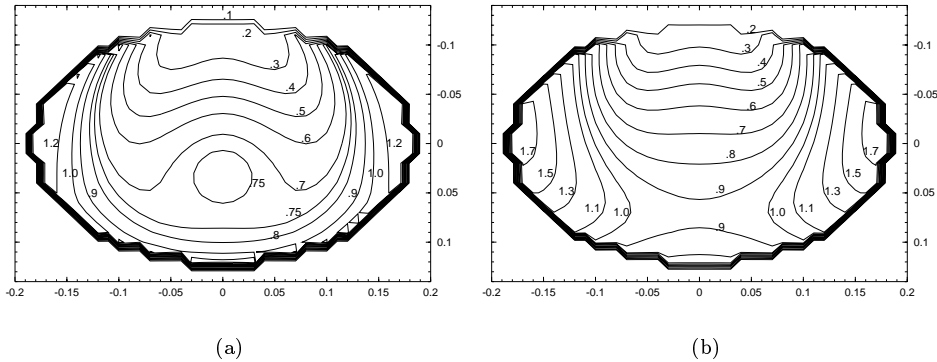
Figure 2.4: Transversal slice in the central plane of a phantom
without fat layer with $21 \times 9 \times 4$ cm^3 absorber (36 gram l^{-1})
at site 2, (a) SAR distribution, normalized to SAR with-
out absorber, and (b) Ratio of SAR distributions with and
without absorber.

the lateral sides. The influence of a fat layer is demonstrated in figures 2.5(c) and
2.5(d). A major deterioration of the attenuating effect of the absorber is observed.
However, in this case, the central maximum remains almost unaffected.

In order to further investigate the effect of absorber size and composition, the
effective depth was defined as the distance central under the absorber where the
ratio of SAR with and without absorber is 50% (Ed$_{50}$) or 75% (Ed$_{75}$). Figure
2.6 gives the computed SAR ratio central under an absorber at site 2 for various
absorber sizes and salinities, with and without the presence of a 1 cm fat layer
around the phantom.

Tabulation of Ed$_{50}$ and Ed$_{75}$ (table 2.2) illustrates the dependence of the effective
depth of absorber parameters and phantom composition.

The differences in the effective depth in a phantom without fat layer and with
1 cm fat indicate that the thickness of the fat layer has a major influence on the
attenuating effect. In figure 2.7, the SAR ratio under a $9 \times 9 \times 4$ cm^3 absorber is
shown for fat layers up to 3 cm. For fat layers of more than 2 cm, even Ed$_{75}$ is no
longer reached, limiting the effective use of absorbers.

An explanation for the lateral increase effect can be found by observing the am-
plitude of E_z along a circular track in the mid-plane of the aperture 2 cm beneath
the outer edge of the water bolus (figure 2.8). It can be seen that the presence
of a $21 \times 9 \times 4$ cm^3 absorber has a distorting effect on the $|E_z|$ distribution, where

(a)

(b)

(c)

(d)
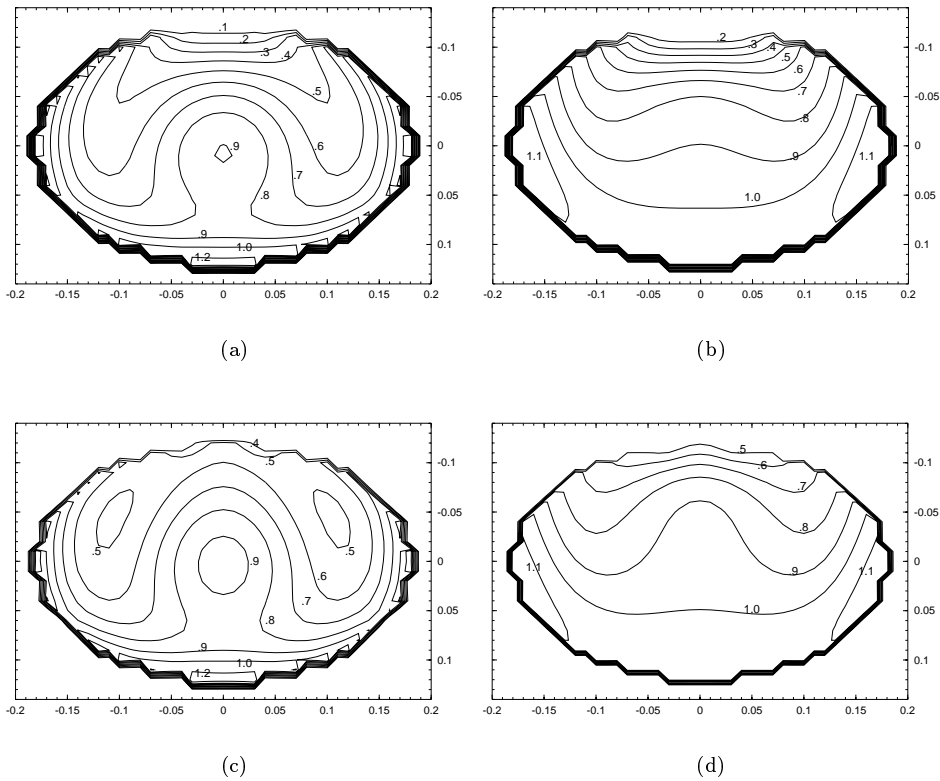
Figure 2.5: Transversal slice in the central plane of a phantom without and with a 1 cm fat layer and with a $9 \times 9 \times 4$ cm^3 absorber (36 gram l^{-1}) at site 2, (a) SAR distribution without fat, normalized to SAR without absorber (figure 2.3(a)), (b) ratio of SAR with and without absorber, phantom without fat, (c) SAR distribution with fat, normalized to SAR without absorber, (d) ratio of SAR with and without absorber, phantom with fat.

(a)

(b)

(c)

(d)
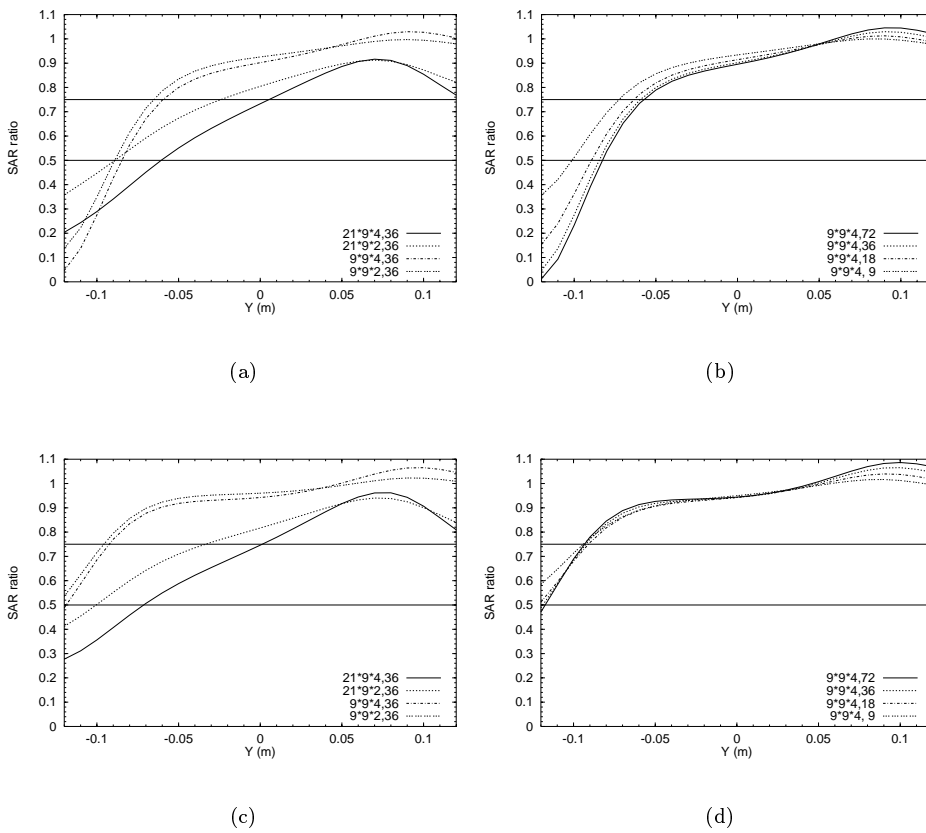
Figure 2.6: SAR ratio with absorber at site 2 along track central under absorber. Absorber size and composition is coded as: length×width×thickness (cm^3), salinity $(gram\,l^{-1})$. (a) no fat layer, influence of size, (b) no fat layer, influence of salinity, (c) 1 cm fat, influence of size, (d) 1 cm fat, influence of salinity.

Table 2.2: Effective depth (cm) of absorber at site 2. ('-' indicates that Ed_{50} is not reached).

Size (cm^2)	Thickness (cm)	Salinity $(gram\,l^{-1})$	With 1 cm fat Ed_{50}	Ed_{75}	Without fat Ed_{50}	Ed_{75}
21×9	4	36	4.9	12.0	5.9	12.5
	4	18	2.3	9.4	3.1	9.7
	2	36	2.0	8.6	2.6	9.6
9×9	4	72	0.3	2.7	3.7	6.3
	4	36	0.1	2.8	3.5	6.0
	4	18	-	2.9	3.1	5.7
	2	36	-	2.4	3.1	5.5
	4	9	-	2.6	1.9	4.7
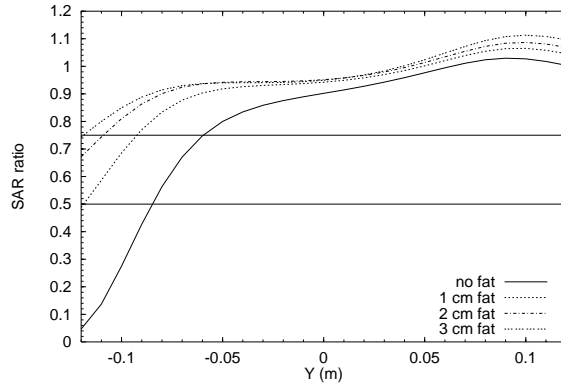
Figure 2.7: SAR ratio: influence of the thickness of the fat layer on the effective depth of a $9 \times 9 \times 4$ cm^3 absorber.

the $9 \times 9 \times 4$ cm^3 absorber causes no large deviations from the pattern without absorber.

All absorbers have a local attenuating effect, but $21 \times 9 \times 4$ cm^3 absorbers can also cause more global changes in the SAR distribution.

2.3.2   Measurement in phantom

Figure 2.9 shows the measured and computed SAR values with and without absorber in the measurement setup of figure 2.2(a). The measured values and the FDTD computation without absorber were normalized to the maximum SAR, close to the aperture mid-plane. Both the measured values and the FDTD compu-
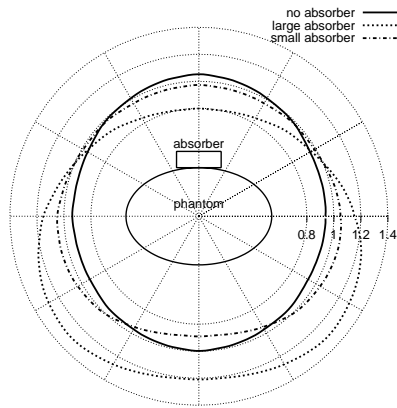
Figure 2.8: |Ez| in mid-plane aperture, illustrating the global effect of long absorbers on the field distribution.
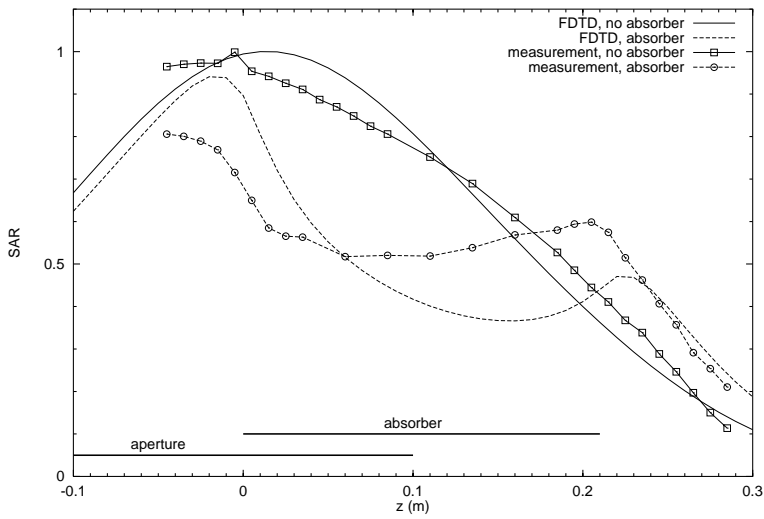
Figure 2.9: Measurements and 3D-FDTD simulation in a phantom.

tation with absorber were normalized to the SAR maximum without absorber, in order to preserve the true ratio between the profiles with and without absorber.

Comparison with a 3D-FDTD simulation shows a fair similarity with the measured results, considering the accuracy of both measurements and simulations. The measured and computed profiles without absorber agree within 10%, the match of the curves with absorber is less clear. However, the general pattern, attenuation under the absorber and some peaking at the absorber edges, is reproduced.

2.3.3 Edge effects

Unfortunately, the presence of an absorber also causes a SAR increase at the edges located in the direction of the dominant field, i.e. the Z-direction.

Figure 2.10 shows the SAR relative to the local SAR without absorber in the xz-plane under a $9 \times 9 \times 4$ cm^3 absorber. It can be seen that the absence of a fat layer enhances the edge effect, note the difference in the SAR ratio scale. Furthermore, it is clear that the maximum SAR enhancement due to the edge effect is in the $x = 0$ plane.

Figure 2.11 shows normalized SAR profiles in a phantom with 1 cm fat, along the z-axis, in the $x = 0$ plane and 1 cm under the fat-phantom boundary, with various types of absorbers applied to the phantom. The profile without absorber is normalized at $z = 0$, the other SAR curves are normalized to the SAR maximum without absorber. The influence of absorber size is depicted in figure 2.11(a), figure 2.11(b) shows the effect of absorber salinity. Short absorbers with a salinity of 36 gram l^{-1} produce an increase of SAR up to 36% at both edges, with respect to the value at the same location without absorber. This is almost independent of absorber thickness. The effect can be reduced to 22% by lowering the salinity to 9 gram l^{-1}. As expected, long absorbers cause a more elongated attenuation profile along the z-axis. The absolute value of the peaks at the edges are lower than those caused by the short absorbers, but still there is an increase of 33%.

2.3.4 Effect of absorber on the SAR distribution in a patient

Figure 2.12(a) shows a transversal slice of the anatomy of a male patient with a prostate carcinoma. A $9 \times 9 \times 2$ cm^3 absorber with a salinity of 36 gram l^{-1} is placed on the skin in front of the symphysis pubica.

In figure 2.12(b), a local SAR maximum can be observed in front of the symphysis pubica. The SAR in figure 2.12(c) is computed with an absorber. The attenuating effect of the absorber is clearly seen in the region indicated by the circle.

The edge effect can be observed in the sagittal cross section, figure 2.12(f), especially at the lower edge of the absorber (region indicated by a circle). The
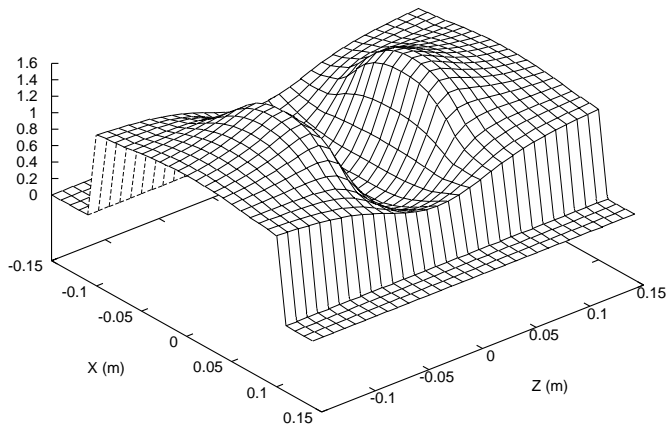
(a)
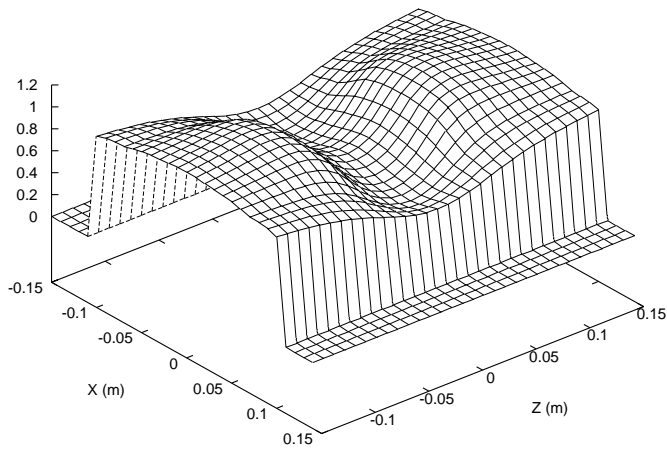
(b)

Figure 2.10: SAR ratio in xz-plane, 2 cm inside phantom material, (a) without fat layer, (b) with fat layer.
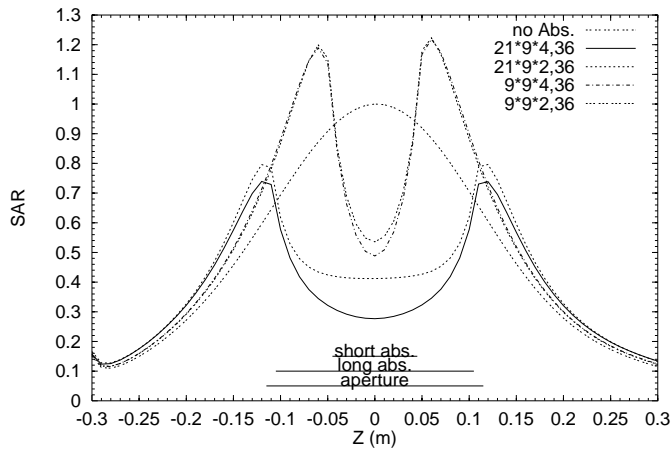
(a)
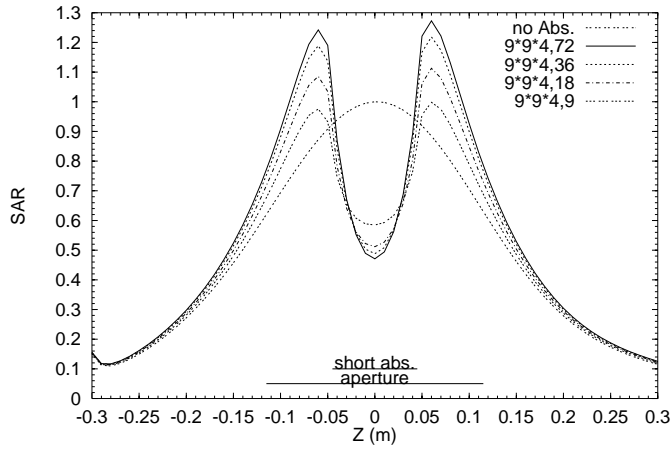
(b)

Figure 2.11: Normalized SAR along track in phantom with 1 cm fat layer, along z-axis 1 cm under fat layer. Absorber size and composition is coded as: $\mathrm{length} \times \mathrm{width} \times \mathrm{thickness}$ (cm^3), salinity $(\mathrm{gram\,l}^{-1})$ (a) influence of size, (b) influence of salinity.

(a)   (b)   (c)

(d)   (e)   (f)
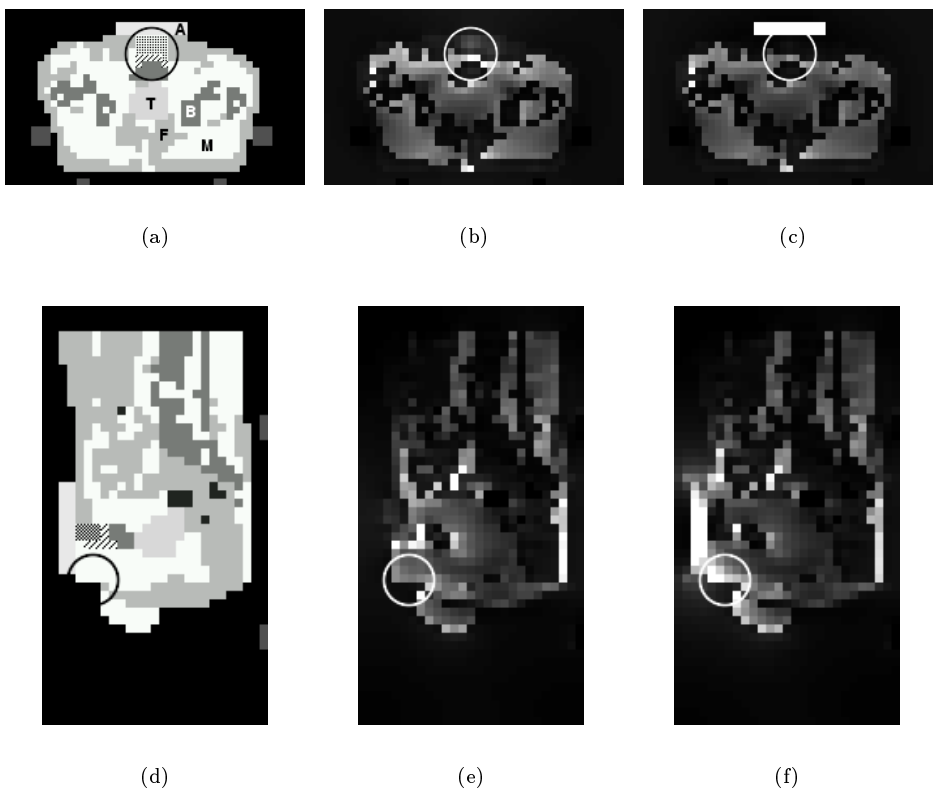
Figure 2.12: (a) Transversal slice through patient anatomy with
absorber A applied in front of the symphysis pubica, tissue
types are M: muscle, F: fat, B:bone, T: tumour; Volume Of
Interest: muscle dashed, fat dotted. Computed SAR distri-
bution in patient anatomy, (b) without absorber, (c) with
absorber. The circle indicating a hot spot corresponds with
the circle in (a). (d) Sagittal slice through anatomy (e) SAR
without and (f) with absorber. The circle indicates a SAR
increase induced by the edge effect.

tomogram (figure 2.12(d)) shows that in this region there is no fat between muscle tissue and absorber.

Numerical evaluation of the performance of both 2 cm and 4 cm absorbers is done by defining a Volume Of Interest (VOI) in front of the symphysis pubica. This volume contains both fat and muscle (see fig 2.12(a) and 2.12(d)). In table 2.3, the SAR is given for several tissues. The averaged SAR in tumour in the situation without absorber is normalized to 1, all other values are scaled with the same constant. It can be seen that the influence on the average SAR in tumour is low; a reduction to ∼80% of the value without absorber, with a slight influence of the thickness of the absorber. The SAR in muscle in the volume of interest is almost halved and in fat reduced to about a third. The influence on average SAR in the rest of the patient is negligible.

The maximum SAR in muscle in the VOI is the absolute maximum in the patient volume and a potential cause of local pain. Application of a 2 cm absorber halves the maximum in muscle and reduces both minimum and maximum in tumour to about 80%, i.e. the same ratios as observed for the average SAR. The maximum in the remaining muscle tissue, however, is almost doubled by the 2 cm absorber and even more by the 4 cm absorber. This maximum is located near the lower edge of the absorber. The maximum in the remaining fat is almost tripled by the 2 cm absorber, but the 4 cm type results in an increase of 'only' 42%.

Table 2.3: Average and maximum SAR in patient model, normalized to average SAR in tumour.

| Abs. th. (cm) | Patient (VOI excluded) | | | | | | | Volume Of Interest | | | |
| | Tumour | | | Muscle | | Fat | | Muscle | | Fat | |
	av.	max	min	av.	max	av.	max	av.	max	av.	max
0	1.00	2.96	0.31	1.08	6.29	0.26	2.38	2.88	12.67	0.68	1.24
2	0.80	2.33	0.26	1.03	12.17	0.26	7.07	1.58	6.39	0.20	0.58
4	0.76	2.28	0.25	1.01	13.58	0.26	3.38	1.43	5.60	0.16	0.51

2.4 Discussion and conclusion

This study demonstrates that absorbing structures, consisting of agar bound saline water, can reduce the SAR in peripheral muscle and fat tissue by approximately a factor 2. It was estimated that a double to threefold increase of SAR would be required to cause hot spots (Wust *et al.*, 1999), so it can be expected that a local reduction of SAR by a factor 2 is sufficient to prevent the onset of pain. This concurs with our clinical experience (Van Vulpen *et al.*, 2000).

Phantom measurements were compared to FDTD computations. The difference between measurement and computation without absorber is well within the margin to be expected, considering both the errors caused by the coarse resolution of the model and the difficulties in performing accurate $\vec{E}$-field measurements (Sullivan *et al.*, 1992; Jia *et al.*, 1994). The larger errors observed when comparing measurement and computation with absorber are mainly caused by the difficulty of correctly modelling the thin PVC wall of the phantom. Nevertheless, the general pattern of attenuation centrally under the absorber and peaking at the edges is well matched. The PVC wall is not present in the other FDTD computations to quantify the absorber behaviour, so this error source is not present in these results.

Long absorbers have an effective depth (Ed_{75}) up to 12 cm, so an attenuating effect on the central (i.e. tumour) region can be expected. Moreover, long absorbers can cause a disturbance of the global $\vec{E}$-field, resulting in SAR raise in remote regions. Short absorbers have a less penetrating effect, but the superficial effect is sufficient to obtain pain relieve. The effect on the central region is limited and global effects are small. Increasing the thickness and/or salinity of the absorbers also increases the effective depth. However, raising the salinity from 36 to 72 gram l^{-1} has hardly any additional effect, so 36 gram l^{-1} can be taken as a practical upper limit. The effective depth of a 2 cm, 36 gram l^{-1} and a 4 cm, 18 gram l^{-1} are almost equal, both for long and short types.

The presence of a fat layer between muscle-like tissue and the absorber has a major influence on the attenuation pattern. More than 2 cm fat prevents the effective use of absorbers. However, absorbers are not only used successfully on thin patients. Superficial pain is likely to occur at a bone-muscle-fat layered structure, like the symphysis pubica, the crest of the pelvic bone or the lumbo-sacral region. At these locations the fat layer tends to be thinner, so an absorber can effectively be used, even on rather stout patients.

A significant SAR increase is induced at the edges of the absorber. This edge effect depends strongly on the thickness of the fat layer. The patient example showed that the SAR maximum under the absorber was successfully attenuated, but a new SAR maximum is induced at the lower edge of the absorber. At this location, there is no fat present in the patient model, so this maximum is in agreement with the observed influence of a fat layer on the edge effect. Lowering the salinity of the absorber can diminish the edge effect to some extent, but this causes a slight reduction of the effective depth. In order to minimize the edge effect, the lowest salinity should be selected that provides sufficient attenuation in the VOI, i.e. 18 gram l^{-1}. This favours the use of 4 cm absorbers over 2 cm. Short absorbers have a higher edge effect than long absorbers, but the global effects of long absorbers makes them less suitable.

Further study has been performed to investigate the effect of modifications of

shape and/or composition of the absorber in order to reduce the edge effect whilst maintaining the effective depth. Results will be presented in a forthcoming paper.

The results presented in this study are valid for the Utrecht Coaxial TEM system. However, other radiative annular ring applicators, like the BSD-2000 SIGMA 60 and the Amsterdam 4 Waveguide system produce a similar $\vec{E}$-field in the central transversal plane Schneider *et al.* (1994). It is likely that absorbers will have a similar effect in these applicators, but the closed water bolus prevents easy placement of absorbing structures during treatment.

In general, it can be concluded that small absorbers are useful in relieving local pain during Regional Hyperthermia treatment. The absorber can be placed at the location of pain on an *ad hoc* basis. The SAR in a central tumour is not significantly affected by the use of a small absorber. The edge effect can be minimized, but not avoided by the use of 18 gram l^{-1} absorbers.

Chapter 3

Regional Hyperthermia Applicator Design using FDTD modelling

Abstract Recently published results confirm the positive effect of regional hyperthermia combined with external radiotherapy on pelvic tumours. Several studies have been published on the improvement of RF annular array applicator systems with dipoles and a closed water bolus. This study investigates the performance of a next generation applicator system for Regional Hyperthermia with a multi ring annular array of antennas and an open water bolus. A cavity slot antenna is introduced to enhance the directivity and reduce mutual coupling between the antennas. Several design parameters, i.e. dimensions, number of antennas and operating frequency, have been evaluated using several patient models. Performance indices have been defined to evaluate the effect of parameter variation on the SAR distribution. The performance of the new applicator type is compared to the Coaxial TEM. Operating frequency appears to be the main parameter with positive influence on the performance. A SAR increase in tumour of 1.7 relative to the Coaxial TEM can be obtained with a 3 ring, 6 antenna per ring cavity slot applicator operating at 150 MHz.
The effect of the patient posture in the applicator and the effect of positioning uncertainty have been examined. The bent patient posture required by the bathtub like open water bolus causes no fringing field problems at the bolus-air boundary provided a large enough applicator bore. Optimal SAR steering requires accurate patient positioning and reliable imaging in the treatment posture.

3.1   Introduction

Recently published results of randomised trials (Harima *et al.*, 2000; Van der Zee *et al.*, 2000) confirm the positive effect of regional hyperthermia combined with external radiotherapy on pelvic tumours. The hyperthermia treatments were performed in various systems: the BSD-2000 SIGMA 60 applicator (Turner and Schaeffermeyer, 1989), the Amsterdam 4 Waveguide system (Van Dijk *et al.*, 1989), the Utrecht Coaxial TEM system (De Leeuw and Lagendijk, 1987) and the Thermotron RF-8 system (Yamamoto VINITA Co., Osaka, Japan) All systems except the Thermotron RF-8 are Radio Frequency (RF) radiative annular ring applicators operating between 70 MHz and 110 MHz, the RF-8 is a capacitive system operating at 8 MHz. The SIGMA 60 and the 4 Waveguide system have the ability to transversaly steer the absorbed power distribution by controlling the phases and amplitudes of the generators feeding the individual antennas. With the Coaxial TEM transversal steering can be accomplished by shifting the patient. None of the systems has the ability of longitudinal steering, other than by shifting the patient with respect to the applicator.

Several authors have shown that adding more rings of antennas to the applicator might improve longitudinal SAR control and enhance the ratio of SAR in the target volume with respect to the rest of the patient (Paulsen *et al.*, 1999) and increase the tumour temperature (Wust *et al.*, 1996). A three-ring applicator with four dipole pairs per ring is commercially available as the BSD-2000 SIGMA Eye system (Turner, 1999; Turner *et al.*, 2000).

Paulsen *et al.* (1999) showed in a simulation study, using the Finite Element Method (FEM), and varying the number of radiating elements per ring, the number of rings and the operating frequency, that in general the performance increased with the number of antenna rings and the number of antennas per ring. An improvement in performance was observed by increasing the operating frequency to 200 MHz.

Wust *et al.* (1996) used a circular array of eight bow-tie antennas with a length of 45 cm and a diameter equal to the SIGMA-60 applicator (60 cm) and an upgraded version with the same overall dimensions, but with 3 circular arrays of antennas with a length of 15 cm. The frequency was fixed at 90 MHz. The water bolus was assumed to be of infinite dimensions. Two truncated patient models were used, with a length of 60 cm. Both patients had a rectal carcinoma defined as target volume. The Volume Surface Integral Equation (VSIE) method was used to compute $\vec{E}$-field distributions and temperature distributions were computed by numerically solving the bio-heat transfer equation. Several optimisation functions, both of SAR and temperature were evaluated. When optimizing for temperature, a temperature gain of $1.7 - 2.0$ºC for T_{90}(tumour) could be obtained by upgrading

the applicator from one ring with four pairs of antennas to three rings with eight independent antennas each.

All applicators except the Coaxial TEM are closed water bolus systems. The space between patient and antenna(s) is filled with one or more silicone bags containing water, often of low temperature to cool the skin of the patient. The Coaxial TEM, however, is an open water bolus type system. The patient is surrounded by water from toes up to upper chest. This approach enables optimal skin cooling and relieves the patient of the pressure from the bolus weight during treatment. The large contact area between bolus and patient also allows good control of the systemic temperature (De Leeuw *et al.*, 1999). One disadvantage of the Coaxial TEM system is the confinement of the patient in the tube holding the water bolus. This limits access to the patient and inspection of thermometry probes in the patient during treatment, and some patients may experience claustrophobia.

The limited length of the water bolus of closed systems can cause local pain in the upper thighs due to fringing fields at the bolus edge (Jia *et al.*, 1994). This can be more or less prevented by elongating the bolus (Hornsleth, 1996; Wiersma *et al.*, 1998), but this solution further increases the burden of the bolus weight. The absence of cooling water between the legs and other air pockets between the skin and the bolus bags can give rise to local hot spots, especially in the perineal area (Van der Zee, 2001). The length of the water bolus affects the size of the central SAR maximum in a phantom (De Leeuw, 1993; Hornsleth, 1996). A short water bolus confines the SAR maximum to its centre, so it can be expected that a longer water bolus is needed for good longitudinal control.

An open water bolus can be considered to be extremely elongated without the disadvantage of the added weight and seems the 'natural' solution to the fringing field problem. The bolus length puts no limitations on the longitudinal SAR control and the free flowing water provides optimal skin cooling and avoids air pockets.

Considering the advantages of both multi-ring, multi-antenna applicators with phase/amplitude control and an open water bolus, we have decided to investigate the possibility of combining both principles. Placing the patient in slightly bent posture (see figure 3.1) in a bathtub makes it possible to surround the patient with an elliptically shaped, completely submerged annular array antenna. The space available for the antenna array is large enough to contain several rings of antennas. The patient will be in a comfortable posture positioned on a stretcher. No part of the patient near the antenna array is close to an air-bolus boundary, except where the anterior chest protrudes the water bolus. The patient is easily accessible for inspection during treatment. This also enables easy placement of absorbing structures (see Chapter 2) at the skin for *ad hoc* relieve of superficial pain. The total height of the patient in a horizontal position while maintaining the
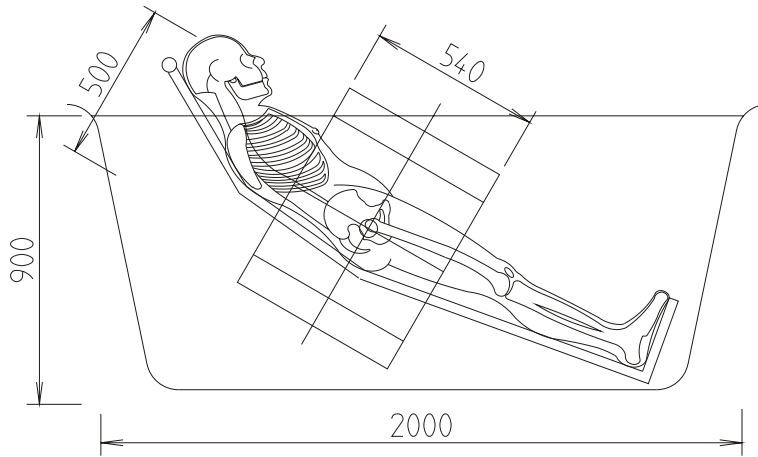
Figure 3.1: Patient in a 'bathtub type' open water bolus, surrounded by a submerged annular array of antennas. Main dimensions in millimeters.

same bent posture does not exceed 60 cm, so imaging with standard CT or MRI devices in the same bent posture is possible.

We investigated the performance of a model of an antenna array suitable for a 'bathtub type' applicator using the finite difference time domain (FDTD) SAR model of our hyperthermia treatment planning system (Van de Kamer *et al.*, 2001a) and compared it with simulations of the Coaxial TEM system. Furthermore, we numerically evaluated the SAR steering capacity in several patient models, while varying some design parameters: the number of antennas per ring, the applicator dimensions and the operating frequency. The effect of varying the operating frequency was substantiated with temperature computations. Finally the effect of the bent patient posture and possible fringing field effects at the air-patient-bolus boundaries were examined. These results are to serve as a guide for further technical development of a new applicator.

3.2   Methods

3.2.1   Applicator dimensions

The general set up in figure 3.1 shows the general dimensions of the proposed applicator. The patient bore can have a height of 50 cm with the patient bore fully submerged and the geometric centre of the antenna array central in the

pelvic region. As 50 cm is not wide enough for normal patients, an elliptic bore is made with a width of 64 cm. This bore is suitable for 95% of the Dutch population [1]. The patient depicted in figure 3.1 has a length of 180 cm, about the average length of the mentioned group. Larger and smaller patients can be placed in the applicator by varying the stretcher position, the tilt angle of the antenna array and the water level in the tub. Very small patients will fit in the applicator, but the required more upright orientation of the stretcher might be uncomfortable during a lengthy hyperthermia session. In this configuration the antenna array can have a length of 54 cm when centered on the pelvic region and with the patient bore fully submerged. This is sufficient for three rings of antennas with a length of 18 cm, about half a wavelength at 100 MHz in water.

3.2.2 Cavity slot antenna

We propose to use a slot antenna as radiating element. This type of antenna consists of a narrow slot of half a wavelength long in a conducting metal sheet and is the complement of the common half wave dipole (Collin, 1985). The slot antenna is exited by a source connected across the slot halfway its length, so the $\vec{E}$-field of the radiated wave is along the width of the slot. In RF annular array hyperthermia applicators the dominant electric field is chosen to be along the longitudinal axis of the applicator. This means that the slots are to be oriented perpendicular to the longitudinal axis of the applicator, i.e. along the elliptical circumference of the patient bore. This circumference is long enough to contain 8 half wavelength 100 MHz slot antennas with ample inter antenna spacing (see figure 3.2). The theoretical impedance of a resonant slot antenna is 487 Ω in vacuum (Collin, 1985), so it will be close to 50 Ω when submerged in water. This means that no matching network is needed when a slot antenna is connected to a standard transmission line.

Like a dipole, a slot antenna has a symmetrical radiation pattern, i.e. it radiates both in forward and backward direction in an isotropic medium. In closed water bolus systems the dipole antennas are mounted at a water-air boundary and by selecting the physical length of the dipole close to half a wavelength in water it is made a suboptimal radiator into air, i.e. most of the energy is radiated into the water bolus. In our proposed open water bolus, bath tub type applicator the antenna is completely submerged in water, so it needs other means to direct the RF energy into the patient. To improve the directivity of the slot antenna a metal box can be fitted behind the slot. This cavity can be filled with de-ionised water to reduce its dimensions. Cavity backed slot antennas mounted in an array configuration have small mutual coupling effects (Omiya *et al.*, 1998) and are thus suitable elements in a phased array antenna.

---

1. www.io.tudelft.nl/research/ergonomics/ page:DINED
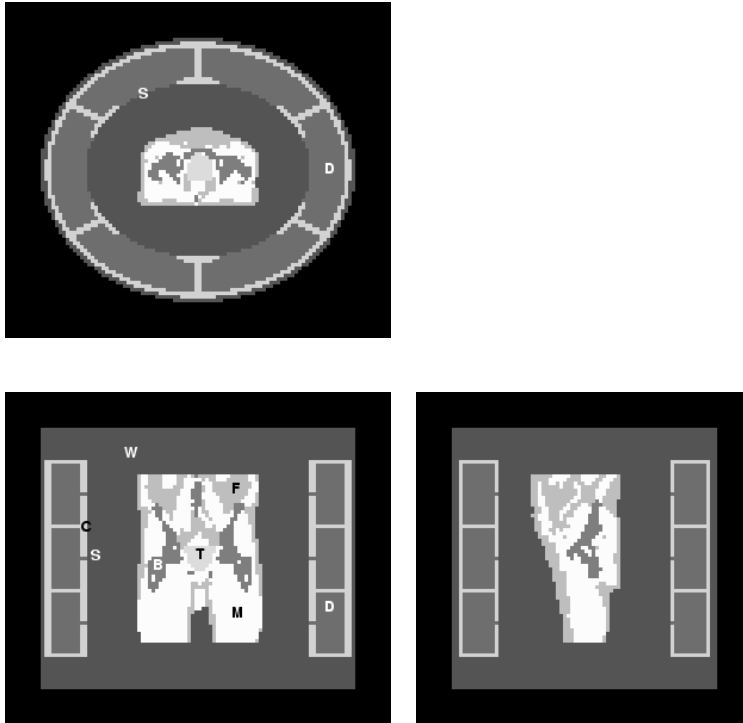
Figure 3.2: RHOCS applicator with patient A inserted. The patient is segmented in muscle (M), fat (F) and bone (B); the tumour (T) in placed in the centre of the applicator. The applicator consists of metal cavities(C), filled with Deionised water (D). The radiating slots (S) direct energy into the patient trough the water bolus (W).

A Cavity Slot applicator with three rings and six antennas per ring is shown in figure 3.2. We dubbed this system the Regional Hyperthermia Open water bolus Cavity Slot (RHOCS) applicator.

3.2.3   Parameter variation

In order to evaluate the influence of the number of antennas and their configuration, the dimensions of the antenna array and the operating frequency, SAR distributions were computed and evaluated in three different patient models. The effect of the number of rings was evaluated with one patient model for two and

three rings. All other simulations with patients were done with three ring applicators. The number of radiators was set at four, six and eight antennas per ring. More antennas per ring were not implemented, the available space would limit the size of the antennas and therefore their efficiency (Wlodarczyk *et al.*, 1997). The number of rings m and antennas per ring n of a certain array will further be referred to as $m \times n$. The dimensions of the patient bore were varied from 64×50 cm^2 to 56×44 cm^2. The operating frequencies investigated were 100 MHz, 150 MHz and 200 MHz.

3.2.4 Coaxial TEM

The Coaxial TEM system has been described extensively in De Leeuw and Lagendijk (1987). The applicator is characterised by a circumferential radiating aperture surrounding a water filled plastic tube with a diameter of 60 cm. The patient is placed in the tube laying on a stretcher and is positioned with the pelvic area in the central aperture plane using a shifting mechanism. The Coaxial TEM operates at 70 MHz and is driven by a single 2500 W generator. The simulated results with the patient models in the Coaxial TEM are used as a basis for comparison to evaluate the improvement obtained with the RHOCS applicator.

3.2.5 Patient models

The patient models A, B and C were derived from 40 cm CT data sets (slice thickness 5 mm), which are segmented by Hounsfield Unit thresholding (Hornsleth *et al.*, 1996) and down scaled to 1 cm resolution, using the 'winner take all' algorithm (James and Sullivan, 1992). This method results in a patient model with regions that are assigned constant dielectric properties, contrary to methods that average dielectric properties over a number of sub-voxels. The latter method is known to underestimate SAR peaks at tissue boundaries (Wust *et al.*, 1999; Van de Kamer *et al.*, 2001c). The material properties are listed in table 3.1, the dielectric properties (Gabriel *et al.*, 1996) were assumed to be constant in the frequency range studied in this chapter.

Patients A and C are male patients with a prostate carcinoma, patient B is a female with a cervical tumour. A physician outlined the tumours, as well as three volumina of interest in patient C, where local pain could be expected. Patients A, B and C all received 5 hyperthermia treatments in the Coaxial TEM applicator with reasonable success. The tumour temperatures (average T_{50} measured in the urethra (prostate) or the cervical canal during the steady state period) were 40.2ºC, 39.8ºC and 41.4ºC in patients A, B and C respectively. During treatment the maximum systemic temperatures, measured in the esophagus (De Leeuw *et al.*, 1999) were (averaged over 5 treatments) 38.1ºC, 38.0ºC and 39.4ºC.

Table 3.1: Dielectric and materials properties applicator materials and patient tissues

material/ tissue		rel. permittivity ε_r	conductivity $\sigma(\mathrm{S\,m^{-1}})$	density $\rho(\mathrm{kg\,m^{-3}})$
applicator	metal	1	1.0×10^5	7900
	De-ionised water	76.5	0.001	1000
	tap water	76.5	0.042	1000
patients	muscle	75	0.75	1050
	fat	10	0.06	880
	bone	10	0.05	1595
	tumour	65	0.74	1050
	lung	20	0.2	750

The patient model D is made from a much longer CT scan, including the head and the upper legs. In order to study the effect of the bent patient posture needed in the proposed 'bathtub' applicator, the segmented patient is transformed into a bent posture by shifting slices in the anterior direction. After down scaling to 1 cm resolution, a hypothetical tumour was inserted into the pelvic region. The water bolus is extended and tilted to account for the effect of the upper chest projecting out of the water bolus.

3.2.6   SAR model

The FDTD-core of our Regional Hyperthermia Treatment Planning (HTP) system (Hornsleth, 1996; Van de Kamer *et al.*, 2001a) was used to compute $\vec{E}$-field distributions in the patient models. The HTP system was validated by comparing measured and computed $|\vec{E}|^2$ in a phantom in the Coaxial TEM and found to be in good agreement (Van de Kamer *et al.*, 2001a). The definition of applicators is done using our Generic Object Format (De Bree, 1998).

The regional HTP system uses a symmetric implementation of the FDTD method (Van de Kamer *et al.*, 2001a) using Retarded Time Absorbing Boundary Conditions (RT-ABC) (Berntsen and Hornsleth, 1994). The resolution was set at 1 cm, the time step $\delta t = 1.67 \times 10^{-11}$ s follows from the resolution and the use of the RT-ABC. The number of iterations was 9000; convergence was tested by observing the time evolution of $|\vec{E}|$ at test points in the patient and found to be stable within 1% of the end value. The $\vec{E}$-field distribution is computed for each separate slot antenna. The active slot is excited with a source of unit amplitude placed in the gap in the metal sheet halfway along the length of the slot. The source has an impedance of 50 Ω, implemented as described by Piket-May *et al.* (1994). The
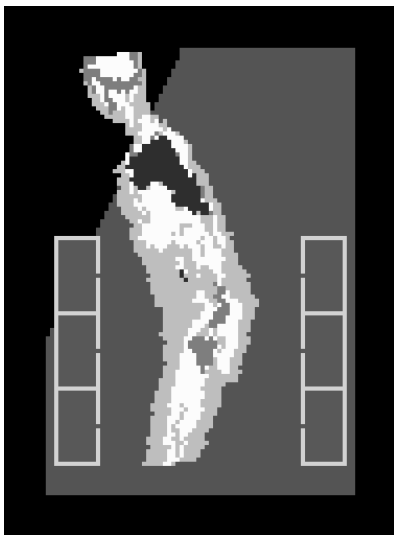
Figure 3.3: Patient D in bent posture in a 3 × 6 RHOCS applicator with tilted water bolus.

inactive slots are terminated with the same impedance in order to achieve correct simulation of coupling effects between the antennas. However, practical generator systems in general do not have an output impedance of 50 Ω, but are capable of delivering RF power into a 50 Ω load with maximum efficiency (Raskmark, 1995). Both waves reflected at the cable-antenna connection and waves coupled in from other antennas will be reflected at the generator output, resulting in a standing wave pattern on the cable connecting the generator output and the antenna. This results in unpredictable antenna gap voltages and thus deviation from the results obtained by simulation. Insertion of a circulator properly terminated with 50 Ω can solve this problem without significant loss of efficiency. The terminated circulator creates a matched load for the backwards traveling waves in the cable, and this is equal to terminating all antennas with 50 Ω. In general the antenna impedance will not be real, so the antenna gap voltage will not be in phase with the source voltage as assumed in the model. This effect can be calibrated out with a measurement of the scattering matrix of the applicator system (Raskmark *et al.*, 1994b).

A typical $\vec{E}$-field computation takes ∼ 1.7 hour and requires about 49 MB RAM on a Pentium®, 450 MHz standard personal computer, running GNU/Linux®. The SAR distribution for N $\vec{E}$-fields is computed according to equation 3.1 using

a steering vector $\mathbf{V}$, where $\mathbf{V}_i$ is the complex number representing the amplitude and phase of each antenna.

$$\text{SAR}(\vec{r}) = \frac{\sigma(\vec{r})}{2\rho(\vec{r})} \left| \sum_i^N \vec{E}(\vec{r})_i \, \mathbf{V}_i \right|^2 \tag{3.1}$$

In equation 3.1 $\text{SAR}(\vec{r})$ is the SAR, $\vec{E}(\vec{r})_i$ is the $\vec{E}$-field for antenna i, $\sigma(\vec{r})$ and $\rho(\vec{r})$ are respectively the conductivity and density of the voxel at $\vec{r}$.

3.2.7   Optimization objective function

A number of optimization objective functions were defined for power deposition (Fenn and King, 1996; Clegg *et al.*, 1996; Wust *et al.*, 1996; Das *et al.*, 1999b; Paulsen *et al.*, 1999) and temperature distribution (Wust *et al.*, 1996; Das *et al.*, 1999a). Most power deposition optimization objective functions maximise the ratio of SAR in tumour with respect to normal tissue, or with respect to a set of SAR maxima in normal tissue. Optimization of temperature distribution is not considered in this study.

In this study we used an optimizer that maximizes an objective function of $\mathbf{V}$, defined as the ratio of SAR in two volumina (3.2), for example the total SAR in tumour versus the total SAR in the remaining muscle tissue.

$$\text{Obj}(\mathbf{V}) = \frac{\sum \text{SAR}(\text{numerator volume}, \mathbf{V})}{\sum \text{SAR}(\text{denominator volume}, \mathbf{V})} \times 100\% \tag{3.2}$$

This optimization objective function is effectively equal to the one Paulsen *et al.* (1999) selected for use with a highly heterogeneous patient model after testing objective functions that minimise SAR maxima in normal tissue.

The optimizer modifies the steering vector $\mathbf{V}$ in small steps from a start vector in the direction of maximal improvement of the objective function (Steepest decent method (Press *et al.*, 1988)). This involves repeated computation of the total SAR in a fixed volume. This computation can be done efficiently using the following method.

Equation 3.1 can be rewritten in matrix form as

$$\text{SAR}(\vec{r}, \mathbf{V}) = \frac{\sigma(\vec{r})}{2\rho(\vec{r})} \, \mathbf{V}^{\text{H}} \, \mathbf{E}^{\text{H}} \, \mathbf{E} \, \mathbf{V} \tag{3.3}$$

where $\mathbf{E}$ is a complex $3 \times N$ matrix with the x, y, z components of the E-fields at $\vec{r}$ and $\mathbf{V}^{\text{H}}$ is the complex conjugate transpose of $\mathbf{V}$. For a volume Q the $\sum \text{SAR}(Q, \mathbf{V})$ is

$$
\begin{aligned}
\sum \mathrm{SAR}(Q, \mathbf{V}) \ &= \ \sum_{\vec{r}}^{Q} \frac{\sigma(\vec{r})}{2\rho(\vec{r})} \, \mathbf{V}^{\mathrm{H}} \, \mathbf{E}^{\mathrm{H}} \, \mathbf{E} \, \mathbf{V} \\
&= \ \mathbf{V}^{\mathrm{H}} \Big[\sum_{\vec{r}}^{Q} \frac{\sigma(\vec{r})}{2\rho(\vec{r})} \, \mathbf{E}^{\mathrm{H}} \, \mathbf{E} \Big] \, \mathbf{V} \\
&= \ \mathbf{V}^{\mathrm{H}} \, \mathbf{I}_Q \, \mathbf{V}
\end{aligned}
\tag{3.4}
$$

The matrix $\mathbf{I}_Q$ is called the influence matrix (Bardati *et al.*, 1995) and is complex, Hermitian and positive. The influence matrix can be computed from the set of E-fields once and then SAR_Q can be evaluated for various steering vectors $\mathbf{V}$. This requires only $N^2 + N$ calculations, irrespective of the number of voxels in Q. In order to be able to enhance or suppress the SAR in certain subvolumina an optional weight $w(\vec{r})$ can be given to voxels belonging to these subvolumina in the computation of the influence matrix.

$$
\mathbf{I}_Q = \sum_{\vec{r}}^{Q} \frac{\sigma(\vec{r}) w(\vec{r})}{2\rho(\vec{r})} \, \mathbf{E}^{\mathrm{H}} \, \mathbf{E}
\tag{3.5}
$$

After computation of the numerator and denominator influence matrices the optimization process is completed within 15 s. In order to test whether the optimizer has reached the absolute maximum of its objective function, it is restarted repeatedly with random start vectors (Das *et al.*, 1999a).

The optimizer can be set to constrain the power per antenna to a predefined maximum percentage of the total power. This avoids unrealistic steering vectors that no practical generator set could produce due to power limitations per channel.

3.2.8 Performance indices

To evaluate the performance of applicator systems Hornsleth (1996) introduced the indices

$$
API1 = \frac{\sum_{muscle} \mathrm{SAR}}{\sum_{fat} \mathrm{SAR}}
\tag{3.6}
$$

$$
API2 = \frac{\mathrm{SAR \ in \ centre \ of \ phantom}}{\mathrm{Maximum \ of \ SAR \ in \ phantom}}
\tag{3.7}
$$

The API1 index quantifies the ability to heat at depth without excessive superficial heating and the API2 index expresses the systems ability to focus energy at the centre of a phantom. However, these indices are only applicable to a particular phantom, because the indices are calculated for a specific volume or a specific location in the phantom. The obtained maximum of the objective function can also serve as a performance indicator, but its value also depends on target and non-target volume. This limits performance comparison between different patient models. Furthermore the use of performance indices that are independent of the objective function makes it possible to identify the specific effect of design parameter changes on the SAR distribution in target and non-target tissue. In all comparisons in this study the result of the optimizer, i.e. the maximum of the objective function is presented. Furthermore, three indices are computed from each SAR distribution:

$$\text{Ti} \quad = \quad \frac{\text{SAR}_{50}(\text{tumour})}{\text{SAR}_{50}(\text{totalpatient})} \tag{3.8}$$

$$\text{MMi} \quad = \quad \frac{\text{SAR}_{1}(\text{muscle})}{\text{SAR}_{50}(\text{tumour})} \tag{3.9}$$

$$\text{FMi} \quad = \quad \frac{\text{SAR}_{1}(\text{fat})}{\text{SAR}_{50}(\text{tumour})} \tag{3.10}$$

where $\text{SAR}_{50}(Q)$ is the median SAR in the subvolume Q and $\text{SAR}_{1}(Q)$ is the value indicating the highest percentile of the SAR distribution in the indicated subvolume. The Tumour index Ti indicates the ability of the applicator to selectively direct energy into the tumour. The Muscle Maximum index MMi gives the level of the highest percentile of the SAR distribution in muscle with respect to the median value in tumour, i.e. it indicates the level of the maxima in muscle. The Fat Maximum index FMi is an identical ratio for fat. The indices are, contrary to the objective function, not dependent on the number of voxels in the subvolumina. This enables direct inter patient comparison of the indices.

In the patient models A, B and C the tumour volume is respectively 323, 93 and 111 cm^3, average tumour volume is 176 cm^3. The average number of muscle and fat voxels is around 12500. The highest percentile of both muscle and fat is a volume of comparable size to the tumour, although this volume can be divided in several, unconnected subvolumina.

The indices were selected to enable evaluation of two major aspects of applicator performance:
- selective heating of the tumour
- ability to avoid hot spots

The importance of preventing hot spots, possibly related to SAR maxima, is indicated by the observation (Wust *et al.*, 1999) that in more than 80% of all regional hyperthermia patients treatment limiting hot spots occur. This aspect of applicator performance was not assessed by Paulsen *et al.* (1999). A good applicator should have a high Ti and low MMi and FMi.

3.2.9 Thermal model

Temperature distributions have been computed from the SAR distributions using our DIVA thermal model (Kotte, 1998), without accounting for the effect of the discrete vasculature. The tissue blood perfusion was modelled by means of a heatsink (see table 3.2). The tumour perfusion was taken half the value of the surrounding muscle tissue (Wust *et al.*, 1996).

Table 3.2: Thermal properties of patient tissues

Tissue	Capacity C_p $J\,kg^{-1}\,K^{-1}$	Conductivity κ $W\,m^{-1}\,K^{-1}$	Perfusion w_b $kg\,m^{-3}\,s^{-1}$
fat	2387	0.22	1.1
muscle	3639	0.56	3.6
tumour	3639	0.56	1.8
bone	1420	0.65	0.12

3.3 Results

3.3.1 Comparison of Coaxial TEM and RHOCS applicator

Patients A, B and C were all treated in the Coaxial TEM applicator. From the treatment planning results for this applicator the performance indices were calculated. The same patient set was simulated in a 3×6 RHOCS applicator and optimized for SAR(tumour) vs. SAR(muscle+fat) without power constraints. The results are listed in table 3.3 In all three cases an improvement of the objective function and the tumour index can be seen, accompanied by almost equal or slightly decreased muscle and fat maximum indices. This indicates the improvement that can be obtained with respect to the Coaxial TEM. However, it was observed that the optimizer designates rather high power levels to a few antennas, in one case (C) 16.5% of total power to one antenna. These are unrealistic power distributions, that can not readily be produced with available generator systems (Wust *et al.*, 1998a). The optimizations were repeated, but with an constraint imposed on the power distribution: all antennas were restricted to 10% of total available power. The results listed in table 3.3 show that optimization with this power constraint is

(a)   (b)   (c)

(d)   (e)   (f)
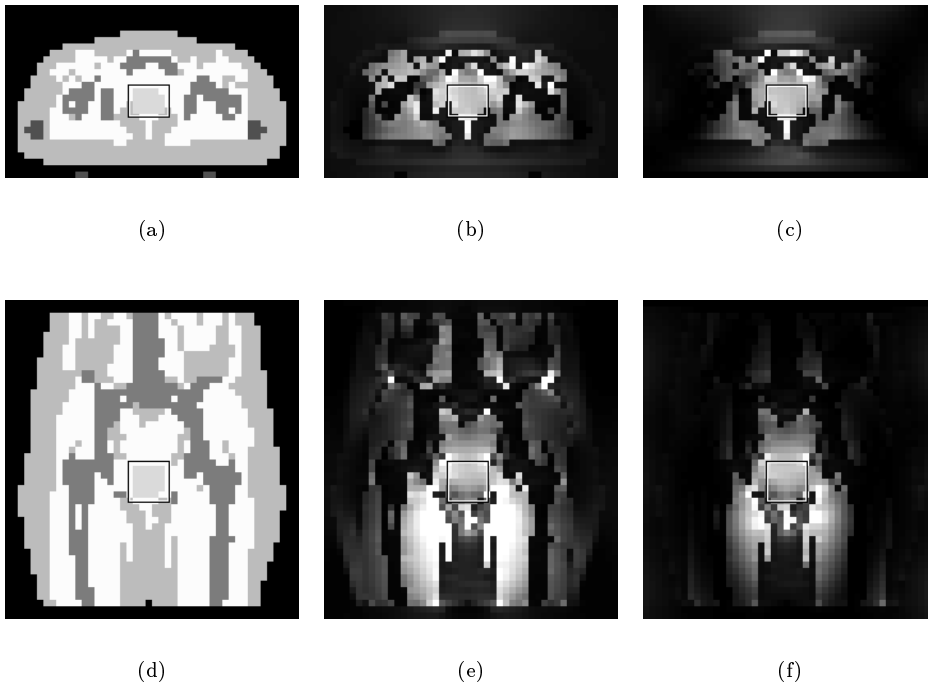
Figure 3.4: patient B in (a) transversal and (d) coronal slices, the
tumour region is marked with a ractangle. (b) and (e) SAR
distribution in the Coaxial TEM, (c) and (f) SAR distri-
bution in 3×6 RHOCS applicator operating at 100 MHz
and optimized for SAR(tumour) vs. SAR(muscle+fat) with
power constraints

not substantially limited and the improvement with respect to the Coaxial TEM
is maintained.

The Coaxial TEM was also simulated at 100 MHz with one patient model (C).
The performance indices show a slight improvement for this frequency, but the
improvement in the RHOCS is far better. This indicates that the general improve-
ment obtained with the RHOCS applicator is not caused by the higher operating
frequency, but is mostly an effect of its SAR steering ability.

Figure 3.4 shows the SAR distributions in patient B in the Coaxial TEM and the
RHOCS applicator. It can be seen that the maximum in the thighs, produced by
the Coaxial TEM (figure 3.4(e)) is significantly reduced in the RHOCS.

Table 3.3: Performance indices in three patient models. Comparison of Coaxial TEM vs. 3×6 RHOCS applicator operating at 100 MHz, optimized for SAR(tumour) vs. SAR(muscle+fat) with and without power constraint ($P_{ant} \leq 10\% \, P_{total}$)

patient	applicator	f(MHz)	constraint	Obj	Ti	MMi	FMi
A	Coaxial TEM	70	-	2.30	2.09	2.37	1.10
	RHOCS	100	no	3.74	5.82	2.40	0.89
	RHOCS	100	yes	3.69	5.53	2.24	0.79
B	Coaxial TEM	70	-	0.79	4.61	1.92	0.56
	RHOCS	100	no	1.57	9.77	1.45	0.50
	RHOCS	100	yes	1.56	9.90	1.46	0.50
C	Coaxial TEM	70	-	0.85	1.88	3.15	1.12
	Coaxial TEM	100	-	0.88	2.04	3.08	0.94
	RHOCS	100	no	1.24	4.65	3.04	0.95
	RHOCS	100	yes	1.23	4.57	3.01	0.90

3.3.2 Effect of variation of applicator parameters

The influence of variation in the design parameters of the antenna array was investigated using the patient A model and an operating frequency of 100 MHz. The numerical results are presented in table 3.4. An increase of Ti is observed when increasing the number of rings from two to three with the same total number of antennas. However, MMi en FMi also increase. Increasing the number of antennas per ring to six improves Ti, MMi and FMi. A further increase to eight antennas per ring improves Ti but deteriorates MMi and FMi. Reduction of the patient bore from 64×50 cm^2 to 56×44 cm^2 with six antennas per ring also improves Ti but deteriorates MMi and FMi.

Table 3.4: Performance indices in patient A. Parameter variation of RHOCS applicator, operating at 100 MHz, for SAR(tumour) vs. SAR(muscle+fat)

no. rings	no. antennas	total no. antennas	dimension (cm^2)	objective (%)	Ti	MMi	FMi
2	6	12	64×50	3.42	4.90	2.44	0.92
3	4	12	64×50	3.63	5.47	2.53	1.04
3	6	18	64×50	3.74	5.82	2.40	0.89
3	6	18	56×44	4.01	6.95	2.85	1.47
3	8	24	64×50	4.17	7.42	2.77	1.34

The effect of varying the operating frequency was tested in patients A, B and C, at 100, 150 and 200 MHz, using a six antennas per ring applicator. Table 3.5 lists the results. In all patients the improvement at 150 MHz is evident, and the results at 200 MHz are in all cases worse than those obtained at 100 MHz

Table 3.5: Performance indices in three patient models. Comparison of 3×6 RHOCS applicator operating at 100,150 and 200 MHz, optimized for SAR(target) vs. SAR(muscle+fat) with power constraints ($P_{ant} \leq 10\%$ P_{total})

patient	frequency (MHz)	Obj	Ti	MMi	FMi
A	100	3.69	5.53	2.24	0.79
	150	3.33	7.32	1.88	0.77
	200	2.28	3.80	4.82	1.68
B	100	1.56	9.90	1.46	0.50
	150	1.97	12.01	1.23	0.50
	200	1.42	7.23	1.44	0.97
C	100	1.23	4.57	3.01	0.90
	150	1.65	6.71	2.37	0.78
	200	1.20	4.66	3.68	1.32

3.3.3 SAR reduction in selected regions

In order to assess the ability of the RHOCS applicator to minimize the SAR pattern in certain regions, three regions were selected in the model of patient C. The lumbosacral region, the region in front of the symphysis os pubica and part of the scrotum, indicated in figure 3.5(a) are known as locations of treatment limiting pain in this patient. SAR distributions were computed at 100 MHz (figure 3.5(b)) and 150 MHz (figure 3.5(c)) in a 3×6 RHOCS applicator, optimized for SAR(tumour) versus SAR(muscle+fat), and in the Coaxial TEM at 70 MHz (not shown). In order to obtain Local SAR Reduction (LSR) in the selected regions, the weight of the regions in the denominator of the optimizer objective function was set at 50, where the remaining muscle and fat tissue had a weight of 1. Figures 3.5(d) and 3.5(e) show the SAR distribution with this SAR reduction attempt at 100 MHz and 150 MHz respectively. At both frequencies the reduction in the lumbo sacral region is impressive. To evaluate the effect of the SAR reduction technique the average SAR is computed in the selected regions, separately for muscle and fat tissue. The results are shown in table 3.6 together with the performance indices. The averaged SAR in the selected regions is reduced at both frequencies, except

the scrotum region at 100 MHz. The SAR reduction is more effective at 150 MHz; when compared to the Coaxial TEM a reduction to at least 50% is observed. The performance indices deteriorate to some extend by the optimization with SAR reduction. However, the indices at both frequencies are better then those obtained in the Coaxial TEM, particularly at 150 MHz.

Table 3.6: SAR in selected regions relative to SAR in tumour at 100 MHz and 150 MHz, effect of Local SAR Reduction (LSR) on performance indices.

SAR averaged	Coaxial TEM 70 MHz	RHOCS 100 MHz no LSR	LSR	RHOCS 150 MHz no LSR	LSR
pre symphysis					
fat	0.68	0.72	0.43	0.53	0.34
muscle	2.88	3.05	2.08	2.11	1.42
lumbo sacral					
fat	0.57	0.45	0.13	0.34	0.08
muscle	1.78	1.61	0.17	1.02	0.09
scrotum					
muscle	1.35	0.57	0.75	1.04	0.63
performance index					
obj(%)	0.85	1.23	0.88	1.65	1.26
Ti	1.88	4.57	3.03	6.71	4.92
MMi	3.15	3.01	3.10	2.37	2.17
FMi	1.12	0.90	0.98	0.78	0.70

3.3.4   Resulting temperature distributions

Figure 3.6 shows the calculated temperature elevation in a sagittal slice in patient B in a 3×6 RHOCS applicator, after optimization for SAR(tumour) vs. SAR(muscle+fat) with power constraints at 150 MHz. The total power absorbed in the patient volume was normalised at 250 W. A maximum temperature elevation of 7 K centrally in the tumour can be observed.

Temperature rise computations were done for patients A, B and C in the Coaxial TEM and a 3×6 RHOCS applicator at 100 MHz, 150 MHz and 200 MHz. The resulting temperature indices are shown in figure 3.7. The median tumour temperature is compared to T_{10} and T_1 in muscle. In the Coaxial TEM computations the total absorbed power is set at 400 W, and in the RHOCS at 250 W. This

(a)   (b)   (c)

(d)   (e)
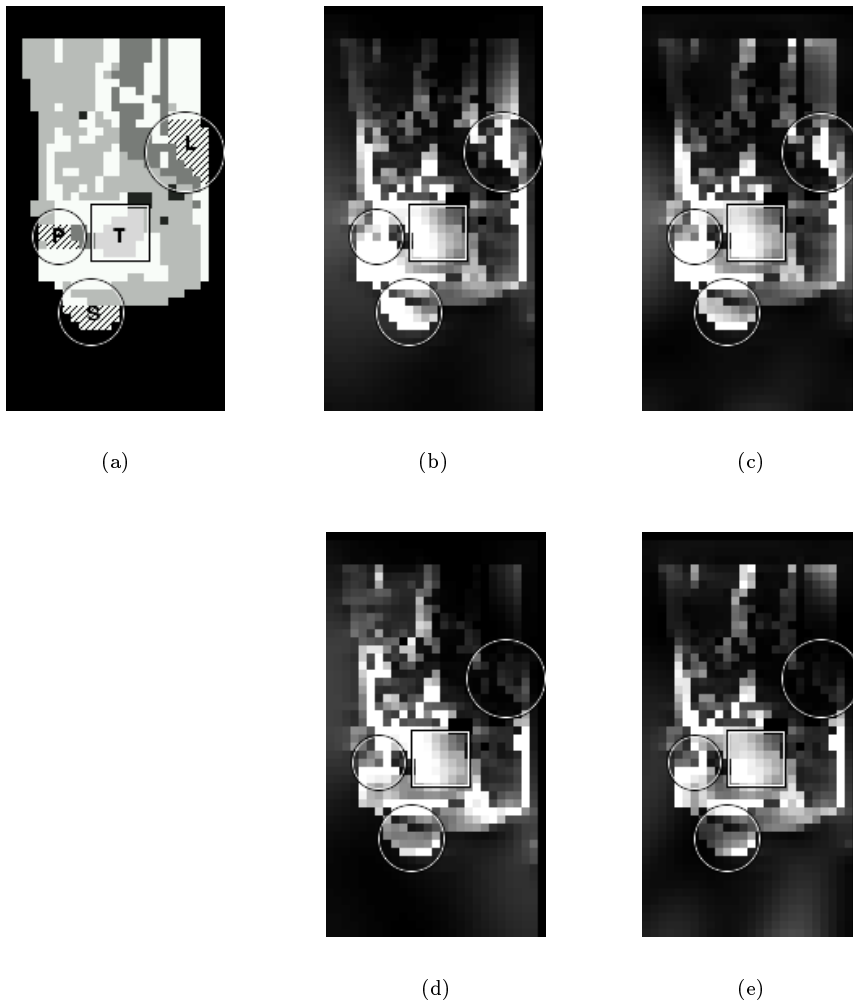
Figure 3.5: Local SAR reduction in patient C. (a) regions
(dashed) where local pain is expected are outlined by a
physician: the lumbo sacral (L) region, the pre symphysis
(P) region and the scrotum (S); for clarity the tumour (T)
is marked with a rectangle. (b) shows SAR at 100 MHz and
(c) at 150 MHz, without attempts to reduce SAR in these
regions. (d) is SAR at 100 MHz and (e) at 150 MHz using
optimization to reduce SAR in the regions

(a)   (b)
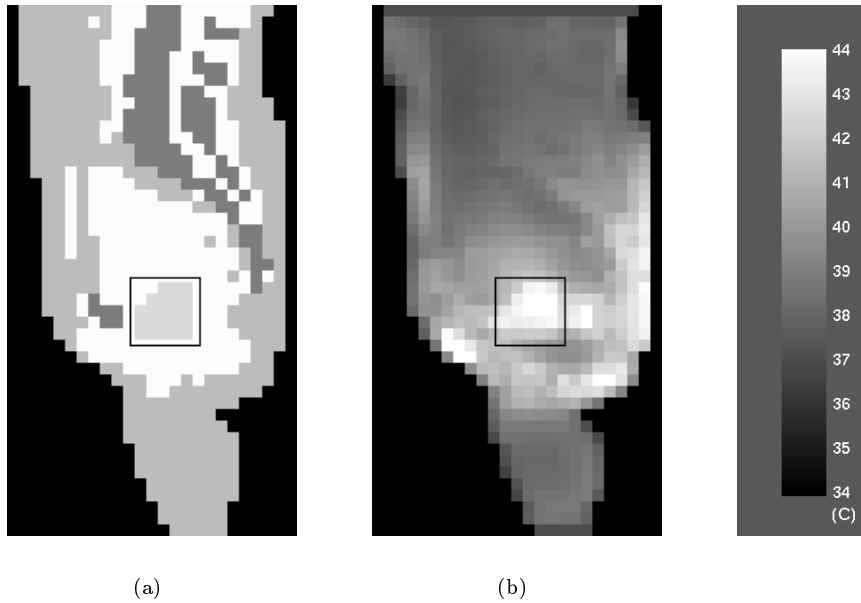
Figure 3.6: (a) Sagittal slice in tomogram and (b) temperature
distribution in patient B in a 3×6 RHOCS applicator at
150 MHz, optimized for SAR(tumour) vs. SAR(muscle+fat)
with power constraints

resulted in a more or less constant T_1 in muscle in all patients, not exceeding 5 K.
Despite the reduced absorbed power in the RHOCS applicator, the median tumour
temperature at 100 MHz and 150 MHz is higher in all patients, when compared
to the Coaxial TEM. However, at 200 MHz the tumour temperature rise is lower
than that obtained in the Coaxial TEM.

A moderate reduction of T_{10} in muscle can be observed in the RHOCS applicator
with increasing frequency. In all patients the best result is obtained at 150 MHz,
however the elevated level of T_1 in muscle is a matter of concern. Note that in
patient C T_1 in muscle is higher then T_{50} in tumour.

To evaluate the effect of the local SAR reduction described earlier (see 3.3.3)
the average and maximum temperatures in the selected regions in patient C are
tabulated in table 3.7. The total absorbed power level in the computations with
SAR reduction was increased to 325 W, in order to obtain comparable median
tumour temperature. This results in an increase of T_{10} in muscle. Although the
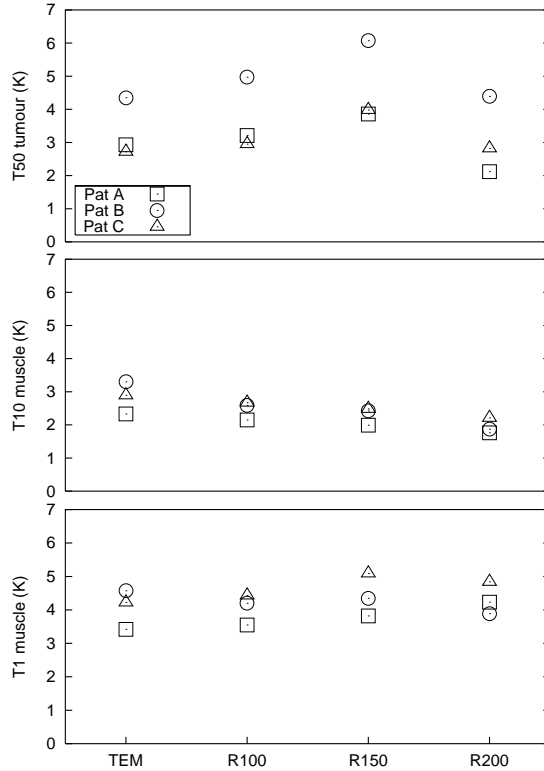
Figure 3.7: Temperature indices in patients A, B and C in the
Coaxial TEM and the RHOCS applicator at 100 MHz
(R100), 150 MHz (R150) and 200 MHz (R200), optimized for
SAR(tumour) vs. SAR(muscle+fat) with power constraints

average SAR in fat and muscle in all selected regions in the RHOCS applicator at
150 MHz, optimized without SAR reduction, is lower then the average SAR in the
same regions in the Coaxial TEM (see table 3.6), the average temperatures can
actually be higher. Both at 100 MHz and 150 MHz the average temperatures in the
pre symphysis and scrotum region are higher than those obtained in the Coaxial
TEM. When reducing high SAR in the selected regions, the average and maximum
temperature also appear to drop. Again the reduction in the lumbo sacral region
is most impressive, and both other average values are below the corresponding
values in the Coaxial TEM.

The temperature simulations also allow a validation of the clinical significance

Table 3.7: Effect of Local SAR Reduction (LSR) at 100 MHz and 150 MHz in patient C on temperatures (average and maximum)

	Coaxial TEM 70 MHz	RHOCS 100 MHz no LSR	LSR	RHOCS 150 MHz no LSR	LSR
T50 tumour	2.72	2.96	2.89	3.98	4.09
T50 muscle	1.82	0.75	1.28	0.68	1.15
pre symphysis					
T average	3.27	4.03	2.36	3.86	2.48
T max	11.1	11.2	7.70	10.3	7.14
lumbo sacral					
T average	2.97	2.82	0.49	2.59	0.40
T max	6.12	4.74	2.02	6.09	2.17
scrotum					
T average	1.23	1.76	0.44	1.48	0.69
T max	2.21	2.78	1.56	2.63	2.08

of the SAR based indices. Figure 3.8(a) shows the relation between the Tumour index (Ti) and the T_{50} obtained in tumour for the patients A, B and C in the Coaxial TEM and the 3×6 RHOCS applicator at 100, 150 and 200 MHz. In figure 3.8(b) the difference between T_1(muscle) and T_{50}(tumour) is plotted against the Muscle Maximum index (MMi). Both plots show a fair correlation, indicating that improvement of the Tumour index leads to higher tumour temperatures and reduction of the Muscle Maximum index results in lower maximum temperatures in muscle with respect to the median tumour temperature.

3.3.5   Effect of patient posture

In figure 3.9(a) a sagittal slice is shown of patient D in a bent posture in the RHOCS applicator. The slice was taken 10 cm to the right of the mid plane in order to show the position of the legs. Figure 3.9(b) shows the SAR distribution optimized for SAR(tumour) vs. SAR(muscle+fat) with power constraints in the same sagittal slice. The white circle in figures 3.9(a) and 3.9(b) indicates the critical region where the chest penetrates the water bolus near the anterior part of the antenna array. The SAR in this region is very low compared to the pelvic area. The transversal slice in the SAR distribution taken at the level of the upper ring of slots (upper black line in 3.9(a)) does not indicate maxima either. At the level of the
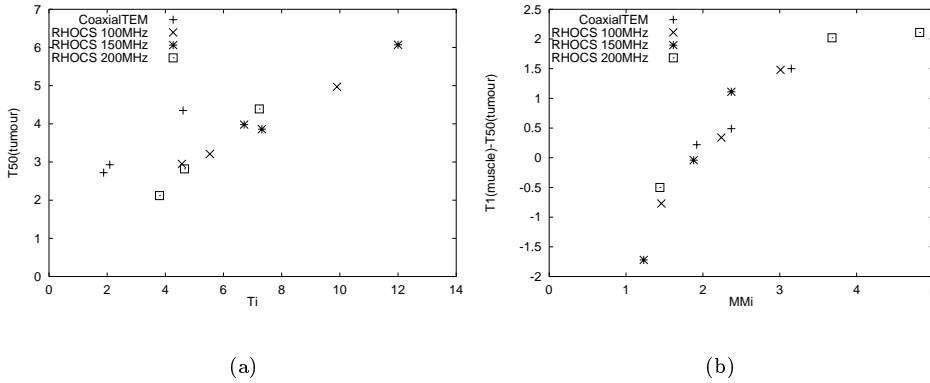
(a)   (b)

Figure 3.8: Relation between (a) Tumour index (Ti) and
T_{50}(tumour) and (b) Muscle maximum index (MMi) and
T_1(muscle) $- T_{50}$(tumour) in patients A, B and C in the
Coaxial TEM and the 3×6 RHOCS applicator at 100, 150
and 200 MHz

lower ring of slots (lower black line in 3.9(a)) however, some SAR elevation in the anterior part of the legs (figure 3.9(d)) can be observed. To further investigate this effect a worse case situation was created. The patient was shifted 5 cm forward, so that the upper chest and the legs were almost touching the antenna array. Furthermore the optimizer was set to optimize phase only and leave the power of all antennas at the same level. Even in this worst case situation no SAR extrema are evident at the water-air boundary (white circle in figure 3.9(f)). However, there are SAR maxima in the anterior chest wall and the upper legs (figures 3.9(g) and 3.9(h)). These maxima are not associated with a bolus effect but with the close proximity of an antenna radiating at high power.

3.3.6   Effect of patient positioning

In a typical patient treatment the accuracy of patient positioning and the limited similarity of the patient model acquired by imaging and the actual patient in the required bent posture will probably cause differences between the optimized simulation results and the obtained SAR distribution. To study the effect of the patient model on the SAR distribution the model of patient A was shifted 2 cm in x, y and z-direction. In all positions the $\vec{E}$-field distributions were recalculated and the SAR distributions were computed using the steering vector $\mathbf{V}$ obtained by optimization in the unshifted position. Table 3.8 gives the performance indices in

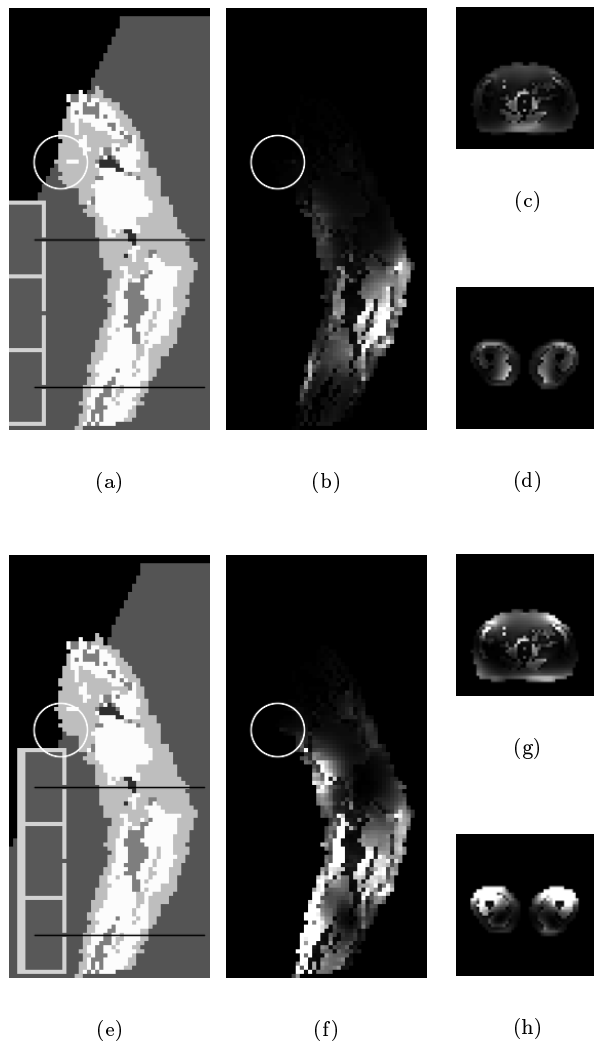**Figure 3.9:** Effect of a bent patient posture. (a) sagittal slice 10 cm right of mid plane, (b) SAR in the same sagittal slice. Transversal slices at the level of (c) the upper and (d) lower slot antenna (black lines in (a)). (e) sagittal slice with patient shifted 5 cm forward. (f) SAR with all antennas at the same power level, generating hot spots in (g) the anterior chest wall and (h) upper legs.

the shifted positions in comparison with the unshifted position. In all cases there is some degradation of one or more of the indices, especially in the y-2 case.

Table 3.8: Effect of patient shift on the performance indices in patient A, optimized for SAR(tumour) vs. SAR(muscle). Patient shifted 2 cm in x, y and z-direction. Note the adverse effects of a posterior shift (y-2).

index	Δxyz = 0	z+2	z-2	y+2	y-2	x+2	x-2
Ti	5.78	5.97	5.53	5.64	**4.54**	5.63	5.58
MMi	2.59	2.72	2.64	2.30	**3.72**	2.62	2.86
FMi	1.14	1.20	1.13	0.93	**1.62**	1.11	1.19

3.4   Discussion

This study evaluates the performance of a new applicator for Regional Hyperthermia, called the Regional Hyperthermia Open water bolus Cavity Slot (RHOCS) applicator. The applicator design retains the advantages of an open water bolus, like the Coaxial TEM.

3.4.1   Applicator dimensions

The proposed applicator is suitable for 95 % of the Dutch population, with ample space between the patient and the antennas. The applicator dimensions allow eight antennas per ring and a total of three rings. Very small patients will fit in the applicator, although the more upright orientation of the patient required might be uncomfortable. This group, possibly including a part of the Asian population can be treated in a more comfortable posture in a version with a smaller patient bore. Experiments with volunteers and an experimental submerged stretcher showed that the bended patient position is sufficiently comfortable.

3.4.2   Applicator performance

Using one of the patient models the effect of variation of the number of antenna rings and the number of antennas per ring has been evaluated. It was shown that an applicator with three rings outperforms an applicator with two rings and the same total number of antennas. Further evaluation was done with three ring applicators only. The use of eight antennas per ring results in slightly higher performance indices in patient A when compared with six antennas per ring. However, it also results in an unwanted rise of the muscle and fat maximum indices. Increasing the operating frequency from 100 MHz to 150 MHz has more positive effect than

increasing the number of antennas from six to eight per ring. The modest improvement of the performance with the increase of the number of antennas from six to eight per ring agrees with the results of Paulsen *et al.* (1999) in a four ring applicator. Wust *et al.* (1996) found a SAR improvement in tumour ranging from 1.3 to 1.6 when upgrading from 1 ring with four pairs of dipoles to three rings with eight independent dipoles. This study finds a similar increase of 1.7 averaged over three patients when substituting the Coaxial TEM with a 3×6 RHOCS applicator at 150 MHz. With the same system upgrade a temperature rise of 1.8K for T_{90} in tumour was realised by Wust *et al.* (1996) after temperature optimization. This study found a temperature rise varying from 1.0K to 1.8K for T_{50} in tumour after SAR optimisation. Wust *et al.* (1996) found a volume of 350 ml outside the tumour volume with a temperature rise exceeding 5K. Assuming a weight of 35 kg for the patient model, this volume is about 1% of the total volume. This study found a T_1 ranging from 4K to 5K at 150 MHz. The translation from SAR to temperature must be considered with great care. The present thermal models used for temperature calculation in regional hyperthermia neglect vasculature, systemic temperature response and effects of redistribution of perfusion (Lagendijk, 2000).

Evaluation of the performance indices in the patient models at 100 MHz, 150 MHz and 200 MHz indicate an optimal frequency of 150 MHz for the treatment of central pelvic tumours. Reduction of SAR in specific regions is also better achieved at 150 MHz. Additional evaluation of the temperatures obtained in the patient models confirmed this conclusion. However, the temperature simulations assumed rather favourable perfusion properties of the tumour tissue. Paulsen *et al.* (1999) also selects 150 MHz as optimal frequency in all target zones, but not for the central target volume, where almost equal results at 100 MHz and 150 MHz are found with six or eight antennas per ring. With 24 antennas per ring 150 MHz is optimal for all target zones. The discrepancy is possibly explained by the difference in definition and size of the target volume in both studies.

Three performance indices have been defined to evaluate and compare applicators: the Tumour index, the Muscle Maximum index and the Fat Maximum index. The definition of the indices is independent of the size of the related subvolumina, allowing inter patient comparison. The temperature optimization functions used by Wust *et al.* (1996) are obviously the most straightforward method to produce the desired temperature distribution. However, the method used in this study, i.e. optimize SAR and calculate temperature, produces surprisingly good temperature distributions in comparison. The observed correlation between the performance indices and temperature indices as well as the obtained temperature distributions justify the use of SAR based indices to evaluate applicator designs.

3.4.3   SAR model

$\vec{E}$-field distributions were computed using our Regional Hyperthermia Planning system, using a voxel size of 1 cm. Van de Kamer *et al.* (2001b) showed that large deviations are found between low resolution (1 cm^3) and high resolution (2 mm) FDTD computations. An averaged difference of 43% and maximum differences up to a factor seven were observed. In particular it was noted that low resolution FDTD computations tend to underestimate SAR peaks located at narrow tissue boundaries. The SAR distribution is highly dependent on the description of the anatomy. This study compared the effect of different applicators on identical patient models, so a significant part of the systematic error is not an issue in this comparison. However, the possible underestimation of SAR peaks emphasises the importance of the ability of applicator types and optimisation strategies to suppress local SAR maxima.

The increasing capacity of computational resources will allow future simulation of regional hyperthermia applicators at 5 mm resolution, reducing the systematic error with a factor four. Quasistatic zooming (Van de Kamer *et al.*, 2001b) of the optimised $\vec{E}$-field is possible down to the available CT-resolution, revealing and quantifying possible hot spots. Repeating the optimisation process will enable reduction of these SAR maxima. Direct optimisation of zoomed $\vec{E}$-field distributions is not possible, as the zooming process discards phase information.

3.4.4   Influence of dielectric properties

The indication of 150 MHz as optimal operating frequency may be affected by the assumption of constant dielectric properties over the frequency range. However, published values of dielectric properties show only a very slight slope ($< 10\%$) over the observed frequency range (Gabriel *et al.*, 1996) and a much larger variation, up to a factor two in conductivity for various sources. Van de Kamer *et al.* (2001e) showed that errors up to 50% in the dielectric properties induce errors smaller than 20% in both power density and temperature distributions, indicating a low sensitivity to the values of the dielectric properties. The contrast between the dielectric properties of muscle, fat and bone is more important than their absolute values.

To exclude possible over or under estimation of SAR distributions, one patient (C) was recalculated with variable dielectric properties. Table 3.9 shows the influence of variation of the dielectric properties with frequency on the performance indices in patient C. The dielectric properties of muscle and fat were calculated for each frequency according Gabriel (1996) [2]. These values are close to those used by Paulsen *et al.* (1999). Comparison with the results in table 3.5 shows only a minor

---

2.   http://www.fcc.gov/fcc-bin/dielec.sh

change of the performance indices and the optimal performance at 150 MHz is retained.

Table 3.9: Influence of variation of the dielectric properties with frequency on the performance indices in patient C in 3×6 RHOCS applicator operating at 100,150 and 200 MHz, optimized for SAR(target) vs. SAR(muscle+fat) with power constraints.

frequency	muscle		fat					
(MHz)	ε_r	$\sigma(\mathrm{S\,m^{-1}})$	ε_r	$\sigma(\mathrm{S\,m^{-1}})$	Obj	Ti	MMi	FMi
100	66.4	0.75	12.7	0.068	1.24	4.49	2.89	0.89
150	63.2	0.77	12.2	0.070	1.49	5.97	2.60	0.88
200	61.5	0.79	12.0	0.073	0.99	3.76	4.48	1.63

3.4.5 Patient positioning

The effect of longitudinal and lateral patient shifts has been investigated. The results show that uncertainty in the patient position can nullify the laboriously obtained advantages of applicator improvements and treatment optimization. Rietveld *et al.* (2000) recorded patient shift and stretcher sagging during treatment in a BSD-2000 Sigma-60 applicator. He showed that both a longitudinal patient shift of 2 cm and a patient posture change due to sagging of the stretcher significantly deteriorates the SAR distribution in a phantom.

Both open and closed water bolus systems will induce a change of the patient shape. In a closed system the pressure of the water bags will compress and deform the outer fat layers, in an open water bolus system the body will deform upwards. In both cases the patient model used for treatment planning will vary from the actual patient posture during treatment, probably causing deviations in the planning result.

The sagging of the stretcher is a minor problem in an open water bolus because of the reduced body weight under water. However, the patient will shift during the treatment session. Tight constraining of the patient by belts during the lengthy and burdensome treatment is less acceptable. Part of the solution of the positioning problem might be the construction of a patient specific, body conformal shell of the posterior side of the patient, using a perforated thermoplastic sheet (Posicast, SINMED BV.). Combined with a fixed stretcher for mechanical rigidity, the patient can be placed in this body conformal positioning tool in a suitable imaging device and in the hyperthermia applicator. A better similarity of the actual patient and the model can be expected.

Simultaneous Magnetic Resonace Imaging and regional hyperthermia treatment

has been performed with a multi-ring, closed waterbolus dipole system (Peller *et al.*, 2000). By measuring a temperature dependent property of the tissue molecules, non invasive thermograpy is possible during the treatment (Carter *et al.*, 1998). MR imaging and thermography is considered to be a precondition for succesfull hyperthermia treatment (Wust *et al.*, 2000). However, the dimensions and the bulk of metal forming the cavity slot antenna array practically exclude the possibility of integrating a RHOCS applicator with a commercially available MR imager. This can be considered as a disadvantage of open water bolus systems, with respect to closed water bolus systems.

To check correct patient positioning and detect shifts during treatment ultrasonic position verification is proposed as an alternative. The open water bolus is an ideal medium for non contact ultrasound imaging, due to the low attenuation of water for ultrasound waves (Webb, 1998). By selecting a suitable number of landmarks on bony structures in the planning image, the position of these landmarks can be verified in a number of ultrasound scans. The imaging can be performed without electronic disturbance during the short treatment interruptions for (invasive) temperature measurements. Commercially available linear array and sector scanners are suitable for this task. Thermometry in a RHOCS applicator will have to be performed with invasive means. However, preliminary results indicate that non invasive thermometry is also possible using ultrasound (Ebbini, 2000).

3.5   Conclusion

The proposed RHOCS applicator, operating at 150 MHz is a major improvement with respect to the Coaxial TEM, while retaining the advantages of the open water bolus. The bent patient posture causes no problem when a sufficiently large patient bore is selected. No SAR maxima at the bolus air interface have been observed.

SAR steering in the target area and local SAR reduction in several regions simultaneously is possible with a 3×6 RHOCS applicator. Extension of the number of antennas to 8 per ring does not merit the extra cost. The operating frequency is the prime design parameter, an optimum at 150 MHz is observed for central pelvic tumours. This frequency optimum is not sensitive to variation of the dielectric tissue properties.

The proposed Tumour, Muscle Maximum and Fat Maximum indices are useful parameters to evaluate applicator performance. The indices correlate well with relevant temperature indices.

Optimal SAR steering requires accurate patient positioning and reliable imaging in the treatment posture. This is a demanding technical problem yet to solve.

Chapter 4

Improvement of absorbing structures used in regional hyperthermia

Abstract Local pain is a major limiting factor in regional hyperthermia treatment wit radiative applicators. Absorbing structures, consisting of agar bound saline water, have been used successfully to reduce peripheral hot spots. However both clinical experience and simulation results indicate a SAR elevation in the tissue under the edges of the absorber block. This paper investigates the effect of modification of shape, position and spatial composition of the absorber blocks on the central attenuating effect and the SAR elevating effect at the edges. A selection from a set of five options is made using a phantom and a single ring dipole applicator. The simulations have been performed with the FDTD core of our regional hyperthermia treatment planning system. It is shown that tapering of the absorber edge and introduction of a water layer between the absorber and the skin can reduce the edge effect in the superficial fat layer by about 50% with respect to a rectangular absorber. A further reduction of 65% can be obtained by an absorber with an appropriate gradient of its conductivity along the length in the direction of the dominant $\vec{E}$-field. The modified absorbers produce a central attenuating effect comparable to the rectangular type. The use of a water layer type and a sigma gradient type absorber if also analyzed in a patient anatomy, both in the dipole ring applicator, operating at 70 MHz, as well as in a three ring Cavity Slot (CS) applicator, operating at 150 MHz. The mutual influence of phase-amplitude steering and the application of absorbers is investigated in the CS applicator. It appears that absorbers have a significant influence on the interference pattern in the patient model, possibly causing substantial reduction of the SAR value in the tumour and limiting the possibility of *ad hoc* application of absorbers. Re-optimization can only partly cancel this effect. Local SAR reduction by phase-amplitude control alone can match or improve the effect obtained with modified absorbers.

4.1   Introduction

In regional hyperthermia the majority of treatment sessions is limited due to localized pain caused by hot spots (Dinges *et al.*, 1998; Rau *et al.*, 1998). Wust *et al.* (1999) reported that in more than 80% of all patients treatment limiting hot spots occur. The hot spots are mainly located peripherally, inducing subcutaneous burns and skin blistering (Van der Zee *et al.*, 2000) or pain at the symphysis pubica, the crest of the pelvic bone or the lumbo-sacral region (Wust *et al.*, 1999; Van Vulpen *et al.*, 2002a).

In Chapter 2 it has been shown that rectangular, homogeneous absorbers with a thickness of 2–4 cm and a salinity of 36 gram l^{-1} can help in reducing these hot spots. In a study with 14 patients with a prostate carcinoma receiving regional hyperthermia treatment in the Coaxial TEM applicator, in 46 out of 70 treatment sessions in 12 patients local pain occurred (Van Vulpen *et al.*, 2002a). In most cases the use of an absorber reduced the local pain to an acceptable level. However, this effect was not in all cases lasting till the end of the treatment session, and a power reduction had to be performed. In about one third of the treatment sessions with an absorber, there were indications of pain at the edge of the absorber, despite the introduction of a water layer between the absorber and the skin during the later sessions. Some of the patients moved the absorber slightly to reduce this pain, which indicates the clinical relevancy of the edge effect. This edge related pain is probably caused by the SAR increase in the tissue under the edge of the absorber in the direction of the dominant $\vec{E}$-field (see Chapter 2).

The current paper investigates the possibility of reducing the edge effect by modification of the shape, position and spatial composition of the absorber. A quasi-static model is used to study the field distribution at the edge of the absorber and to device methods to improve this. Both a structured phantom and a patient model are used to evaluate the performance of modified absorbers, using the FDTD SAR model of our hyperthermia treatment planning system (Van de Kamer *et al.*, 2001a). The effect of modified absorbers is investigated both in a single ring applicator system, operating at 70 MHz and designed to approximate the Coaxial TEM system (De Leeuw and Lagendijk, 1987), as well as in a three ring, six antennas per ring Cavity Slot (CS) applicator system, operating at 150 MHz (see Chapter 3). In the three ring CS system the mutual influence of phase-amplitude steering and the application of absorbers is investigated.
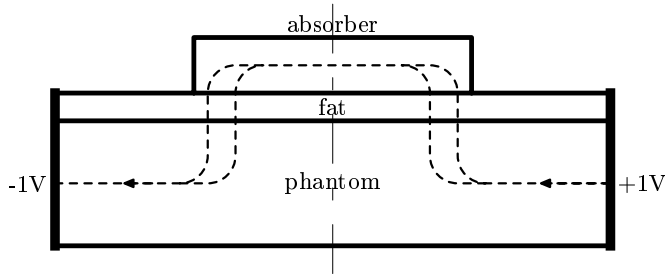
Figure 4.1: Set up of quasi-static study of absorber edge effects

4.2 Methods

4.2.1 Modified absorbers and Quasi-static modelling

At the lower RF frequencies absorbers can be considered to act as a shunt, diverting current from a muscle structure, due to its low impedance. The local reduction of current density in the muscle structure, centrally under the absorber causes a local SAR reduction. However, at the edges of the absorber an increase of the current density can occur, both in muscle as well as in the fat layer between muscle and absorber, causing an unwanted local increase of the SAR (see Chapter 2). It is hence likely that shape, position and/or composition of the absorber can influence this edge effect. This quasi-static concept of the working principle of an absorber is only used to qualitatively evaluate the effect of absorber modifications on the potential distribution at the absorber edge. As the wavelength at 70 MHz in muscle is about 50 cm, the dimensions of the set up exceed the commonly used scale for quasi static approximation of $\lambda/10$. The quasi-static results can, however be considered to be valid in the region of $\sim 5\,\mathrm{cm}$ around the absorber edge.

To study this problem at high resolution, a simplified set up is made of the direct surrounding of an absorber on a muscle-equivalent phantom structure, with a fat layer in between (figure 4.1). The phantom block has a length of 20 cm, a thickness of 4.5 cm and a width of 10 cm; the fat layer is 1 cm thick. The absorber has a length of 10 cm, a thickness of 2 cm and a width of 5 cm. The rest of the total simulation volume ($20 \times 10 \times 10\,\mathrm{cm}^3$) is filled with tapwater.

The potential distribution in this set up is calculated using our Quasar quasi-static model (De Bree *et al.*, 1996; Van de Kamer *et al.*, 2002b), with a resolution of 1 mm. An electric field is applied along the length of the set up by defining fixed potentials of respectively +1 V and -1 V at the right and left boundary of the set up. The operating frequency is set at 70 MHz, the dielectric properties of the materials are listed in table 4.1. Quantitative evaluation of the absorber efficacy is done using a FDTD model (section 4.2.2).
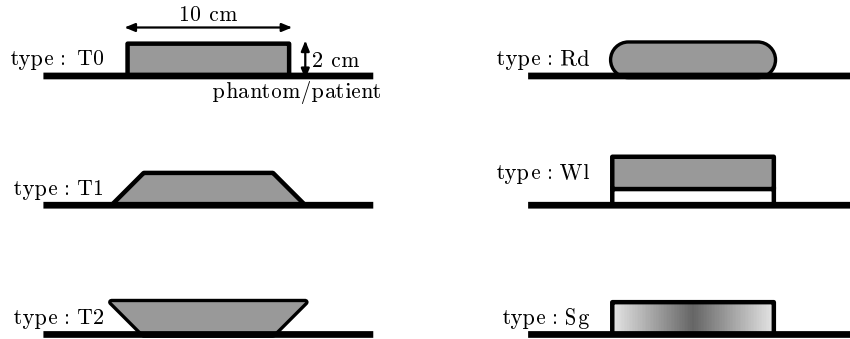
Figure 4.2: Various types of homogeneous absorbers with differ-
ences in shape (T0, T1, T2 and Rd), position (Wl), and
inhomogeneous conductivity (Sg)

Figure 4.2 shows cross sections of the modified absorbers under consideration:
the rectangular type T0 is equivalent to the previously tested types and used for
comparison. All absorbers have a thickness of 2 cm. The types T1 and T2 have a
tapering at the edges in the direction of the dominant $\vec{E}$-field, with respectively
the acute angle at the skin and in the water bolus. The Rd type has a rounded
edge with a radius of 1 cm. With the water layer (Wl) type, a layer of water is
introduced between the absorber and the skin of the patient. All homogeneous
absorbers have dielectric properties (see table 4.1) equivalent to a saline solution
of 36 gram l^{-1}. In a sigma gradient (Sg) absorber the salinity of the absorber
material is varied from 0.2 gram l^{-1} (tapwater) to 36 gram l^{-1} along the length
in the direction of the dominant $\vec{E}$-field. The pattern is symmetrical around the
central plane of the absorber with the highest conductivity in the centre.

4.2.2 Single ring dipole applicator and phantom

In the study of the homogeneous, rectangular absorber (see Chapter 2) the SAR
distributions in the phantom and a patient model have been determined in a
model of the Coaxial TEM applicator at a resolution of 1 cm. For an accurate
simulation of the edge effects of absorbers it is desirable to work at a high resolution
(Van de Kamer *et al.*, 2002b). The large dimensions of the Coaxial TEM structure
(~ 2 m) prevent simulation at high resolution. As alternative a circular dipole ring
(figure 4.3) with eight dipoles and a diameter equal to the Coaxial TEM (60 cm)
is employed. This allows simulation of the applicator-phantom system at 4 mm
resolution. The operating frequency is 70 MHz. The dipole ring applicator consists
of a plastic cylinder shell with a length of 80 cm and the thickness of 12 mm. The
cylinder is filled with tap water. The dipoles are formed by two metal bars with a
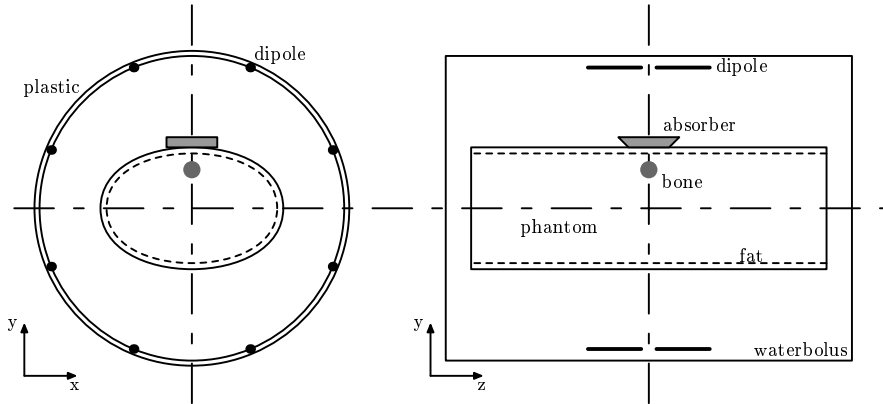
Figure 4.3: Dipole applicator with cylindrical water bolus and
elliptical phantom with T2 type absorber.

length of 12 cm attached to the inside wall of the plastic shell. Comparison of the
$\vec{E}$-field distribution in a phantom in both applicator types shows a fair similarity
(data not shown).

The dipole ring applicator is loaded with an elliptical phantom with a cross section
of 36×24 cm^2 and a length of 70 cm. The dielectric properties of the phantom
material (table 4.1) are equivalent to a saline solution of 3 gram l^{-1}. A fat layer
of 12 mm thickness is introduced in some of the simulations. To create a local
superficial SAR peak, like those frequently observed anterior to the pubic bone, a
bone sphere with a diameter of 34 mm is placed in some simulations in the central
plane of the phantom, at a depth of 12 mm under the fat-muscle boundary. The
applied absorbers have a width and average length of 10 cm and a thickness of
2 cm. Its longitudinal cross sections are 4 mm grid approximations of the shapes
in figure 4.2.

The SAR distribution in the phantom is evaluated along two tracks. The first SAR
profile is taken along a track centrally under the absorber, perpendicular to the
surface of the absorber, along the short axis of the phantom. This profile allows
evaluation of the reduction of the SAR value by the absorber in the superficial
and central regions. The second SAR profile runs along a track parallel to the
z-axis, 4 mm under the absorber. This track serves to assess the effect of the
absorber on the SAR distribution at the edges of the absorber. The track lies in
the central plane under the absorber, because in this plane the maximum edge
effect is expected (see Chapter 2).

4.2.3   Patient model

The patient model, figure 4.4, has been derived from a 40 cm CT dataset (slice thickness 5 mm) of a male patient with a prostate tumour. Both slices in figure 4.4 are displayed centrally through the tumour. The CT data set was segmented by Hounsfield Unit thresholding and down-scaled to $5\,\mathrm{mm}^3$ resolution, using the 'winner take all' algorithm (Van de Kamer *et al.*, 2001a). This method results in a patient model with regions that are assigned homogeneous dielectric properties (table 4.1). The values for tissue have been derived from literature (Gabriel *et al.*, 1996; Van de Kamer *et al.*, 2001e), those of saline water from Stogryn (1971). The tumour was manually outlined by a physician. The performance of absorbers on the patient model is evaluated along a transversal and a cranial-caudal subcutaneous track (see figure 4.4(b)). The subcutaneous track is located 15 mm below the skin, i.e. in the muscle layer directly under the fat layer, in the plane centrally under the absorber and follows the patient outline.

4.2.4   3D FDTD Simulations

The Finite Difference Time Domain (FDTD)-core of our Regional Hyperthermia Treatment Planning (HTP) system (Van de Kamer *et al.*, 2001a) was used to compute $\vec{E}$-field distributions in the phantom and the patient model. The number of iterations was 10000; convergence was tested by observing the time evolution of $|\vec{E}|$ at a test point in the patient and found to be stable within 0.1% of the end value.

In the dipole ring applicator all dipoles are excited coherently with eight sources placed in the gaps between the dipole bars, in order to mimic the $\vec{E}$-field distribution in the Coaxial TEM. The operating frequency is 70 MHz. The sources have an impedance of 50 Ω, implemented as described by Piket-May *et al.* (1994).The SAR distribution is computed from the $\vec{E}$-field distribution using:

$$\mathrm{SAR}(\vec{r}) = \frac{\sigma(\vec{r})}{2\rho(\vec{r})}\left|\vec{E}(\vec{r})\right|^2 \qquad (4.1)$$

In the Cavity Slot applicator, with three rings of 6 antennas per ring and operating at 150 MHz, the $\vec{E}$-field distribution is computed for each separate slot antenna. The active slot and dipole are excited with a source with an impedance of 50 Ω, generating a triple cosine pulse of unit amplitude, placed in the gap in the metal sheet halfway along the length of the slot. The inactive slots are terminated with the same impedance in order to achieve correct simulation of coupling effects between the antennas.

A typical $\vec{E}$-field computation requires about 200 MB RAM and takes about six hours on a 800 MHz standard personal computer, running GNU/Linux®. The
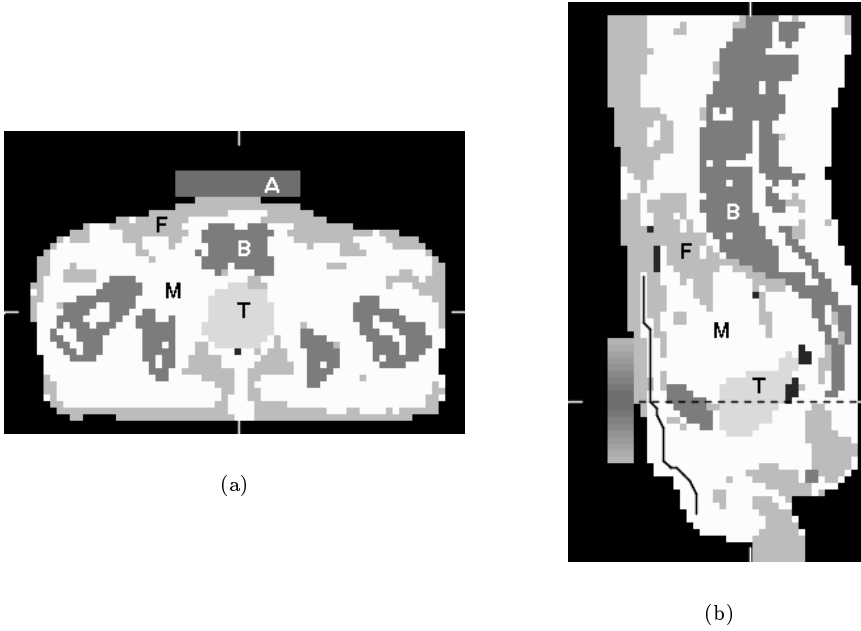
(a)

(b)

Figure 4.4: (a) Transversal and (b) sagittal slice of the patient
model with sigma gradient absorber (A). The patient model
is segmented in muscle (M), fat (F), bone (B) and tumour
(T). The black dashed and solid line indicate respectively
the transversal and subcutaneous SAR tracks used to eval-
uate the absorber performance.

SAR distribution for N $\vec{E}$-fields is computed according to equation (4.2) using a
steering vector $\mathbf{V}$, where $\mathbf{V}_i$ is the complex number representing the amplitude
and phase of each antenna (Sullivan *et al.*, 1993).

$$\mathrm{SAR}(\vec{r}) = \frac{\sigma(\vec{r})}{2\rho(\vec{r})} \left| \sum_i^N \vec{E}_i(\vec{r}) \, \mathbf{V}_i \right|^2 \tag{4.2}$$

In equation (4.2) $\mathrm{SAR}(\vec{r})$ is the SAR, $\vec{E}(\vec{r})_i$ is the $\vec{E}$-field for antenna i, $\sigma(\vec{r})$ and
$\rho(\vec{r})$ are respectively the conductivity and density of the voxel at $\vec{r}$. The steering
vector $\mathbf{V}$ is obtained by optimizing the ratio of SAR in the tumour and in muscle
and fat tissue (see Chapter 3).

All results of FDTD simulations are multiplied with a factor k to obtain a SAR value of $1\,\mathrm{W\,kg^{-1}}$ centrally in the phantom or the tumour in the situation without absorber. All simulations in the same configuration with an absorber are also normalized with the factor k. As both situations with and without absorber are excited with the same source amplitude, comparison of the normalized SAR curves demonstrates the effect of the absorber only.

Table 4.1: Dielectric properties of applicator and phantom materials and patient tissues at 70 MHz and 150 MHz

material/tissue	ε_r	$\sigma(\mathrm{S\,m^{-1}})$
tap water	76.5	0.042
deionised water	76.5	0.001
air	1.0	0
phantom	75.0	0.50
muscle	75.0	0.75
fat	10.0	0.06
bone	10.0	0.05
tumour	65.0	0.74
homogeneous absorber	65.7	6.33

4.3   Results

4.3.1   Quasi-static study

In figure 4.5(a) equipotential lines are shown in the right half of the quasi static absorber set up. The slice is taken in the central plane of the set up. As the set up is symmetric around the $y-$axis, it is sufficient to evaluate one half. The central plane at $z = 0$ is at zero potential; the right boundary at $x = 0.1\,m$ is at 1 V. The equipotential lines have an interval of 0.1 V. It can be seen that the high conductivity of the absorber bends the equipotential lines to exclude its boundary, causing a concentration in the fat layer near the absorber edge. As the current density $\mathbf{J} = -\kappa\nabla V$, with $\kappa = \sigma + j\omega\epsilon_o\epsilon_r$, a concentration of the equipotential lines indicates a region of high current density, and hence high SAR. Figure 4.5(b) illustrates that a T1 type tapering is not useful to suppress the edge effect. The acute angle of the absorber further concentrates the potential distribution. A T2 type absorber, however, does improve the edge effect (figure 4.5(c)). The rounding of the absorber edge (figure 4.5(d)) is also an improvement, but comparison with figure 4.5(c) suggests that the T2 type is slightly better.

From the results with the homogeneous absorber it appears that the major goal in the improvement of the edge effect is a redistribution of the current distribution. Removal of the edge of the absorber from the muscle-fat phantom, i.e. the
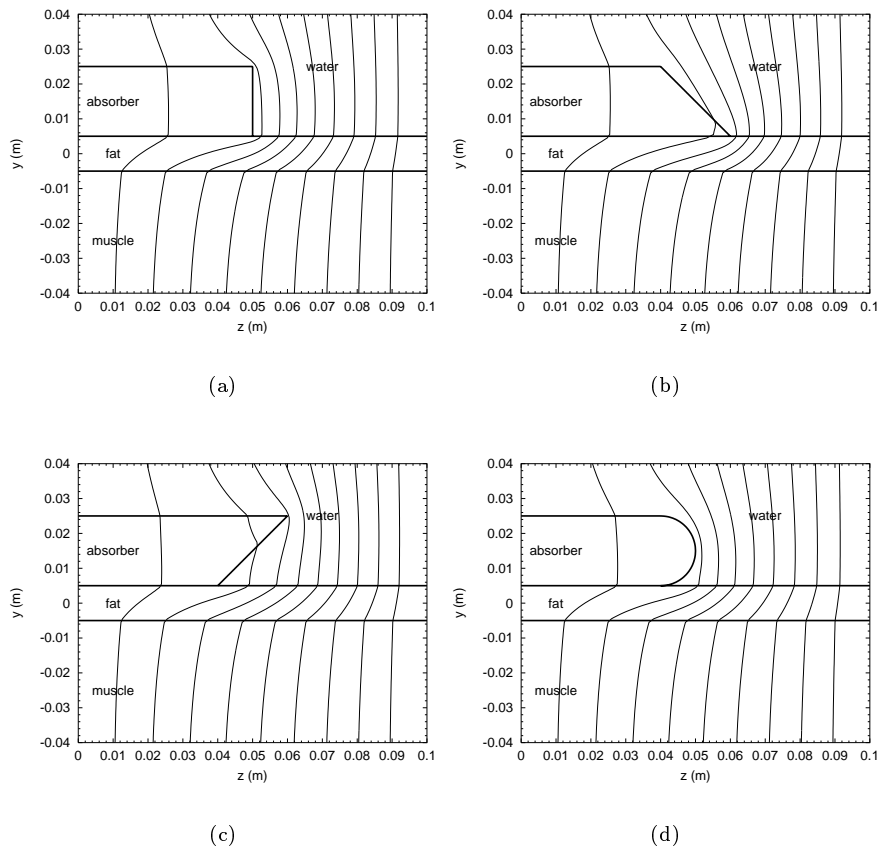
Figure 4.5: Influence of shape on the potential distribution at the edge of various absorber types: (a) rectangular, (b) T1 type, (c) T2 type and (d) round edge absorber

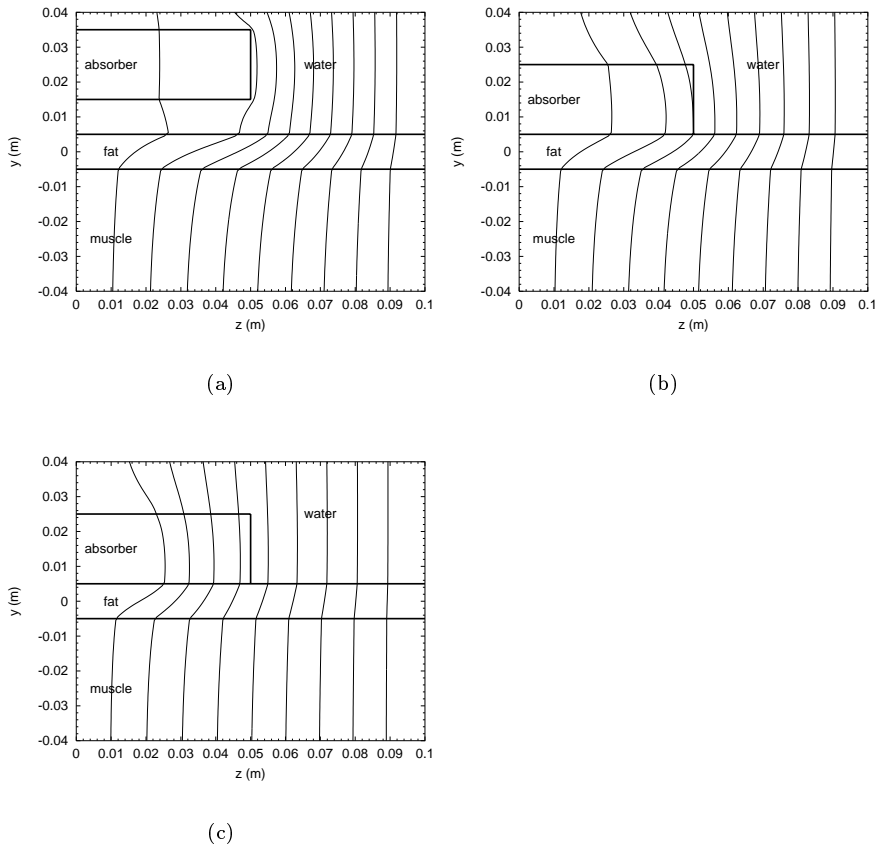(a)   (b)

(c)

Figure 4.6: Influence of position and composition on the potential distribution at the edge of various absorber types: (a) water layer, (b) linear sigma gradient and (c) sigmoid shaped sigma gradient absorber
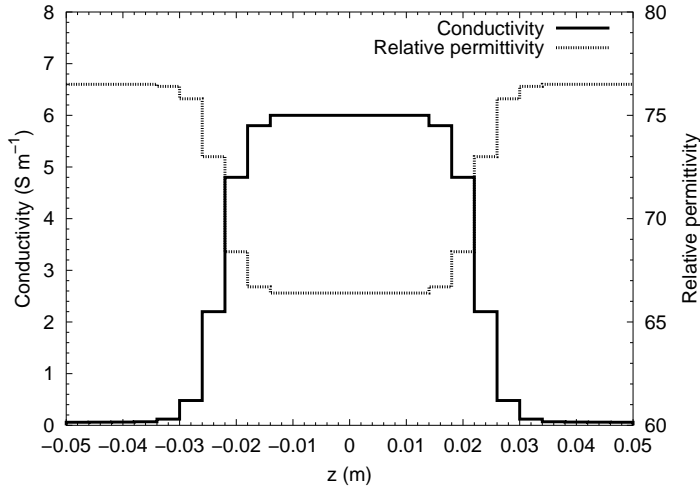
Figure 4.7: Distribution of conductivity and relative permittivity
in a sigma gradient absorber with a sigmoid profile.

introduction of a water layer between fat and absorber, is useful to obtain such a redistribution. However, from figure 4.6(a) it can be seen that the effect is roughly equal to the T2 type absorber. Increasing the thickness of the water layer might further decrease the current density at the edges, but might also influence the central SAR reducing capacity. This aspect is further studied using the FDTD model (section 4.3.2). A gradual onset of the conductivity of the absorber at its edge is probably the most fundamental way to influence the local current distribution. Figure 4.6(b) shows the potential distribution of an absorber with a linear gradient of its conductivity σ, ranging from 6 $\mathrm{S\,m^{-1}}$ centrally to 0.06 $\mathrm{S\,m^{-1}}$ at both edges. The sigma-gradient causes a more gradual decrease of the potential distribution, and hence the redistribution of the current from the muscle structure to the absorber. An even better distribution can be obtained by a sigma gradient that is shaped as a sigmoid curve (figure 4.6(c)). Figure 4.7 displays the discrete distribution of the conductivity over the length of the absorber. The relative permittivity has been computed from Stogryn (1971), assuming that the absorber is composed of agar solidified saline water. This type of sigma gradient absorber will be further analyzed with the FDTD model.

In the quasi-static results small peaks of the SAR in the fat layer under the corners of the absorbers can be observed (data not shown). These peaks can be up to twice the SAR value found in the central plane with the homogeneous type absorbers,

especially the T1 type absorber. The peaking is absent in the water layer and sigma gradient type absorbers.

4.3.2   Phantom study

Phantom without fat layer

Figure 4.8 shows SAR profiles in the phantom without fat layer with all absorber types in comparison with the SAR distribution without absorber. Figure 4.8(a) displays the SAR profile along a track centrally under the absorber along the short axis of the phantom. A reduction of the SAR value at the surface of the phantom of 80% is obtained. The attenuating effect is negligible at a depth of ~ 6 cm. This is in accordance with the value found in an earlier study, performed at a resolution of 1 cm (see Chapter 2). All types of absorbers exhibit a similar behavior along the transversal track, i.e. a large attenuation at the surface and a negligible effect in the central region. The sigma gradient absorber creates maximum attenuation at the surface and minimal attenuation centrally in the phantom.

However, large differences between the various absorber types can be observed in figure 4.8(b). The SAR profile along a track parallel to the z-axis, 4 mm under the absorber shows large peaks near the edges of the rectangular (T0) and T1-tapered absorbers, with values up to ten times the value without absorber. Application of T2-tapered, water layer and sigma gradient absorber results in a major reduction of these peaks. In all absorbers the edge effect is maximal under the centre-line of the absorber, no peaking at the edges is observed (data not shown).

Phantom with fat layer

In figure 4.9 the effect of several types of absorbers on a phantom with a 12 mm fat layer is depicted. The fat layer substantially reduces the attenuating effect centrally under the absorber (figure 4.9(a)), irrespective of the absorber type. The longitudinal SAR tracks, both in muscle-like phantom material at a depth of 16 mm (figure 4.9(b)) and in the fat layer at a depth of 4 mm under the absorber (figure 4.9(c)) reveal a reduction of the peaks at the edges of the modified absorbers. In accordance with the quasi-static results the T1 type absorber increases the edge effect, where the T2 and decreases it. The round edge (Rd) type performs slightly worse in comparison to the T2 type. The effect of the water layer type (Wl) is almost equal to the T2 type absorber. The best reduction of the edge effect is obtained by the sigma gradient absorber.

Phantom with bone obstruction

The introduction of a sphere of bone equivalent material 12 mm under the fat-muscle boundary creates a local, superficial SAR peak (figure 4.10(a)). In this
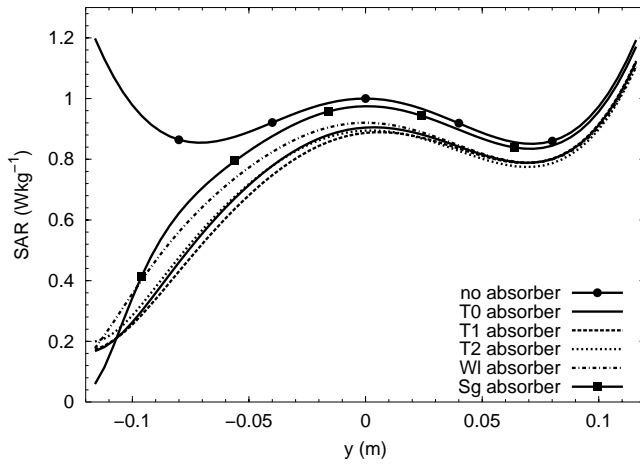
(a)
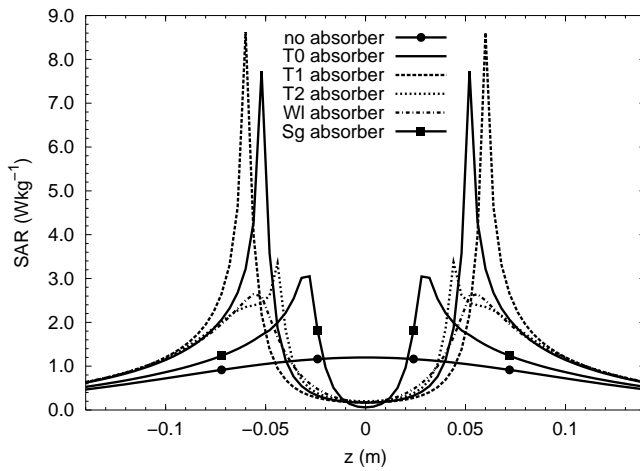
(b)

Figure 4.8: SAR tracks in phantom in dipole ring applicator, effect of various absorber types, (a) transversal track centrally under the absorber, (b) along z-axis 4 mm under absorber

(a)

(b)

(c)

Figure 4.9: SAR tracks in phantom with fat layer in dipole ring
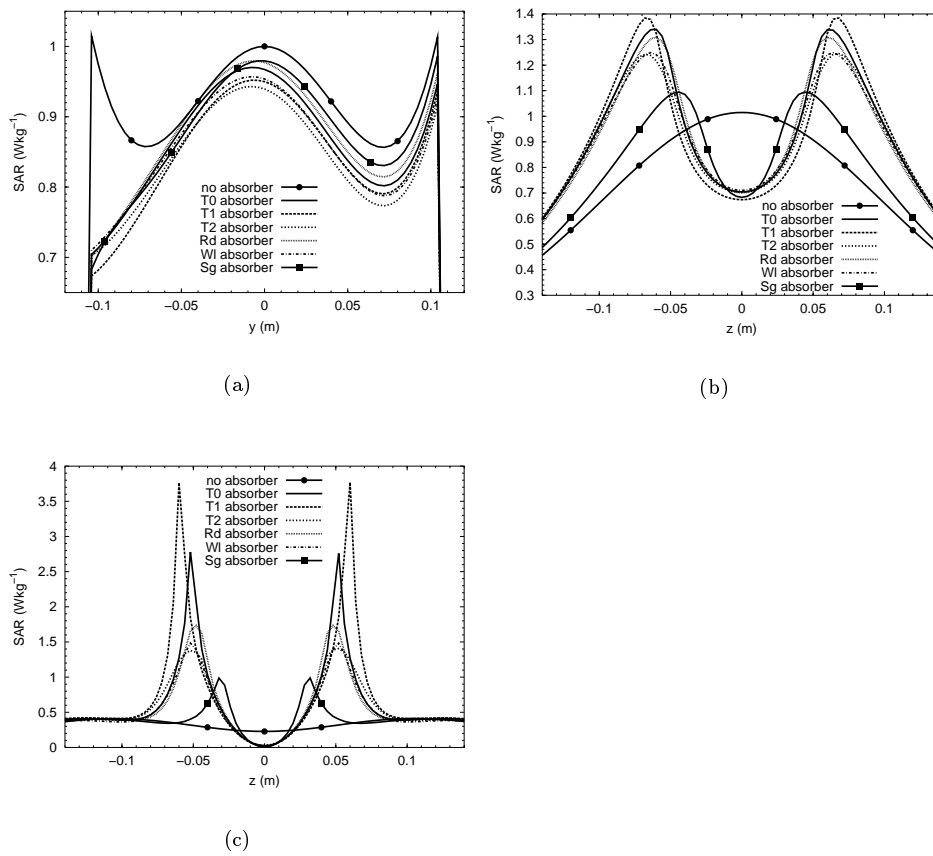applicator, effect of various absorber types, (a) transversal
track centrally under the absorber , (b) along z-axis in mus-
cle (depth 16 mm), (c) along z-axis in fat (depth 4 mm)

case the evaluation of the T1-tapered absorber has been left out, because of the enhancement of the edge effect caused by this absorber type in the previous simulations. All modified absorber types accomplish a reduction of SAR of about 25% in the superficial muscle layer between fat and bone, however, no attenuating effect is achieved in the muscle equivalent phantom material behind the bone sphere. The ability to suppress the edge effect of the various absorber types is not influenced by the presence of the bone sphere.

Influence of the thickness of the water layer

In figure 4.11 the influence of the thickness of the water layer on the performance of an absorber is investigated. In figure 4.11(a) it can be seen that an increase of the thickness of the water layer from 4 mm to 20 mm has a slight deteriorating effect on the attenuating effect of the absorber. An absorber with a water layer of 8 mm has an almost equal attenuating effect as a sigma gradient absorber. The thickness of the water layer has a major influence on the edge effect. Selecting a water layer of 20 mm can reduce the edge effect more than a sigma gradient absorber.

4.3.3 Patient study

In the patient study, only the effect of the water layer and the sigma gradient absorbers are evaluated, compared to the rectangular homogeneous type (T0). The phantom study showed an increase of the edge effect for the T1 tapered type, a moderate improvement for the Rd type and a comparable behavior of the T2 and the Wl type absorbers. Hence the analysis of the T1, T2 and Rd type would be superfluous.

Figure 4.12 shows the SAR profiles in the dipole ring applicator along the selected tracks in the patient model. A high SAR peak is located in the narrow muscle strip, anterior of the pubic bone (figure 4.12(a)). Note the similarity of this peak with the maximum created by the spherical bone object in the phantom study (figure 4.10). Both water layer and sigma gradient absorbers reduce this peak by about 27%, compared to a reduction of 42% by the T0 type absorber. However the magnitude of the peak is still twice the SAR value centrally in the tumour. The reduction of the SAR value in the tumour is slightly larger for the water layer absorber in comparison with the sigma gradient type. The SAR pattern along the subcutaneous track (figure 4.12(b)) is complicated, due to the heterogeneous composition of the patient. However, it can be seen that an edge effect is present at the cranial side of the absorbers. The sigma gradient absorber increases the local SAR value by about 25% above the upper edge of the absorber, the water layer absorber causes an increase of about 75% at the same location. At the caudal

(a)

(b)

(c)
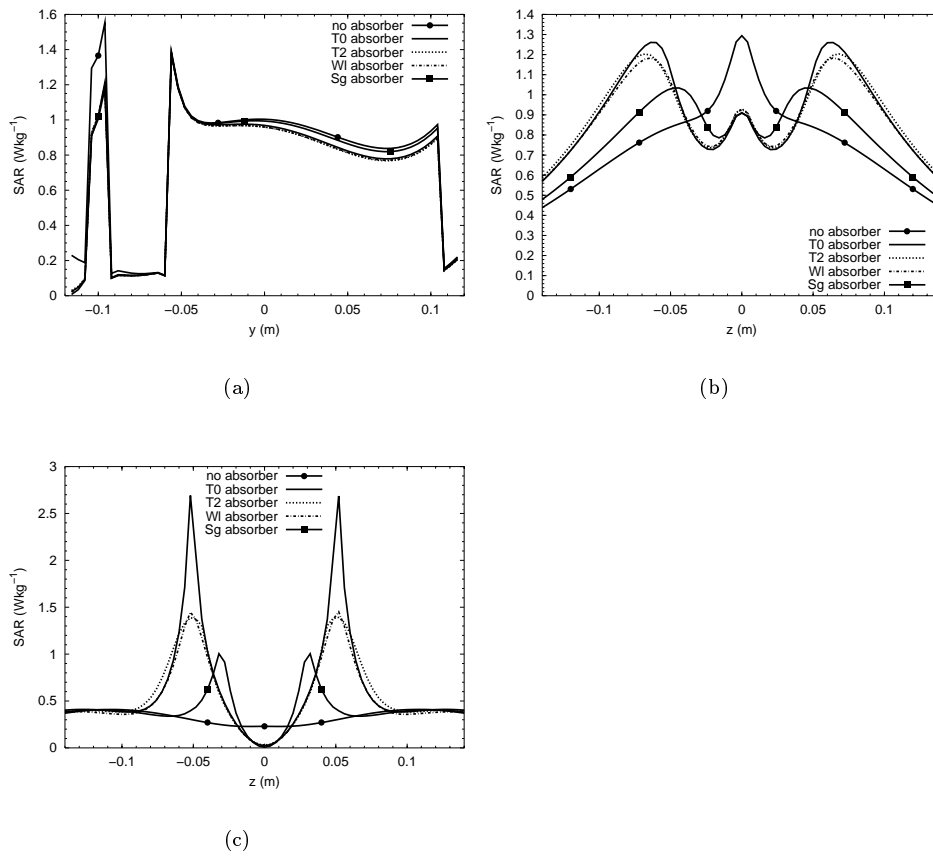
Figure 4.10: SAR tracks in phantom with spherical obstruction in dipole ring applicator, effect of various absorber types, (a) transversal track centrally under the absorber , (b) along z-axis in muscle (depth 16 mm), (c) along z-axis in fat (depth 4 mm)

(a)

(b)

(c)
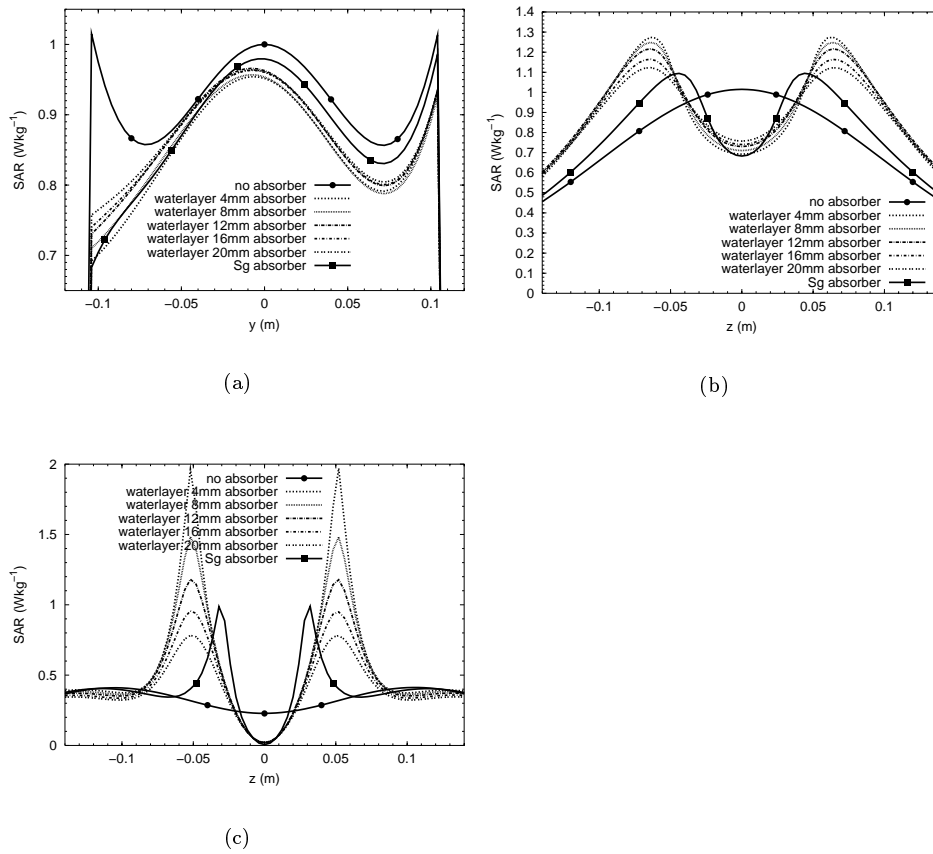
Figure 4.11: SAR tracks in phantom with fat in dipole ring applicator, effect of the thickness of the water layer, (a) transversal track centrally under the absorber , (b) along z-axis in muscle (depth 16 mm), (c) along z-axis in fat (depth 4 mm)
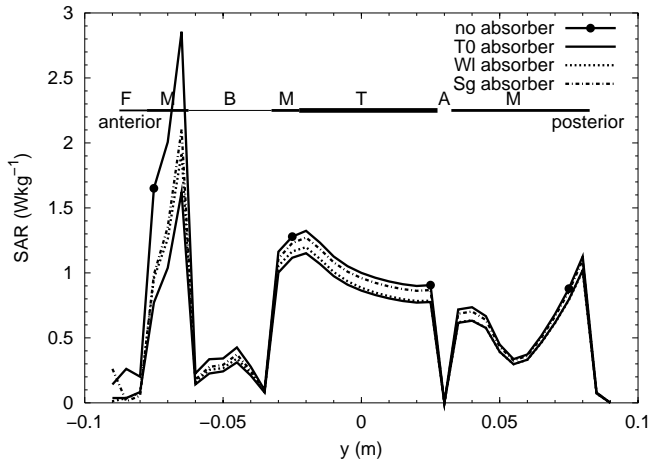
(a)
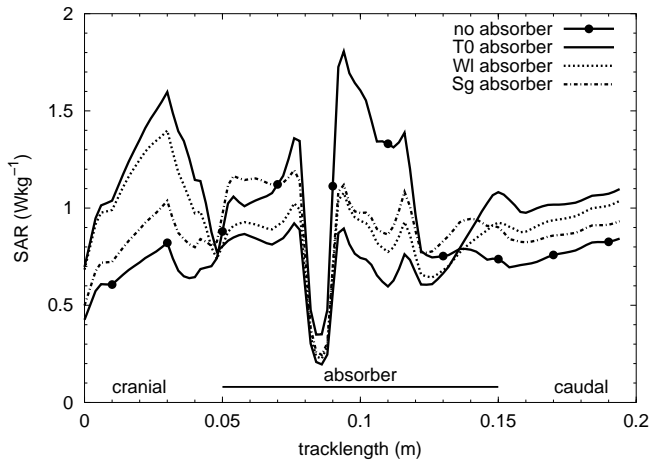
(b)

Figure 4.12: SAR tracks in patient in dipole ring applicator, effect of water layer (Wl) and Sigma gradient (Sg) absorber, (a) anterior-posterior centrally in the tumour, tissue along the track indicated as muscle(M), fat(F), bone(B) and air(A), (b) cranial-caudal subcutaneous profile.

edge of the modified absorbers, however, only a small elevation of the local SAR can be observed, that is about half the effect of the T0 type absorber. Due to the curved form of the lower abdomen the absorber is not in direct contact with the skin, lowering the edge effect of the absorbers.

The effect of modified absorbers on the patient model has also been investigated in the 3 ring RHOCS applicator (see Chapter 3), operating at 150 MHz. In figure 4.13 the SAR distribution is shown. After optimization of the ratio of SAR in tumour versus muscle and fat the SAR peak ventral of the pubic bone is reduced by about 20% with respect to the value in the dipole ring applicator (figure 4.13(a)). Application of absorbers results in a further decrease of the anterior peak: the sigma gradient absorber yields a reduction of 27%, the water layer and the T0 type absorbers produce a remarkable reduction of 61%. The latter absorbers also cause a reduction of 28% centrally in the tumour. This reduction can, however, be compensated with an increase of the total power. The SAR along the subcutaneous track (figure 4.13(b)) indicates a substantial reduction with respect to the distribution without absorber for the water layer absorber. The sigma gradient absorber,however, creates a remarkable increase of the SAR of about 57% at its caudal end. Both at the cranial and caudal end the edge effect of the sigma gradient absorber is large compared with the T0 and Wl type absorbers.

It has to be noted that in the previous evaluation of absorbers the steering vector **V** has not been changed after the introduction of absorbers. It is likely that the $\vec{E}$-field distribution of some of the antennas is influenced by the presence of a conducting structure and that the interference pattern is negatively affected. This assumption has been tested by re-optimizing the SAR distribution in the presence of the T0, Wl and Sg absorber types. Figure 4.14 gives the SAR profiles after re-optimization, normalized for an equal total power. In the distribution with the sigma gradient absorber the anterior peak is further reduced with 43%, however with a slightly lower SAR centrally in the tumour. The SAR distribution along the transversal track with the water layer absorber is hardly affected by the re-optimization process. For comparison a re-optimization has also been performed with the aim of decreasing the SAR in the problem region anterior of the pubic bone by phase-amplitude control only. Chapter 3 described the ability of the three ring cavity slot applicator of local SAR reduction (LSR) by assigning an extra weight to a certain region in the object function of the optimization. In figure 4.14 it can be seen that LSR can reduce the anterior peak to the same value attained by the water layer absorber, with a higher and more homogeneous SAR in the tumour. The SAR distribution along the subcutaneous track (figure 4.14(b)) is improved for all absorber types by the re-optimization, however, the minimal values are obtained after LSR optimization.
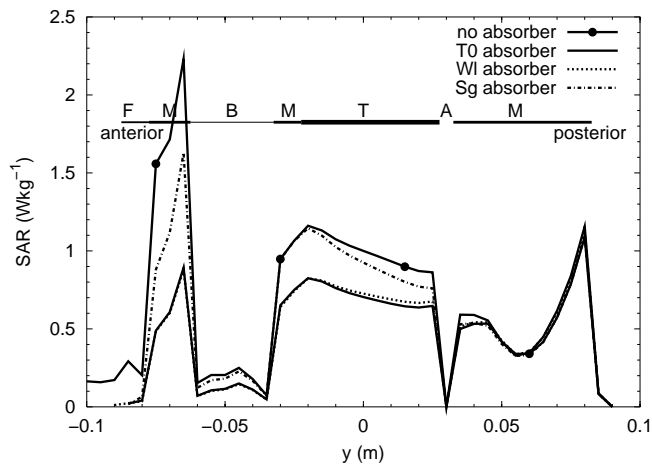
(a)
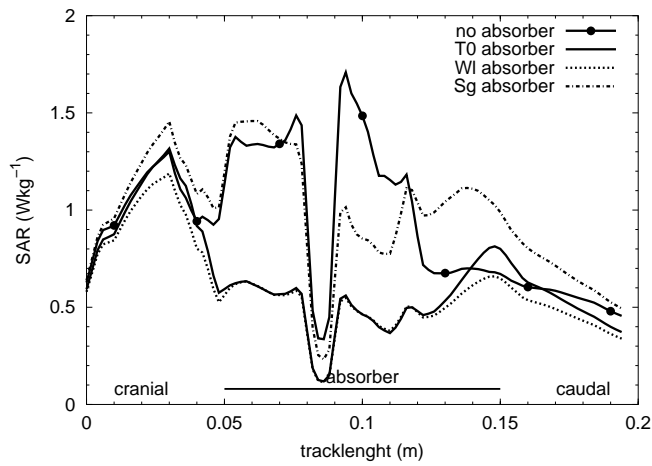
(b)

Figure 4.13: SAR tracks in patient in RHOCS applicator, effect of water layer (Wl) and Sigma gradient (Sg) absorber, (a) anterior-posterior centrally in the tumour, tissue along the track indicated as muscle(M), fat(F), bone(B) and air(A), (b) cranial-caudal subcutaneous profile.

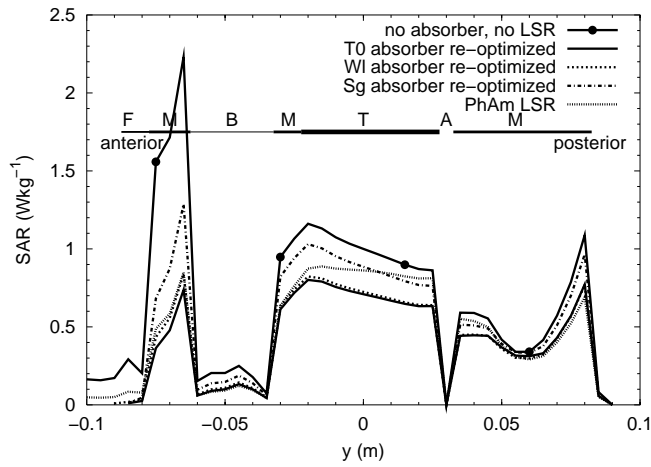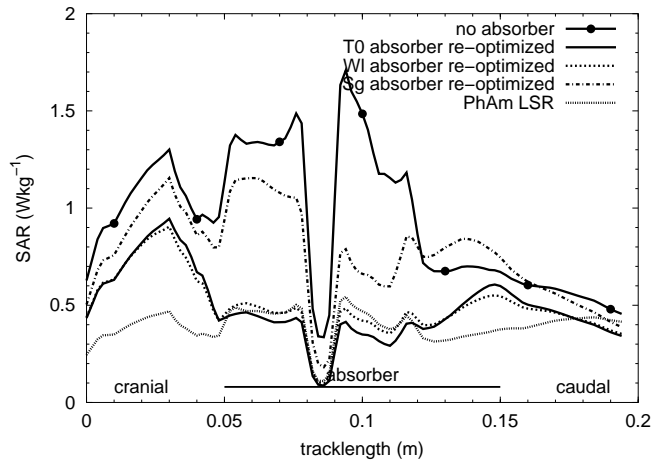(a)

(b)

Figure 4.14: SAR tracks in patient in RHOCS applicator, effect
of water layer (Wl) and Sigma gradient (Sg) absorber after
re-optimization and Local SAR Reduction (LSR) by phase-
amplitude (PhAm) control, (a) anterior-posterior centrally
in the tumour, (b) cranial-caudal subcutaneous profile.

4.4   Discussion

Clinical experience indicates that the increase of the SAR near the edges of the absorber has a negative influence on the use of absorbers during regional hyperthermia. This paper investigates the effect of variations in shape, position and composition of absorbing structures on the SAR distribution during regional hyperthermia.

Using a quasi-static model it is demonstrated that appropriate tapering and rounding of the absorber edge can improve the current distribution in the fat layer under the absorber edge and reduce the local SAR value. Introduction of a water layer between muscle and fat also serves to obtain this effect. A variation of the conductivity of the absorber along a sigmoid profile leads to the best reduction of the dissipation in the fat layer.

Using an elliptical phantom and the dipole ring applicator it is demonstrated that the superficial attenuation centrally under the absorber depends mainly on the presence of the fat layer. Variations in shape, water layer or sigma gradient have no major effect on the efficacy of the absorber, c.q. the ability to reduce a superficial SAR maximum. However, modification of the shape, introduction of a water layer and a sigma gradient have a major influence on the edge effect. A tapered absorber with the acute angle at the skin (T1 type) does not reduce the edge effect of an absorber. Inversion of the tapered absorber reduces the edge effect to a level comparable with the water layer type. Rounding of the absorber edge has less effect. The best result is obtained with a sigma gradient absorber. These results are in accordance with the results of the quasi-static study. Both the water layer and the sigma gradient absorbers can reduce a superficial SAR peak, caused by the introduction of a bone sphere in the phantom, to the level observed without the bone sphere.

Increasing the thickness of the water layer has a slight deteriorating influence on the central, attenuating effect. The edge effect can be decreased by an increase of the thickness up to 20 mm. The best trade off between central and edge effect is obtained with a thickness of 8 to 12 mm.

In a patient model in the dipole ring applicator a similar behavior of the modified absorber types is observed. A reduction of about 30% can be obtained in the SAR peak ventral of the pubic bone, with a negligible reduction of the SAR in the tumour. The edge effect at the cranial side of the absorber is minimal with the sigma gradient absorber. In a three ring cavity slot applicator, operating at 150 MHz, the effect of both absorber types is quite differently. There is a marked difference in the effect on the SAR peak at the pubic bone. The water layer absorber creates a high attenuation in comparison to the sigma gradient absorber. Furthermore the sigma gradient absorber causes a remarkable high edge effect. This indicates that both

modified absorber types have a different effect on the SAR pattern created by the 150 MHz three ring applicator system, indicating that the quasi-static approach is no longer valid at this frequency. The increase of the operating frequency might also negatively affect the field pattern at the edges of the absorber. This suggests that *ad hoc* application of absorbers to reduce local pain is not a viable option in a phase-amplitude controlled applicator.

After re-optimization there is still a noticeable difference between both absorbers, both with respect to the effect on the pubic bone peak and to the edge effect. Contrary to the results obtained in the single ring dipole applicator the water layer absorber performs better. However, it has to be noticed that re-optimization with an absorber in place requires recalculation of the $\vec{E}$-field distribution for all antennas, which is a large computational effort. It is therefore remarkable to observe that local SAR reduction by phase-amplitude control can generate even better results in terms of reduction ventral of the pubic bone, reduction of edge effect and SAR distribution in the tumor region. Local SAR reduction requires no field re-computation, but only a straightforward re-optimization with a different objective function.

A water layer absorber can be made by combining a homogeneous saline agar block with a sheet of agar bound water. This type of absorber, with a waterlayer of 10 mm, is now clinically used during hyperthermia treatments with the Coaxial TEM applicator. However, it might be better to create the water layer by putting a few stand off studs of water equivalent material. This allows both skin cooling and cooling of the absorber itself by the free flowing bolus water. This might help to reduce the skin erythema that is sometimes observed after the use of absorbers (Van Vulpen *et al.*, 2002a). This effect should be studied further in a thermal model.

4.5 Conclusion

In this paper the improvement of absorbing structures used during regional hyperthermia is studied. Both a phantom and a patient study indicate that in a single ring applicator system operating at 70 MHz a sigma gradient absorber creates a similar reduction of superficial SAR peaks, compared to a homogeneous absorber and, in addition, minimizes the SAR elevation at the edges of the absorber. Both introduction of a water layer and a tapering of the absorber edge have less effect on the edge elevation. The quasi-static study indicates that at the lower RF frequencies the effective mechanism of an absorber is the rerouting of current, with an inherent concentration at the edges. With a sigma gradient absorber an optimal dispersion of this current can be obtained. A total annihilation of the edge effect is not possible.

In multi ring applicator systems, that employs phase-amplitude steering of the SAR distribution at 150 MHz, simple application of absorbers might lead to unexpected effects, in particular a deterioration of the SAR in the tumour. Re-optimization with the absorber in place can partly cancel this effect, but requires a time consuming computational effort. This method will not be practically usefull. Local SAR reduction by phase-amplitude control alone can match or improve the results obtained with improved absorbers. At least the same attenuation in the region of local pain can be obtained without any elevation of the SAR level in the surrounding regions.

Chapter 5

Treatment planning for capacitive regional hyperthermia

Abstract Capacitively coupled hyperthermia devices are widely in use, mainly in Asian countries. In this paper a comprehensive treatment planning system, including a Specific Absorption Rate (SAR) and thermal model for capacitively coupled hyperthermia is described and demonstrated using a heterogeneous patient model. In order to accurately model a hyperthermia treatment, simulation at high resolution is mandatory. Using the quasi-static approximation, the electromagnetic problem can be solved at high resolution with acceptable computational effort. The validity of the quasi-static approximation is demonstrated by comparing the Maxwell solution of a phantom problem to the quasi-static approximation. Modelling of capacitive hyperthermia of the prostate reveals the difficulty of heating deep seated tumours in the pelvic area. Comparison of the SAR distribution in the heterogeneous patient model and a patient shaped agar phantom shows a shielding effect of the pelvic bone and the influence of the fat-muscle distribution. It is shown that evaluation of capacitive hyperthermia with agar phantoms leads to overly optimistic conclusions. Therapeutic relevant tumour temperatures can only be obtained by permitting temperature extrema in normal tissue. This concurs with clinical practice, where treatment limiting hot spots restrict the tumour temperature. It is demonstrated that the use of very cold overlay bolus bags has only a very superficial effect. The presented model can be used for individual treatment planning and optimization, for the evaluation of capacitive applicator modifications and comparison with other devices.

5.1   Introduction

Regional hyperthermia is widely used as an adjuvant therapy to radiotherapy for advanced pelvic tumours. The positive effect of regional hyperthermia was confirmed in two randomized studies (Van der Zee *et al.*, 2000; Harima *et al.*, 2000). The study of Van der Zee *et al.* (2000) used several radio frequency (RF) radiative annular ring applicators, whereas Harima *et al.* (2000) used the Thermotron RF8 system (Yamamoto VINITA Co., Osaka, Japan). The RF8 system is a capacitive heating device operating at 8 MHz, where the patient is placed between two electrodes connected to a high power RF generator. The patient is coupled to the electrodes with bolus bags, containing saline water at low temperature. The Thermotron RF8 device is mainly in use in Asian countries; the average Asian patient is considered to be very suitable for capacitive hyperthermia due to its slender appearance.

A clinical comparison between the Thermotron RF8 system and an early radiative annular ring applicator, the Annular Phased Array System (APAS) (Turner, 1984) was made by Egawa *et al.* (1988). The study concluded that both systems have advantages and disadvantages, and did not indicate either of the systems as superior. This lead to a further development of both capacitive and radiative hyperthermia systems.

The ESHO quality assurance guidelines for Regional Hyperthermia (Lagendijk *et al.*, 1998) highly recommend the use of 3D treatment planning. While 3D treatment planning systems for RF radiative annular ring applicators are amply available (Sullivan, 1991; Clegg *et al.*, 1996; Wust *et al.*, 1996; Paulsen *et al.*, 1999; Van de Kamer *et al.*, 2001a), only a few Specific Absorption Rate (SAR) models for capacitively coupled hyperthermia in a structured patient have been described. The system described by (Armitage *et al.*, 1983) was limited to a few slices of interest, due to the then available limited computer resources. Orcutt and Gandhi (1990) used the impedance method to compute the power deposition in a crude model of the human body. Sowinski and Van den Berg (1990) introduced an efficient three-dimensional iterative scheme to solve quasi-static field problems and applied this technique to model a capacitive ring applicator.

Van de Kamer *et al.* (2002a) have demonstrated the need for high-resolution regional hyperthermia treatment planning. At the high frequencies used for radiative regional hyperthermia this can be done by using a FDTD model in combination with a quasi-static zooming technique (Van de Kamer *et al.*, 2001b), which reduces the long computation times required to solve the electromagnetic problem at a sufficiently high resolution. At the lower frequencies, used in capacitively coupled hyperthermia ($\leq 27.12\,\mathrm{MHz}$), the effective wavelength in tissue is much longer than the dimensions of the tissue model. This indicates that a quasi-static approximation of the problem is allowed. Armitage *et al.* (1983) and Orcutt and

Gandhi (1990) assumed the quasi-static approximation to be valid for a model of respectively the human thorax and the abdomen at 13.56 MHz, Sowinski and Van den Berg (1990) found good agreement between the quasi-static method and the integral equation method (i.e. a full Maxwell solution) in a layered model of the human thigh in a ring applicator, operating at 27.12 MHz. The current paper investigates the validity of the quasi-static approximation for low frequency capacitive heating devices, by comparing the static analytic solution of a simple problem with the FDTD solution of the Maxwell equations.

None of the aforementioned treatment planning systems for capacitively coupled hyperthermia incorporate a thermal model. In this paper a high resolution 3D treatment planning system for capacitively coupled hyperthermia, consisting of a quasi-static SAR model and a thermal model is introduced. Both the SAR model and the thermal model are demonstrated using a patient anatomy.

5.2 Validation

5.2.1 Methods

The electromagnetic field in a tissue volume coupled to any type of hyperthermia applicator is described by the Maxwell equations, which can be numerically solved in differential (Paulsen and Ross, 1990; Sullivan, 1991) or integral form (Wust *et al.*, 1993; Zwamborn *et al.*, 1991). If the volume of interest is small in comparison to the wavelength a quasi-static approximation, $\nabla \times \mathbf{E} = 0$ can be used (Dirks, 1988; Hand *et al.*, 1991), resulting in a substantial reduction of the computational complexity with respect to the various Maxwell models (Van de Kamer *et al.*, 2001d). Currently, in capacitive tissue heating a frequency of 8 MHz to 13.56 MHz is used, resulting in a wavelength of 3.0 m to 1.75 m in muscle tissue. In order to test whether the quasi-static approximation is valid in this frequency range for tissue models of human size, the analytic solution of the potential distribution around a spherical object placed in an other medium to which a uniform electric field is applied is compared to the numerical Maxwell solution, computed using the FDTD method (Taflove, 1995). Correspondence between the analytical solution and the FDTD results indicates the validity of the use of the quasi-static approximation in this case.

The analytic solution is also compared with the results of an iterative solution of the quasi-static potential distribution (Sowinski and Van den Berg, 1990), calculated with the QUASAR model (De Bree *et al.*, 1996). Correspondence between the analytical solution and the QUASAR results validates the use of QUASAR to compute power density distributions in heterogeneous anatomies.

Analytical solution

The potential distribution around a spherical object with radius R, placed in a uniform electric field E_z is (Jackson, 1975; De Bree *et al.*, 1996)

$$V(x, y, z) = \begin{cases} \frac{-3\kappa_i}{\kappa_i + 2\kappa_e} E_z z & \text{inside sphere} \\ \left(\frac{\kappa_i - \kappa_e}{\kappa_i - 2\kappa_e} \frac{R^3}{r^3} - 1\right) E_z z & \text{outside sphere} \end{cases} \tag{5.1}$$

where E_z is assumed to be oriented along the $z-$axis, the origin is at the centre of the sphere, r is the distance from the origin and κ_i and κ_e are respectively the complex admittance of the medium inside and outside the sphere, with $\kappa = \sigma + j\omega\epsilon_o\epsilon_r$.

From this expression the power density can be calculated as

$$PD(x, y, z) = \frac{1}{2}\sigma|\nabla V|^2 \tag{5.2}$$

Outside the sphere ∇V works out to

$$\begin{aligned} \nabla V(x, y, z) \quad &= \frac{\kappa_i - \kappa_e}{\kappa_i - 2\kappa_e} \frac{R^3}{r^5}(-3xyE_z\vec{x} - 3yzE_z\vec{y}) \\ &+ \left(\frac{\kappa_i - \kappa_e}{\kappa_i - 2\kappa_e}\left(\frac{R^3}{r^3} - 3\frac{R^3 z^2}{r^5}\right) - 1\right)E_z\vec{z} \\ \text{with} \quad r &= \sqrt{x^2 + y^2 + z^2} \end{aligned} \tag{5.3}$$

Inside the sphere the power density is

$$PD_{\text{sphere}} = \frac{1}{2}\sigma\left|\frac{-3\kappa_e}{\kappa_i + 2\kappa_e}E_z\right|^2 \tag{5.4}$$

Phantom setup

For the purpose of this test the homogeneous E_z-field is assumed to be present between two cylindrical capacitor plates (figure 5.1(a)), with between them a cylinder of equal diameter of a material with a high permittivity ($\varepsilon_r = 149$) and conductivity ($\sigma = 0.62\,\text{S}\,\text{m}^{-1}$), i.e. muscle like. The sphere is fat-like material ($\varepsilon_r = 29.6$, $\sigma = 0.053\text{S}\,\text{m}^{-1}$). The axis of the cylinder is along the $z-$axis. The operating frequency is 13.56 MHz. The validation is performed in three phantoms of different dimensions, denoted as A, B and C. Table 5.1 gives the dimensions of the phantoms.

(a)

(b)
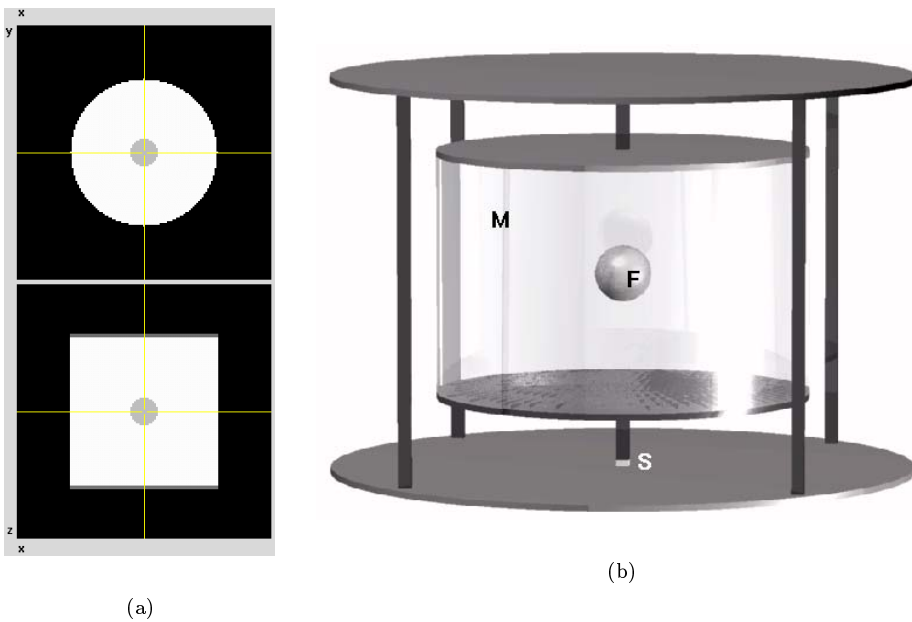
Figure 5.1: Phantom setup used in (a) the Quasar simulation of a muscle (white) equivalent phantom with an inserted fat (gray) sphere between capacitor plates, radial (top) and axial (bottom) cross section, and (b) the extended setup of the muscle (M) equivalent phantom with the fat sphere (F), with a metal (dark gray) cage construction used in the FDTD simulation. The bottom source (S) can be seen between the bottom plate and the connecting rod, a similar source is placed under the top plate.

Table 5.1: Dimensions and dielectric properties of the phantom setups

phantom	diameter (cm)	height (cm)	R_{sphere} (mm)
A	30	20	22.5
B	40	40	40
C	40	80	55

QUASAR and FDTD simulations

In the FDTD simulations (Van de Kamer *et al.*, 2001a) the phantom with capacitor plates was surrounded by a metal cage construction (see figure 5.1(b)), in order to supply a return path for the current generated by the sources. The sources are placed between the top and bottom plates of the cage construction and the rods extending from the capacitor plates connected to the phantom. This configuration places the cage construction at a zero potential. The FDTD power density distributions were normalized for equal absorbed power in the phantom with respect to the analytic solution. Convergence of the simulation was tested by observing $|\vec{E}|$ at a test point in the muscle phantom. The number of iterations was set at 10000, in all cases the value of $|\vec{E}|$ at the test point was stable within 0.1% of the end value.

In the QUASAR simulations cylindrical plates at the top and the bottom of the phantom (see figure5.1(a)) were set at a constant potential 1 V, respectively -1 V. This defines $E_z = \frac{2}{\text{heigth}}$. With this E_z there is numerical correspondence without scaling between the analytic solution and the QUASAR simulation. The boundary of the simulation domain is at zero potential. The error norm in the QUASAR simulations (De Bree *et al.*, 1996) was set at 2×10^{-10}, the number of iterations varied between 1500 and 2500.

To evaluate the performance of the Quasar and FDTD simulations, the relative, averaged absolute difference is calculated in the phantom. To assess the behaviour of the simulations at the muscle-fat boundary a sphere shell with a thickness of 2 cm is defined, extending 1 cm both into muscle and fat. The boundary specific relative, averaged absolute difference is calculated in this sphere. The relative, averaged absolute difference Q is defined as (Van de Kamer *et al.*, 2001e):

$$Q_V = \frac{\sum |\text{PD}_i - \text{PD}_{i,\text{ref}}|}{\sum |\text{PD}_{i,\text{ref}}|} \tag{5.5}$$

The sums are taken over all voxels i in the volume V, 'ref' indicates the reference distribution, i.e. the analytic solution.

Figure 5.2: Comparison of Quasar and FDTD simulation with a resolution of 5 mm in phantom A at 13.56 MHz with an analytical solution. The tracks are taken along the (a) central $x-$axis and (b) $z-$axis.

Figure 5.3: Comparison of Quasar and FDTD simulations with a resolution of 2 mm in phantom A at 13.56 MHz with an analytical solution.

(a)   (b)

Figure 5.4: Comparison of Quasar and FDTD simulation with a
resolution of 5 mm in phantom B at 13.56 MHz with an
analytical solution.

(a)   (b)

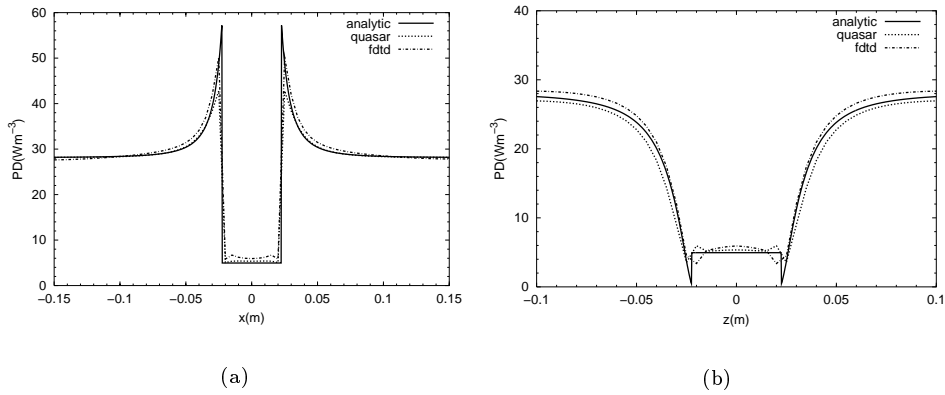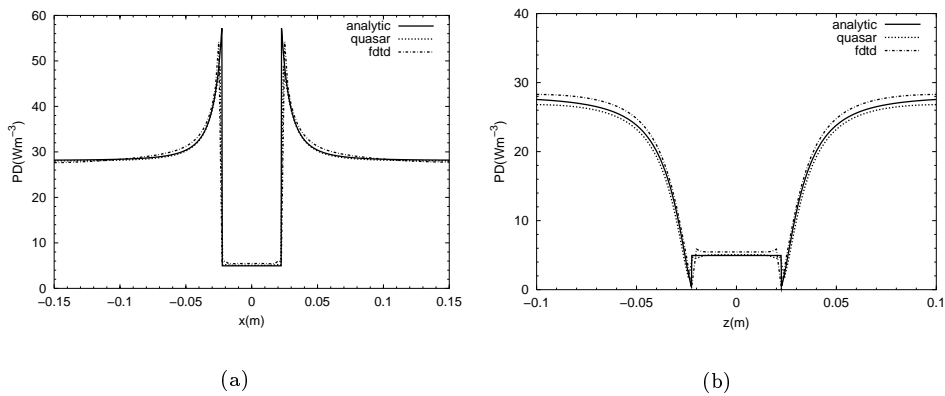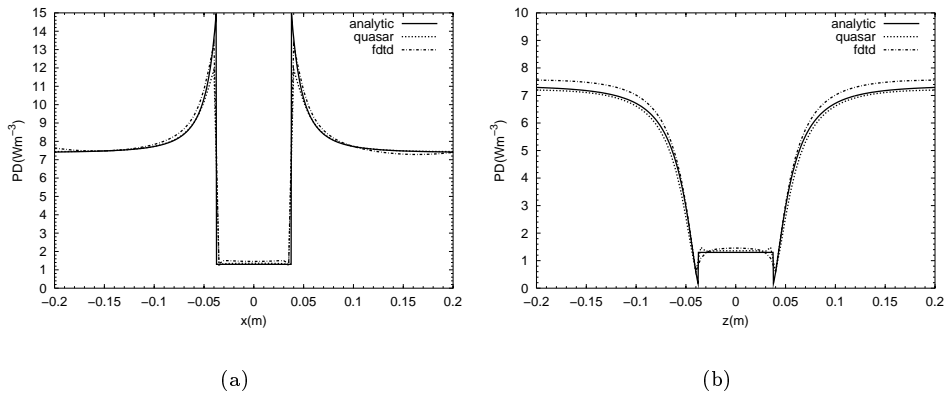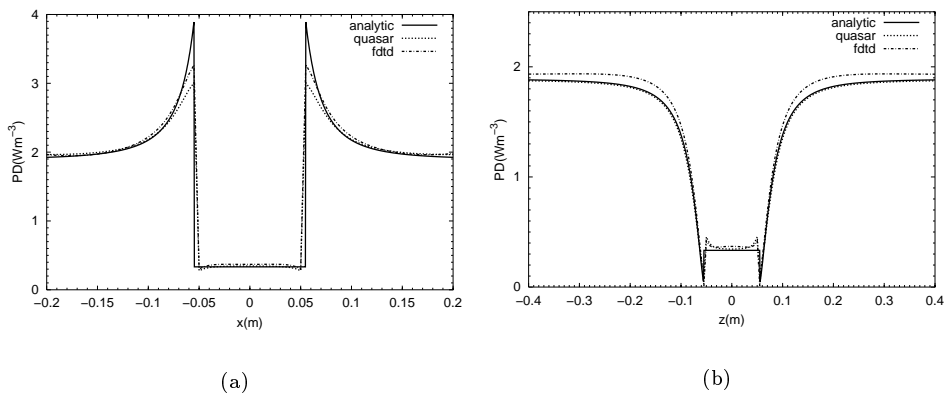**Figure 5.5:** Comparison of Quasar and FDTD simulation with a
resolution of 5 mm in phantom C at 13.56 MHz with an
analytical solution.

5.2.2 Results

The analytic solution and the QUASAR and FDTD simulations are compared along two tracks. The first along the $x-$axis, centrally through the phantom. The second track along the $z-$axis (i.e. from the bottom plate to the top plate), also centrally through the phantom.

Figure 5.2 shows the tracks in the smallest phantom at 13.56 MHz. An excellent agreement is observed, except at the muscle-fat boundary. This is mainly due to the discretization of the sphere on the rectangular grid. To test this assumption, the simulation was repeated with the same phantom at a resolution of 2 mm (QUASAR) and 2.5 mm (FDTD). In figure 5.3 it can be seen that the differences at the tissue boundaries are significantly reduced.

In order to investigate whether the quasi-static approximation is valid beyond the commonly used scale of $\lambda/10$, a much larger phantom was subjected to simulation and comparison. With a diameter and height of 40 cm the phantom has a size of about 0.22λ. The results in figure 5.4 show fair agreement of the FDTD simulation and the analytic solution. Even with a phantom with a height of 80 cm good agreement can be observed (figure 5.5), although some deviation between the FDTD simulation and the analytic solution is present along the $z-$track.

In table 5.2 the difference between the FDTD and QUASAR simulations and the analytical solution is quantified. The relative, averaged absolute difference between the FDTD simulations and the analytic solution grows with the increase of the phantom size. A reduction of the operating frequency to 8 MHz in phantom A (30×20 cm) resulted in a reduction of the difference between the FDTD simulation and the analytic solution. In both FDTD and QUASAR simulations the difference decreases with an increase of the resolution.

5.2.3 Discussion and conclusion

The FDTD simulation fully evaluates the Maxwell equations without making any assumptions. The simulation, however, needs a large computational volume to enclose the artificial circuit needed to provide a return path for the current generated by the sources. This limits the maximal resolution of the simulation. The analytic solution assumes a static field of infinite dimensions in $x-$ and $y-$direction. The correspondence of the analytic solution with the FDTD results shows that, with the applied phantom dimensions and a frequency of 13.56 MHz, the quasi-static approach is valid within reasonable error margins for phantoms with a size up to 40 cm and that the assumption of a homogeneous $\vec{E}$-field between the finite capacitor plates in a homogeneous phantom is correct. The average absolute difference with the analytic solution is 1.9%. The difference is even smaller at 8 MHz, because of the longer wavelength with respect to the object dimensions. Errors up to

Table 5.2: Phantom simulations: relative, averaged absolute difference Q between simulations and the analytical solution, $Q_{phantom}$ in the full phantom and $Q_{boundary}$ in a 2 cm shell around the muscle-fat boundary.

test	simulation	frequency MHz	resolution (mm)	$Q_{phantom}$ (%)	$Q_{boundary}$ (%)
A	FDTD	13.56	5	1.7	6.6
	FDTD	8.0	5	0.46	5.6
	Quasar	13.56	5	0.53	14.6
A	FDTD	13.56	2.5	1.5	5.4
	Quasar	13.56	2	0.24	6.5
B	FDTD	13.56	5	1.9	7.3
	Quasar	13.56	5	0.49	14.2
C	FDTD	13.56	5	2.1	7.3
	Quasar	13.56	5	0.73	15.5

6.6% occur the muscle-fat boundary, partly due to the rectangular discretization of curved surfaces.

QUASAR also matches the analytic solution with small overall error, so it is apparently a valid simulation tool for structures with a size up to 40 cm in a capacitive heating device with a frequency up to 13.56 MHz. There is a slight underestimation of the power density in muscle at the muscle-fat boundary (figure 5.4), amounting to an error of 14.6% in the boundary region. The errors at the boundary can be reduced by increasing the resolution from 5 mm to 2 mm.

This gives the possibility of treatment planning for RF capacitive heating devices with patient anatomies, using QUASAR simulations. The efficiency of the QUASAR algorithm allows for patient simulation at high resolution, up to 2 mm. A patient simulation at a resolution of 2 mm can be performed on a standard PC (800 MHz), running GNU/Linux® in about 10 hours, requiring 500 MB RAM.

5.3   Treatment planning with a patient anatomy

5.3.1   Methods

The patient model, figure 5.6 was derived from a 40 cm CT data set (slice thickness 5 mm) of a male, Asian patient with a prostate tumour. All slices in figure 5.6 are
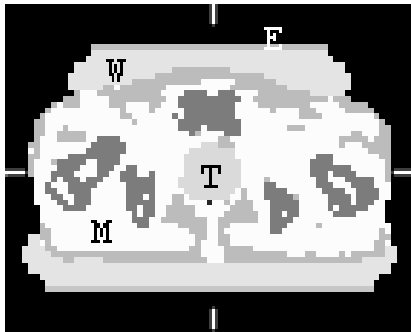
(a)

(b)
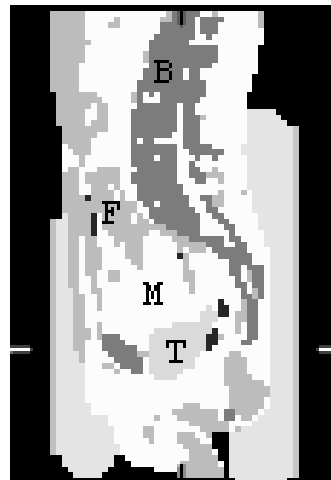
(c)

Figure 5.6: Segmented and down scaled patient placed between circular electrodes (E) with water filled bolus bags (W). The patient is segmented in muscle (M), fat (F), bone (B) and intestinal air (small black regions). (a) transversal, (b) coronal and (c) sagittal slice; markers indicate the centre of the tumour.

Table 5.3: Dielectric and materials properties of applicator materials and patient tissues. The thermal properties of 'agar' are omitted: this material is not used in the thermal simulations.

material/ tissue	rel. perm. ε_r	el. cond. σ $S\,m^{-1}$	density ρ $kg\,m^{-3}$	spec. heat Cp $J\,kg^{-1}\,K^{-1}$	therm. cond. k $W\,m^{-1}\,K^{-1}$	perfusion $ml\,100\,gr^{-1}\,min^{-1}$
saline water	76.5	0.5	1000	4180	6.0	0
air	1.0	0	1.3	1000	0.02	0
muscle	160	0.64	1050	3639	0.56	22
fat	29.6	0.053	888	2387	0.22	6.8
bone	36.8	0.043	1595	1420	0.65	0.77
tumour	160	0.64	1050	3639	0.56	11
agar	77.6	0.39	1000			

taken centrally through the tumour. The CT data set was segmented by Hounsfield Unit thresholding (Hornsleth *et al.*, 1996) and down-scaled to 5 mm cubic resolution, using the 'winner take all' algorithm (James and Sullivan, 1992). This method results in a patient model with regions that are assigned constant dielectric properties. The tumour was outlined by a physician. The material properties used in the simulations are listed in table 5.3, the dielectric properties of tissue have been derived from Gabriel *et al.* (1996), those of saline water (0.4% NaCl, 10ºC) and agar (with 0.18% NaCl, 37ºC) from Stogryn (1971). The thermal properties of tissue have been taken from the ESHO Taskgroup Committee (ESHO Taskgroup Committee, 1992).

The patient was treated in a Thermotron RF8 applicator with an anterior electrode of 21 cm and a posterior electrode of 30 cm. The definition of the applicator electrodes with bolus bags is done using the Generic Object Format (De Bree, 1998). The metal electrode plates are set at a constant voltage of 1 V, respectively -1 V, with a frequency of 8 MHz. The QUASAR computation of the power density distribution takes about 40 minutes with a standard PC (800 MHz) and requires about 7.5 MB RAM. From the power density distribution a Specific Absorption Rate (SAR) distribution is derived. The temperature distribution has been computed from the power density distribution using the DIVA thermal model (Kotte, 1998), without accounting for the effect of the discrete vasculature and systemic heating. The tissue blood perfusion was modeled by means of a heatsink (see table 5.3). The tumour perfusion was taken half the value of the surrounding muscle tissue (Wust *et al.*, 1996; Van Vulpen *et al.*, 2002b). The power density distribution was scaled to a total absorbed power in the patient volume of 700 W, in order to obtain a median tumour temperature of approximately 42ºC. The temperature of the bolus bags and the metal electrodes was kept at a constant value of 10ºC, the ambient air at 22ºC. The temperature at the cranial and caudal cut off planes was

kept constant at 37°C. The simulation time was set at 2000 s with a time step of 0.25 s; the temperature after 8000 time steps is within 0.1°C of stationarity. Calculation of the temperature distribution takes less then 15 minutes and requires about 7.5 MB RAM.

5.3.2 Results

The SAR distribution (figure 5.7) shows a distinct maximum below the lower part of the anterior electrode (figure 5.7(d)), where a large muscle volume is present. Logarithmic scaling of the gray values in figure 5.7 allows presentation of the large SAR differences between the superficial and the central regions. In figure 5.7(a) a SAR maximum can be observed in the anterior and posterior fat layers. This is consistent with the high ratio of SAR in fat with respect to muscle, when the local $\vec{E}$-field is normal to the tissue interface (Lagendijk and De Leeuw, 1986). With the used dielectric tissue parameters and a frequency of 8 MHz the theoretical ratio for a pure normal $\vec{E}$-field is $SAR_{fat}/SAR_{muscle} = 13.6$, explaining the high SAR values in the superficial fat layers despite the low conductivity of fat.

The low SAR values in the tumour volume appear to be caused by a shielding effect of the pelvic bone, in particular the os pubis (figure 5.7(d)): the low conductivity of bone causes a high current density in the narrow channels of muscle tissue between the bone oriented in the direction of the $\vec{E}$-field and a low current density in the areas shielded by bone. The inhomogeneous distribution of current density causes local SAR maxima and minima. In order to illustrate the effect of the bone structure on the SAR distribution, a SAR computation was made with the tumour, muscle, fat and bone tissue replaced by agar bound saline water. The SAR distribution figure 5.8(a) shows a transversal slice of the SAR distribution at the same location as used in figure 5.7(a). The SAR pattern is fairly homogeneous, with maxima at the edge of the smaller, anterior electrode. The central minimum is caused by a small air pocket. After restoring the bone structure the SAR distribution (figure 5.8(b)) is almost similar to the pattern seen in figure 5.7(a) with exception of the maxima in the anterior and posterior fat layers. Figure 5.9 shows anterior-posterior SAR profiles along a track through the patient anatomy and the agar volume with and without bone. The track is located between the anterior and posterior markers in the figures 5.6(a) and 5.6(c). All profiles have been computed with the same unit excitation voltage on the capacitor plates. Comparison of the SAR profiles in the agar volume and in the agar volume with bone clearly shows the SAR reduction in the anterior part of the tumour due to the shielding effect. The SAR profile with the original tissues shows the anterior peak in the fat layer, caused by normal $\vec{E}$-field, and an even larger SAR maximum in the posterior muscle channel. The SAR in tumour is significantly reduced with respect to the SAR profiles in the agar volume. This indicates that the central SAR distribution

(a)

(b)

(c)

(d)
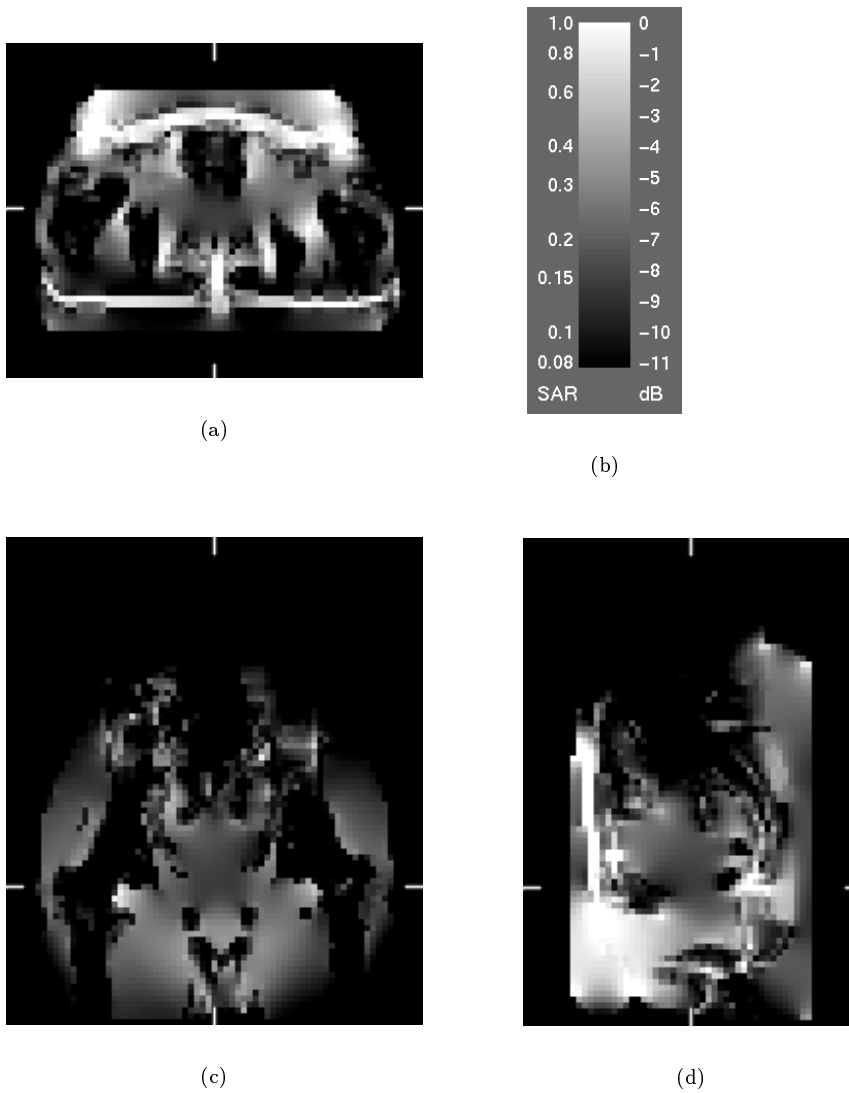
Figure 5.7: SAR distribution in the patient volume, (a) transversal , (c) coronal and (d) sagittal slice. SAR values are presented (b) on a logarithmic scale

(a)   (b)
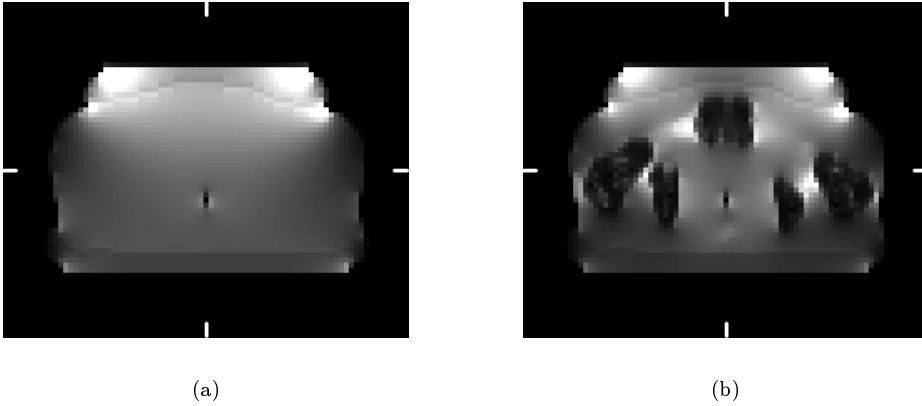
Figure 5.8: Transversal slice in the SAR distribution in the pa-
tient volume with (a) tumour, muscle, fat and bone replaced
by agar, (b) tumour, muscle and fat replaced by agar, and
bone in place.

is mainly determined by the bone and fat distribution, and that the superficial
SAR distribution is further influenced by the fat layers.

The temperature distribution, calculated from the SAR distribution in the hetero-
geneous patient model, given in figure 5.10 also shows maxima in the anterior and
posterior regions adjacent to the electrodes (figure 5.10(c)). However, the SAR
maximum in the thin (1 cm) posterior fat layer (figure 5.7(a)) did not cause a
temperature maximum at the same location (figure 5.10(a)). Apparently the cool-
ing effect of the bolus is sufficient to suppress this unwanted maximum. The bolus
cooling effect is, however, not able to reduce the anterior maximum, because the
thickness of the anterior fat layer exceeds 1 cm. As expected from the SAR dis-
tribution, only a modest temperature rise is obtained in the tumour volume with
respect to normal tissue. For a quantitative evaluation of the temperature distri-
bution a cumulative histogram is given in figure 5.11. The T_{90}(tumour) = 40.9°C,
T_{50}(tumour) = 41.8°C and T_{10}(tumour) = 43.4°C, indicating an inhomogeneous
temperature distribution in the tumour. The temperature indices in muscle, in-
dicating the maximum temperature are T_{10}(muscle) = 43.3°C and T_1(muscle) =
49.7°C. The total muscle volume is 11090 cm^3, so 1% of it exceeds the tumour vol-
ume (94.5 cm^3). The temperature indices for fat are even higher with T_{10}(fat) =
45.6°C and T_1(fat) = 59.4°C.

Practical attempts to reduce the excessive superficial heating include the use of
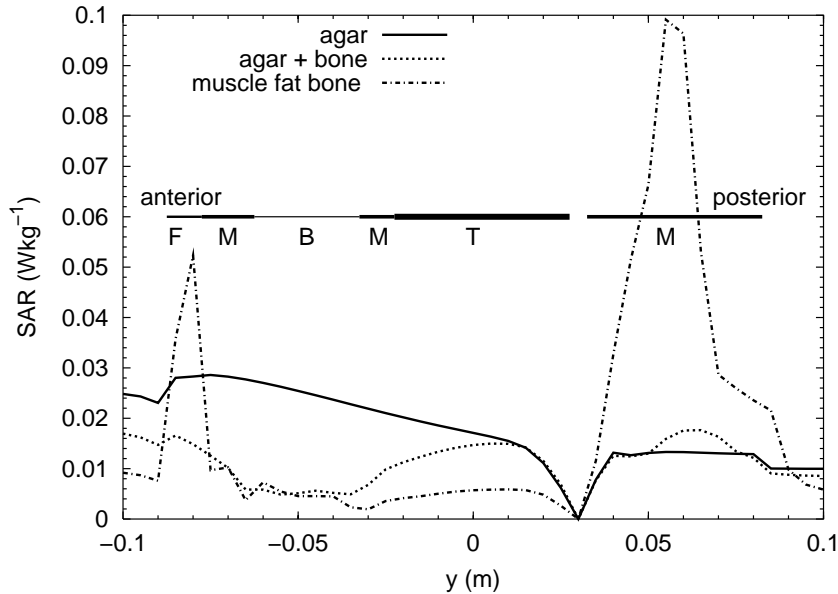
Figure 5.9: SAR profile, anterior-posterior centrally in the tumour location in the patient volume, with tumour(T), muscle(M), fat(F) and bone(B) tissue and with agar replacing tumour, muscle and fat, with and without bone.

overlay bolus bags, that are circulated with a liquid close to the freezing point of water (Tomimatsu *et al.*, 1999a,b). In order to make a crude simulation of the effect of an overlay bolus with very low temperature, the temperature calculation was repeated with the (fixed) temperature of the bolus bags set at 0°C and the ambient air replaced with water, also at a fixed temperature of 0°C. The temperature profiles in figure 5.12 show the influence of the extreme cooling of the superficial tissue in comparison to normal cooling. The temperatures are plotted along an anterior-posterior profile, located between the anterior and posterior markers in the figures 5.10(a) and 5.10(c). It can be seen that the profiles practically overlap, except in the first 2 cm anterior to the pubic bone. Both the anterior and posterior peaks are not affected by the extra cooling efforts. The temperature distribution in the tumour is not significantly changed: T_{90}(tumour) = 40.9°C, T_{50}(tumour) = 41.8°C and T_{10}(tumour) = 43.4°C. However, the temperature indices in muscle and fat are reduced to some extend: T_{10}(muscle) = 42.8°C and T_1(muscle) = 48.5°C; T_{10}(fat) = 44.2°C and T_1(fat) = 55.3°C.

(a)
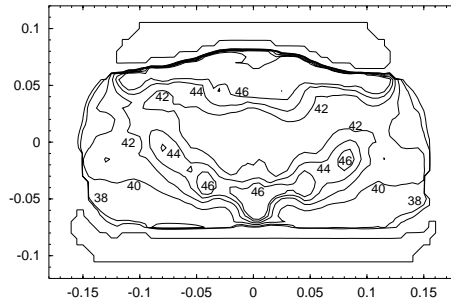
(b)

(c)
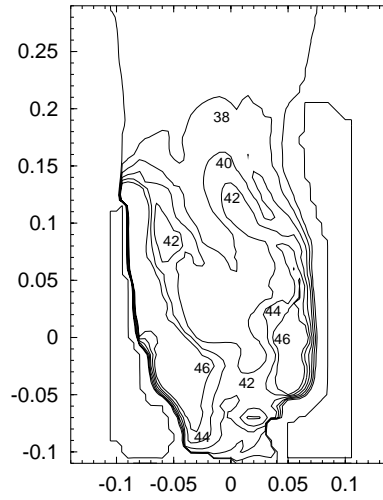
(d)

Figure 5.10: Temperature distribution in the patient volume (a,c) in gray-scale and (b,d) contour plots, (a,b) transversal and (c,d) sagittal slices. The slices are taken in the same planes as in figure 5.6.
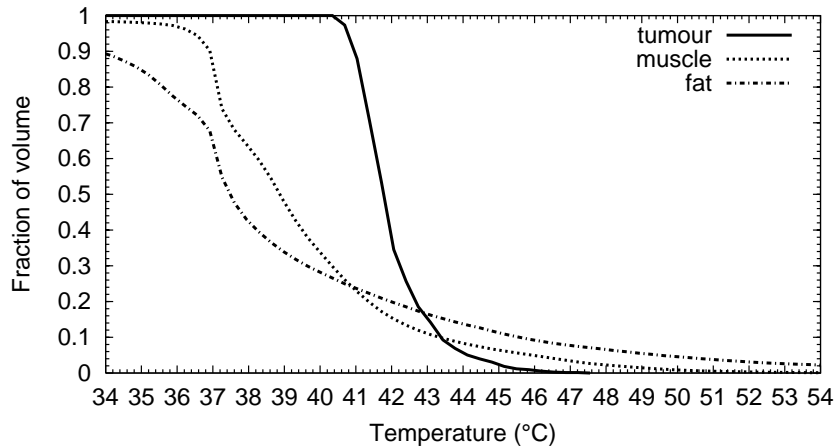
Figure 5.11: Cumulative histogram of the temperature distribution in the patient.

5.4   Discussion and conclusion

Comparison of SAR distributions in a phantom computed using the FDTD method at 13.56 MHz with the analytic solution of a static $\vec{E}$-field showed that a quasi-static approximation is valid with the used phantom and electrode dimensions and the used frequency. The SAR distribution in a patient anatomy can be computed, using a quasi-static model, in about 40 minutes at a resolution of 5 mm.

In a patient anatomy with a pelvic tumour, the SAR maxima are located in the superficial fat and muscle layers. The central SAR distribution is mainly influenced by the configuration of the pelvic bone. The bone and fat structure, in particular the os pubis shields the tumour location, causing a local SAR minimum.

In general, the SAR distribution is determined primarily by the anatomy of the patient. The relative thickness of the used patient model, defined as the height of the patient between the electrodes devided by the width of the patient model (Tanaka *et al.*, 1981) is 0.57. In a cylindrical agar phantom with the same relative thickness the ratio of the central SAR with respect to the SAR at 1 cm depth is only slightly less than 1.0 (Tanaka *et al.*, 1981; Kato *et al.*, 1985). In the patient model fully consisting of agar a SAR ratio of 0.61 is found, however, in the patient model
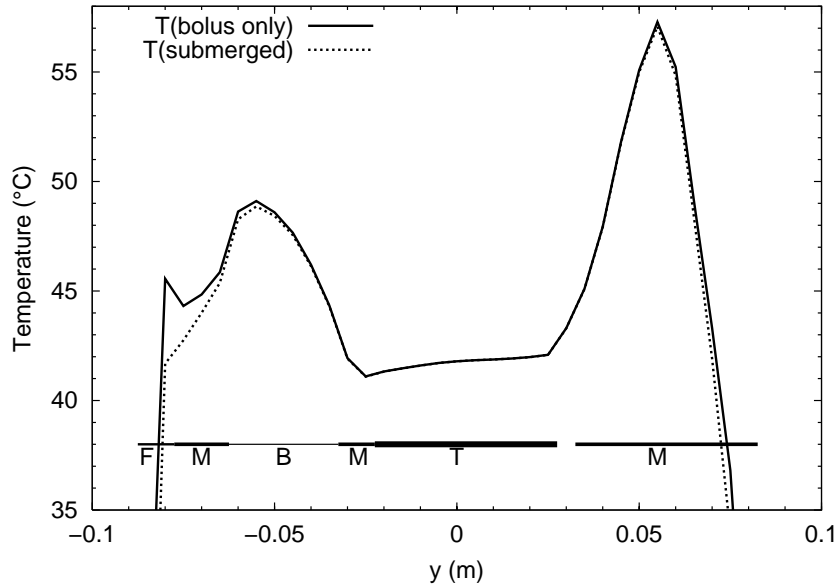
Figure 5.12: Anterior-posterior temperature profile, centrally in
the tumour, with normal bolus bags and with the patient
submerged in ice water. The tissues along the profile are
coded as Muscle, Fat, Bone and Tumour.

with muscle, fat and bone tissue the SAR ratio is only 0.12. It can be concluded
that evaluation of a capacitive hyperthermia device with a homogeneous agar
phantom, whether cylindrical or patient shaped, leads to overly optimistic results.
It has been shown (Kato *et al.*, 1997) that SAR maxima at the bolus edges can be
minimized with a simultaneous improvement of the ratio of the central SAR with
respect to the SAR at 1 cm depth by the use of overlay bolus bags with a reduced
salinity in a homogeneous muscle-fat phantom. The proposed treatment planning
system for capacitive regional hyperthermia can be used to evaluate the effect of
overlay bolus bags on the SAR distribution in heterogeneous patient anatomies.

An adequate tumour temperature elevation can be obtained, however, not without
causing very high temperatures in the superficial fat and muscle layers. The cooling
effect of the bolus bags is only very superficial. The use of very cold overlay bolus
bags has only a marginal influence on the temperature distribution at a depth of
more than a few centimeters.

In a clinical study (Lee *et al.*, 1995) with (amongst others) 27 patients with a
pelvic tumour, an averaged maximum tumour temperature of only 40.5°C was

obtained, while a tumour temperature of 42.0°C or higher was the objective. Both the averaged maximum and the averaged mean tumour temperatures in the pelvic tumours were the lowest observed in the study. Of all patients in the study 60% complained of pain, and in 19% this pain was power limiting despite the use of pre-cooling of the superficial fat layers (Rhee *et al.*, 1991) and overlay bolus sheets. Comparable results (Van Rhoon *et al.*, 1992) have been found in a clinical evaluation of the HTM3000P capacitive hyperthermia system on a Dutch patient population.

Both the clinical studies and the simulation results indicate that pelvic tumours are not very suitable for treatment with capacitively coupled hyperthermia, because of the treatment limiting hot spots in normal tissue. However, it has to be noted that the reliability of thermal simulation depends largely on the presumed values of the perfusion. These values were assumed independent of temperature in this study. Thermal models that incorporate the effect of a temperature dependent blood perfusion (Lang *et al.*, 1999) indicate a lower total generator power in a radiative system to achieve tumour goal temperature and a lower temperature of the superficial layers. Moreover, the effect of the systemic heating of the patient is not taken into account. The temperature extremes found in this study may be overestimations.

Considering these limitations, the SAR and temperature models for capacitive hyperthermia can be used for individual patient treatment planning, for instance electrode diameter and position selection. Furthermore the models can be used in evaluation of improvements of capacitive hyperthermia devices and comparison with other hyperthermia systems.

Chapter 6

Comparison of a Capacitive and a Cavity Slot Radiative applicator for Regional Hyperthermia

Abstract The performance of a capacitive and a radiative annular phased array applicator for regional hyperthermia is compared in a model study, for an agar-bone phantom and a structured patient anatomy with a prostate tumour. The capacitive applicator is a model of the Thermotron RF8 device, operating at 8 MHz. Its performance is improved by the use of very cold overlay boli with a suitable salinity. The radiative applicator is a three ring, cavity slot annular array applicator, operating at 150 MHz. The Specific Absorption Rate (SAR) distribution in the cavity slot applicator is optimized by phase-amplitude control. Comparison of both SAR and thermal distributions shows that the radiative applicator can generate good tumour heating in the pelvic region and avoid the overheating of superficial fat layers and muscle tissue seen in the capacitive applicator.

領域加温における誘電型加温法と放射型加温法との比較

Hugo Kroeze[1]、小久保雅樹[2]、Jeroen B. Van de Kamer[1]、Astrid A. C. De Leeuw[1]、菊地眞[3]、平岡眞寛[4]、Jan J. W. Lagendijk[1]

[1]ユトレヒト大学メディカルセンター放射線腫瘍学
[2]先端医療センター映像医療研究部
[3]防衛医科大学校医用電子工学
[4]京都大学医学研究科腫瘍放射線科学

[1]PO Box 85500, 3508, GA, Utrecht, The Netherlands
[2]神戸市中央区湊島南町２－２
[3]所沢市並木３－２
[4]京都市左京区聖護院川原町５４

抄録

領域加温における誘電型加温法と放射型加温法を、ファントムモデルと前立腺患者をモデルとして用いて比較した。誘電型加温のモデルには、8MHz 装置（サーモトロン RF8）を用いた。この加温性能は適切な塩分濃度で極低温にしたオーバーレイボーラスを使用することで改善した。放射型加温には 3 列のリングアレイ型アンテナを用い、150MHz の電流を給電した。放射型においては、位相、振幅を制御することにより、単位質量あたりのエネルギー吸収率（SAR）を最適化した。SAR と温度分布を比較したところ、放射型加温では骨盤内腫瘍に関して良好な温度分布が得られ、誘電型加温で見られたような皮下脂肪、筋組織でのホットスポットを防ぐことができた。

6.1   Introduction

The Thermotron RF8 system (Yamamoto VINITA Co., Osaka, Japan) is widely in use in Asian countries for the hyperthermia treatment of tumours. The RF8 system is a capacitive heating device operating at 8 MHz, where the patient is placed between two electrodes which are connected to a high power RF generator (Tanaka *et al.*, 1981; Kato *et al.*, 1985). The patient is coupled to the electrodes with bolus bags, containing saline water of low temperature. The positive effect of capacitive regional hyperthermia was demonstrated in a randomized study of radiation therapy versus thermoradiotherapy in stage IIIB cervical carcinoma (Harima *et al.*, 2000). The basic characteristics of capacitive hyperthermia are related to the E-field orientation perpendicular to the body surface and the low RF frequency. These properties result in absorbed power distributions highly governed by tissue anatomy (see Chapter 5). Characteristics are overheating of subcutaneous fat, edge effects and insufficient penetration depth (Hiraoka *et al.*, 1987). These effects can be partially overcome by intensive surface cooling to avoid overheating of fat (Rhee *et al.*, 1991), the use of water pads (i.e. overlay bolus sheets) larger than the electrodes to reduce edge effects (Kato *et al.*, 1997; Tomimatsu *et al.*, 1999a,b), and/or increasing the size of the electrodes to improve penetration depth (Tanaka *et al.*, 1981; Kato *et al.*, 1985).

Clinical studies show a good performance of capacitive heating techniques in the head and neck region and the thorax, fair results in the upper abdomen and moderate results in the lower abdomen and pelvis (Hiraoka *et al.*, 1987; Lee *et al.*, 1995).

Parallel to the advent of capacitive applicator systems, several radiative annular array systems have been developed: the early BSD Annular Array (AA) system (Turner, 1984), the BSD-2000 SIGMA 60 applicator (Turner and Schaeffermeyer, 1989), the Amsterdam 4 Waveguide system (Van Dijk *et al.*, 1989) and the Utrecht Coaxial TEM system (De Leeuw and Lagendijk, 1987), operating in the range from 70 MHz to 110 MHz. These systems are characterized by an $\vec{E}$-field oriented parallel to the cranial-caudal axis of the patient. A randomized trial by Van der Zee *et al.* (2000) established the positive effect of regional hyperthermia with radiative applicators, combined with external radiotherapy on pelvic tumours. These early radiative systems are characterized by a deep interference maximum of the absorbed power distribution, but also by treatment limiting local hot spots (Dinges *et al.*, 1998; Van Vulpen *et al.*, 2002a), systemic stress (Van Es *et al.*, 1995) and general discomfort (Rau *et al.*, 1998).

Egawa *et al.* (1988) compared the performance of the Thermotron RF-8 system with the Annular Array (AA) system (Turner, 1984) in a study with 13 patients with abdominal and pelvic tumours. The study concluded that both systems have advantages and disadvantages, and did not indicate either of the applicators as su-

perior. To resolve these disadvantages, both capacitive and radiative hyperthermia systems became subject of further development and technical improvement.

Recently, hyperthermia treatment planning (HTP) systems have been developed for radiative applicator systems (Sullivan, 1991; Clegg *et al.*, 1996; Wust *et al.*, 1996; Paulsen *et al.*, 1999; Van de Kamer *et al.*, 2001a, 2002a). It has been shown using these HTP's that a new generation of radiative systems can be developed using multiple antenna rings, phase amplitude control and a higher RF frequency (Wust *et al.* (1996); Paulsen *et al.* (1999); Seebass *et al.* (2001) and Chapter 3). The characteristics of a new radiative cavity slot antenna have been described in Chapter 3. Using a quasi static model, a HTP system for capacitive regional hyperthermia has been developed (see Chapter 5).

Using both HTP systems, the current paper compares the performance of the RF8 capacitive system with the new design of the cavity slot radiative hyperthermia applicator, using a Japanese patient anatomy with a prostate tumour. The basic performance of both applicator types is investigated in a patient shaped agar-bone phantom, showing the influence of the bone structure on the SAR distribution in the capacitive applicator.

6.2   Methods

6.2.1   Patient model and agar bone phantom

The patient model, figure 6.1, has been derived from a 40 cm CT data set (slice thickness 5 mm) of a male, Asian patient with a prostate tumour. All slices in figure 6.1 are displayed centrally through the tumour. The CT data set was segmented by Hounsfield Unit thresholding (Hornsleth *et al.*, 1996) and down-scaled to 5mm^3 resolution, using the 'winner take all' algorithm (James and Sullivan, 1992). This method results in a patient model with regions that are assigned homogeneous dielectric properties. The tumour was manually outlined by a physician.

The SAR distribution in a patient in a capacitive heating device depends largely on the distribution of fat and bone (see Chapter 5). To separate the effects of bone and fat in the comparison of a capacitive and a radiative applicator, the comparison is first made in the patient shaped agar-bone phantom. The agar-bone phantom is created by assigning fat, muscle and tumour tissue the dielectric properties equivalent to saline water with 0.22% NaCl at 25°C (Stogryn, 1971). These values are equal to those used by Tomimatsu *et al.* (1999a,b) in a phantom study.

The dielectric properties used in the SAR computations are listed in table 6.1. The values for tissue have been derived from literature (ESHO Taskgroup Committee,

1992; Gabriel *et al.*, 1996; Van de Kamer *et al.*, 2001e), those of the saline water in the bolus bags from Kato *et al.* (1997).

Table 6.1: Dielectric properties of applicator materials and patient tissues at 8 MHz and 150 MHz

| frequency | 8 MHz | | 150 MHz | |
material/tissue	ε_r	$\sigma(\mathrm{S\,m^{-1}})$	ε_r	$\sigma(\mathrm{S\,m^{-1}})$
bolus water	73.5	3.0	-	-
overlay bol.	78.6	0.45	-	-
tap water	-	-	76.5	0.042
deionised water	-	-	76.5	0.001
air	1.0	0	1.0	0
muscle	160	0.64	75.0	0.75
fat	29.6	0.053	10.0	0.06
bone	36.8	0.043	10.0	0.05
tumour	160	0.64	65.0	0.74
agar	77.6	0.39	77.6	0.39

6.2.2 RF8 SAR model

The SAR distributions in the patient model have been computed using the quasi-static treatment planning system for capacitive hyperthermia (see Chapter 5). The validity of the quasi-static approximation for capacitive HTP has been validated by comparison with an analytic solution. The patient was treated in a Thermotron RF8 applicator with an anterior electrode of 21 cm and a posterior electrode of 30 cm. In order to optimize the heating conditions in the RF8 applicator, overlay boli (Kato *et al.*, 1997; Tomimatsu *et al.*, 1999a,b) were incorporated in the patient simulation. The model of the overlay boli was created by growing an anterior and posterior 'blanket' with a thickness of 25 mm on the patient model, and positioning the the normal electrode bolus bags against them (figures 6.1(a) and 6.1(c)). The salinity of the electrode bolus bags and overlay boli were taken from a phantom study by Kato *et al.* (1997), as the values that result in the best ratio of central SAR with respect to SAR in the superficial fat. As the main function of the overlay boli is the suppression of high SAR values in the superficial fat, they have not been employed in the simulation with the agar-bone phantom.

The definition of the applicator electrodes with bolus bags is done using the Generic Object Format (De Bree, 1998). The metal electrode plates are set at a fixed potential of 1 V, respectively -1 V, with a frequency of 8 MHz. The QUASAR computation of the power density distribution takes about 40 minutes with a standard PC (800 MHz) and requires about 7.5 MB RAM. From the power density distribution a Specific Absorption Rate (SAR) distribution is derived.

(a)

(b)

(c)

(d)
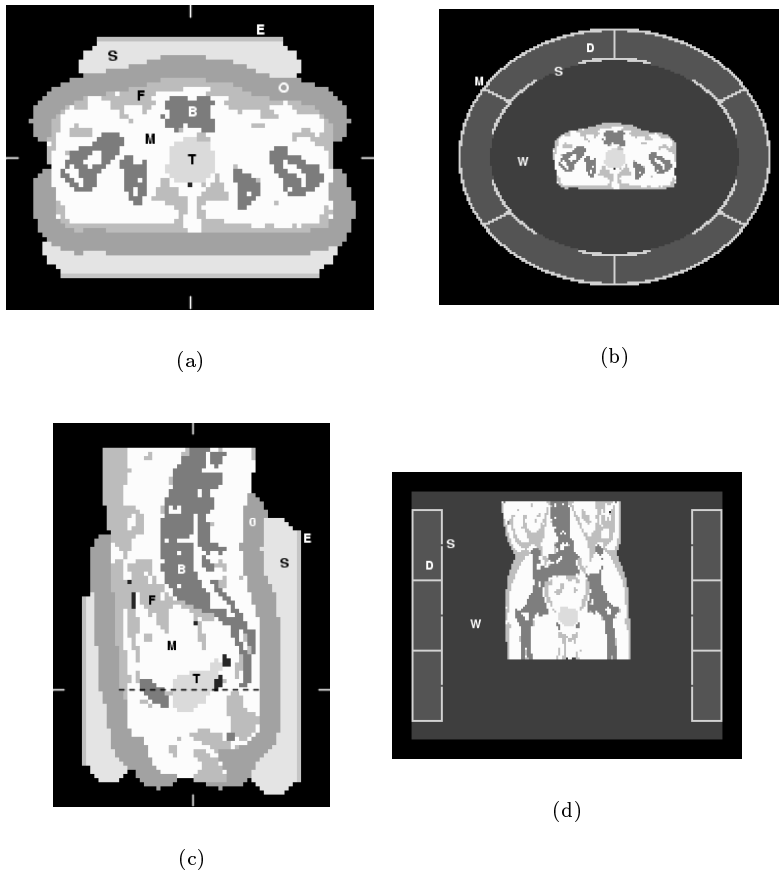
Figure 6.1: Patient model (a,c) in RF8 applicator and (b,d) in cavity slot applicator. The CT data set is segmented in muscle (M), fat (F), bone (B) and tumour (T) tissue, (a,b) transversal, (c) sagittal and (d) coronal slice centrally through the tumour. The RF8 applicator is modeled with circular electrodes (E) coupled to the patient with saline bolus bags (S) and overlay boli (O). The cavity slot applicator (b,d) is constructed from metal sheets (M), forming cavities filled with deionised water (D) with radiating slots (S). The space between the applicator and the patient is filled with tapwater (W).

6.2.3 Cavity slot applicator SAR model

The cavity slot applicator consists of three elliptical rings of six cavity slot antennas each (see Chapter 3). The patient and the antenna array are submerged in a volume of tapwater, in order to couple the patient to the antennas. The operating frequency of the cavity slot applicator is chosen to be 150 MHz; this frequency was found to be optimal for the effective heating of deep situated tumours and good hot spot avoiding ability in normal tissue (Seebass *et al.* (2001) and Chapter 3). The cavities are filled with deionised water in order to reduce the dimensions of the antenna array. The length of the slots and the depth of the cavities are approximately $\lambda_{water}/2$ and $\lambda_{water}/4$ respectively, in order to obtain a resonant antenna at the operating frequency. The Finite Difference Time Domain (FDTD)-core of our Regional Hyperthermia Treatment Planning (HTP) system (Van de Kamer *et al.*, 2001a) was used to compute $\vec{E}$-field distributions in the patient model. The number of iterations was 12000; convergence was tested by observing the time evolution of $|\vec{E}|$ at a test point in the patient and found to be stable within 0.1% of the end value. The $\vec{E}$-field distribution is computed for each separate slot antenna. The active slot is excited with a source, generating a triple cosine pulse of unit amplitude, placed in the gap in the metal sheet halfway along the length of the slot. The source has an impedance of 50 Ω, implemented as described by Piket-May *et al.* (1994). The inactive slots are terminated with the same impedance in order to achieve correct simulation of coupling effects between the antennas.

A typical $\vec{E}$-field computation requires about 200 MB RAM and takes about six hour on a 800 MHz standard personal computer. The SAR distribution for N $\vec{E}$-fields is computed according to equation (6.1) using a steering vector $\mathbf{V}$, where $\mathbf{V}_i$ is the complex number representing the amplitude and phase of each antenna (Sullivan *et al.*, 1993).

$$\text{SAR}(\vec{r}) = \frac{\sigma(\vec{r})}{2\,\rho(\vec{r})} \left| \sum_i^N \vec{E}(\vec{r})_i \, \mathbf{V}_i \right|^2 \tag{6.1}$$

In equation (6.1) $\text{SAR}(\vec{r})$ is the SAR, $\vec{E}(\vec{r})_i$ is the $\vec{E}$-field for antenna i, $\sigma(\vec{r})$ and $\rho(\vec{r})$ are respectively the conductivity and density of the voxel at $\vec{r}$.

6.2.4 SAR optimization

The SAR distribution in the RF8 applicator is optimized with the application of overlay boli and selection of the optimal salinity of both bolus elements (see section 6.2.2).

The SAR distribution in the cavity slot applicator is optimized by maximizing the objective function defined as the ratio of total SAR in the tumour versus total SAR in muscle and fat (or in agar in the agar-bone phantom). An optimizer routine modifies the steering vector **V** in small steps from a start vector in the direction of maximal improvement of the SAR ratio (see section 3.2.7). The optimizer constrains the power per antenna to 10% of the total power in order to avoid an unrealistic power distribution at the antennas. In order to avoid high SAR values in certain subvolumes, these subvolumes can be assigned a weight factor to reduce the local SAR value. In this study a three step optimization technique was employed. In the first step the SAR distribution was optimized for the best ratio of total SAR in the tumour versus total SAR in muscle and fat. In this SAR distribution the volume of the maximal 4th percentile in muscle is determined. This volume is assigned a weight of 10 in the next optimization step. The effect of this step is a reduction of the SAR maxima in muscle. The 4th percentile is selected because it generates a volume large enough to have effect in the second optimizing step. In the third step the largest two of the remaining unwanted SAR maxima are manually outlined and assigned an extra weight in the range of 50 to 125, depending on the size of the volume.

Table 6.2: Density and thermal properties of materials and patient tissues. The thermal properties of 'agar' are omitted: this material is not used in the thermal simulations. The entry for 'bolus water' refers to the boli attached to the electrodes, as well as the overlay boli.

material/ tissue	density $\rho(\mathrm{kg\,m^{-3}})$	spec. heat $\mathrm{Cp(J\,kg^{-1}\,K^{-1})}$	therm. cond. $\mathrm{k(W\,m^{-1}\,K^{-1})}$	perfusion $\mathrm{ml\,100\,gr^{-1}\,min^{-1}}$
bolus water	1000	4180	6.0	0
water	1000	4180	0.60	0
air	1.3	1000	0.02	0
muscle	1050	3639	0.56	22
fat	888	2387	0.22	6.8
bone	1595	1420	0.65	0.77
tumour	1050	3639	0.56	11
agar	1000	-	-	-

SAR distributions can be quantitatively compared using three performance indicators, the tumour index (Ti), muscle maximum index (MMi) and the fat maximum index (FMi) (see Chapter 3), defined as:

$$\text{Ti} \quad = \quad \frac{\text{SAR}_{50}(\text{tumour})}{\text{SAR}_{50}(\text{totalpatient})} \tag{6.2}$$

$$\text{MMi} \quad = \quad \frac{\text{SAR}_1(\text{muscle})}{\text{SAR}_{50}(\text{tumour})} \tag{6.3}$$

$$\text{FMi} \quad = \quad \frac{\text{SAR}_1(\text{fat})}{\text{SAR}_{50}(\text{tumour})} \tag{6.4}$$

where $\text{SAR}_{50}(Q)$ is the median SAR in the sub volume Q and $\text{SAR}_1(Q)$ is the value indicating the highest percentile of the SAR distribution in the indicated tissue type. The Tumour index Ti indicates the ability of the applicator to selectively direct energy into the tumour. The Muscle Maximum index MMi gives the level of the highest percentile of the SAR distribution in muscle with respect to the median value in tumour, i.e. it indicates the level of the maxima in muscle. The Fat Maximum index FMi is an equivalent ratio for fat. A good applicator should be able to generate a high Ti and low MMi and FMi.

6.2.5 Thermal model

The temperature distributions have been computed from the power density distributions using the DIVA thermal model (Kotte *et al.*, 1996), without accounting for the effect of the discrete vasculature. The tissue blood perfusion was modeled by means of a heatsink (Pennes, 1948). The tumour perfusion was taken half the value of the surrounding muscle tissue (Wust *et al.*, 1996; Van Vulpen *et al.*, 2002b). The thermal properties of tissue (table 6.2) have been taken from ESHO Taskgroup Committee (1992).

In the thermal simulations the power density distribution is scaled to a total absorbed power in the patient volume sufficient to obtain a median tumour temperature of approximately 42°C. In the RF8 simulation the temperature of the bolus bags, the metal electrodes and the overlay boli was kept at a constant value of 0°C (Tomimatsu *et al.*, 1999a,b), ambient air at 22°C. In the cavity slot simulation the temperature of the tap water bolus is set at a constant value of 34°C. The temperature at the cranial and caudal cut off planes was kept constant at 37°C in both applicator types.

The simulation time was set at 2000 s with a time step of 0.25 s; the temperature after 8000 time steps is within 0.1°C of stationarity. Calculation of the temperature distribution takes less then 15 minutes on a 800 MHz standard personal computer and requires about 7.5 MB RAM.

6.3   Results

6.3.1   Agar bone phantom

Figures 6.2(a) and 6.2(c) show the SAR distribution in the agar-bone phantom generated by a capacitive heating device operating at 8 MHz, the SAR distribution after three step optimization in the cavity slot applicator operating at 150 MHz is shown in figures 6.2(b) and 6.2(d). Both sagittal and transversal slices are taken in the same planes, the slices are taken centrally through the tumour, indicated by the markers in figure 6.2. The SAR distributions are normalized at a total absorbed power of 700 W in the phantom volume.

The capacitive SAR distribution is characterized by maxima at the edge of the anterior bolus bag and in the constrictions between the bone elements in the pelvic region (figure 6.2(a)). The SAR in the tumor location is relatively low, due to a shielding effect of the pelvic bone. The radiative SAR distribution shows a distinct maximum in the tumor location and minor submaxima anterior to the symphysis os pubica and in the lumbo sacral region. These submaxima were partly suppressed in the three step optimization process. Comparison of the SAR distribution along an anterior-posterior track (dashed line in figure 6.1(c)) centrally through the tumour (figure 6.3) shows that the SAR in the tumour is exceeded by anterior and posterior peaks in the RF8 applicator. The SAR track in the cavity slot applicator, on the other hand, shows a threefold increase in SAR in the tumour for the same total absorbed power in the patient and an ample reduction of the anterior and posterior peaks with respect to the tumour. This is also expressed in the performance indices (table 6.3).

Table 6.3: SAR performance indices in agar-bone phantom, comparison of RF8 and cavity slot (CS) applicator

tissue	index	RF8	CS
tumour	Ti	2.5	5.6
agar	AMi	2.7	0.87

6.3.2   SAR in patient model

Figures 6.4(a) and 6.4(c) show the SAR distribution in the patient model generated by the RF8 applicator. The SAR distribution after three step optimization in the cavity slot applicator is shown in figures 6.4(b) and 6.4(d). Both sagittal and transversal slices are taken centrally in the tumour. To allow comparison, both SAR distributions are normalized at an equal total absorbed power in the patient volume (700 W).

Comparison of figures 6.2(a) and 6.4(a) shows the influence of the subcutaneous fat layer on the capacitive SAR distribution. Due to the perpendicular orientation of

<div align="center">(a)</div>

<div align="center">(b)</div>

<div align="center">(c)</div>

<div align="center">(d)</div>
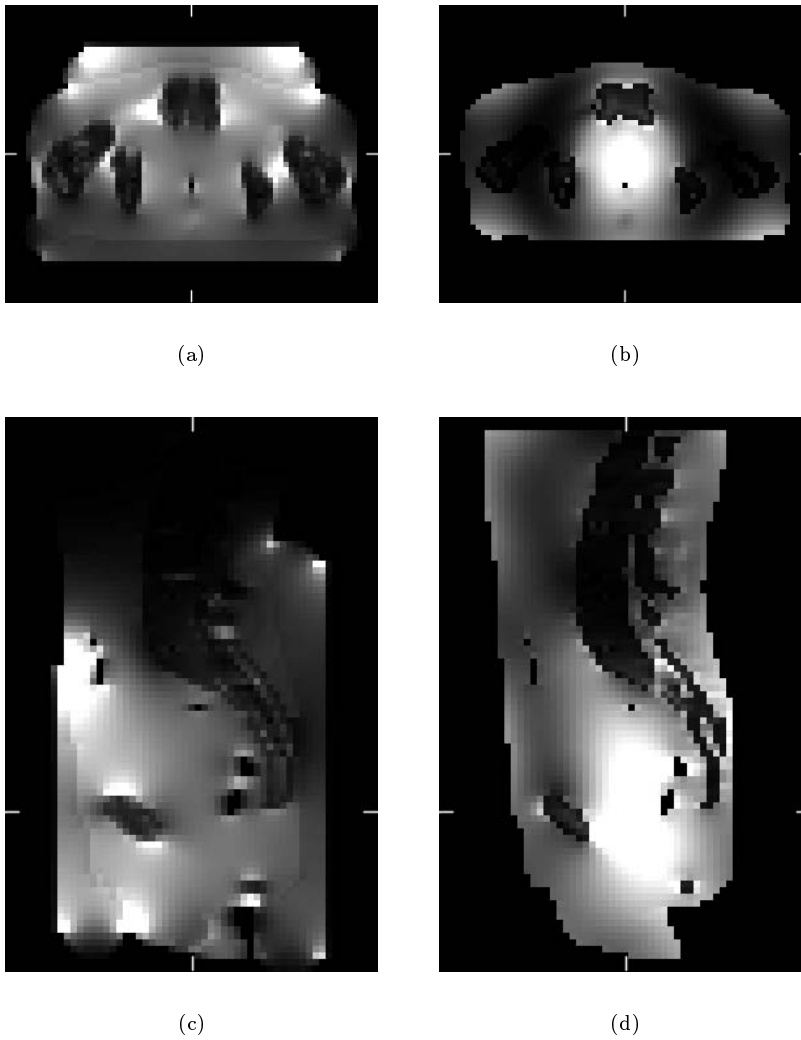
Figure 6.2: SAR distribution in the patient shaped agar-bone phantom, generated in (a), (c) the RF8 applicator and (b), (d) in the CS applicator. (a), (b) transversal and (c), (d) sagittal slice. The slices are taken centrally through the tumour location. Black and white indicate SAR values from 0 to $125\,\mathrm{Wkg}^{-1}$
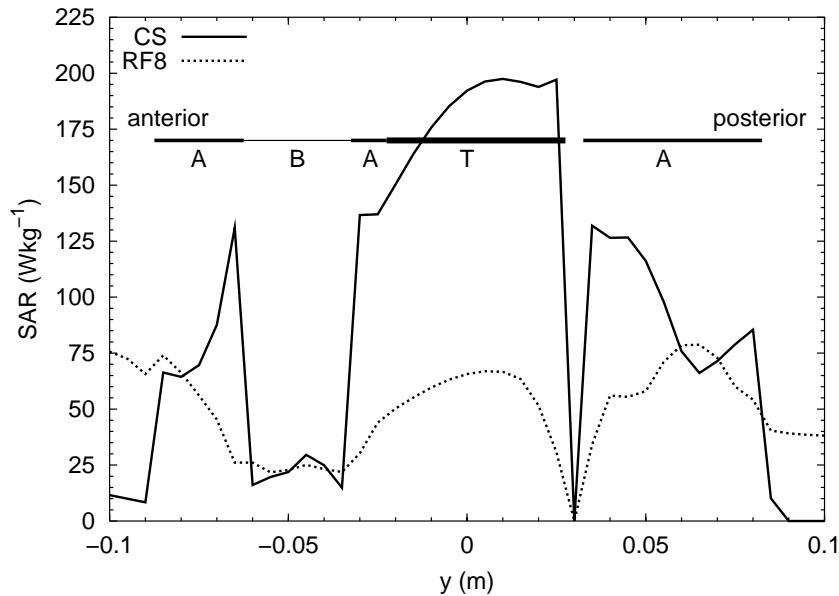
Figure 6.3: SAR profiles, anterior-posterior centrally in the tumour location in the patient shaped agar-bone phantom. Both SAR distributions normalized at 700 W total absorbed power.

the $\vec{E}$-field on the fat-muscle boundary the SAR in fat is very high with respect to the adjacent muscle (Lagendijk and De Leeuw, 1986). A distinct SAR maximum occurs below the lower part of the anterior electrode (figure 6.4(a)) due to the redistribution of current to the location where muscle is in direct contact with the bolus bag.

The radiative SAR distribution in the patient model is characterized by a very low absorption in fat (figure 6.4(b). Some SAR maxima occur in the lumbo-sacral region, the perineum and round the omphalos (navel) (figure 6.4(d)). These unwanted maxima could not fully be eliminated by increasing the weight of these subvolumina in the objective function without creating new SAR maxima. However, the main SAR maximum is located in the tumour volume.

For a quantitative comparison of the SAR distribution in both applicators, the performance indices are tabulated in table 6.4. The improved SAR concentration in the tumour is expressed by a twofold increase of the tumour index (Ti) in the cavity slot applicator with respect to the RF8 applicator. The reduction of both

muscle and fat maximum indices indicate the improvement of the SAR distribution outside the tumour volume.

Figure 6.5 shows SAR profiles along the anterior-posterior track (dashed line in figure 6.1(c)). The anterior SAR peak in the RF8 applicator is located in the fat layer, the posterior SAR peak is located in a narrow muscle conduit wedged between two fat volumes. The SAR track in the cavity slot applicator is more smooth, with an almost constant SAR value in the tumour and moderate peaks in the anterior and posterior muscle volume.

6.3.3 Temperature

The total power in the patient volume has been scaled to a value sufficient to reach a median tumour temperature of 42°C. The required total absorbed power in the patient in the RF8 applicator is 800 W, in the cavity slot applicator 270 W. Figure 6.6 shows the simulated temperature distributions for both applicators. Figures 6.6(a) and 6.6(c) show maxima in the anterior and posterior regions adjacent to the electrodes (figure 6.6(c)) of the RF8 applicator. However, the SAR maximum in the thin (1 cm) posterior fat layer did not cause a temperature maximum at the same location (figure 6.6(a)). Apparently the cooling effect of the posterior overlay bolus is sufficient to suppress this unwanted maximum. The bolus cooling effect is, however, not able to completely reduce the anterior maximum, there remain regions with a temperature exceeding 46°C. The thickness of the anterior fat layer locally exceeds 1.5 cm, which is considered the limit for effective skin cooling (Kato *et al.*, 1985; Nomoto *et al.*, 1999) The cavity slot applicator (figures 6.6(b) and 6.6(d)) generates a temperature maximum in the tumour volume and minor submaxima in the lumbo-sacral region and round the omphalos. There is no excessive heating of fat layers.

For quantitative comparison of the temperature distributions a cumulative histogram is given in figure 6.7. The temperature curves in the tumour are almost equal, due to scaling of the total absorbed power in the patient volume. However, the temperature distribution in muscle and fat in the RF8 extends to very high values with a T_{10}(muscle) = 43.0°C, T_1(muscle) = 46.6°C and T_{10}(fat) = 43.5°C, T_1(fat) = 48.7°C. The temperature elevation in muscle and fat in the cavity slot applicator is moderate with T_{10}(muscle) = 39.3°C, T_1(muscle) = 41.1°C and T_{10}(fat) = 38.9°C, T_1(fat) = 40.2°C. For easy comparison the temperature indices are tabulated in table 6.4.

6.4 Discussion

In a patient the SAR distribution during regional hyperthermia treatment largely depends on the patient anatomy and the $\vec{E}$-field orientation of the applicator. As

(a)   (b)

(c)   (d)

Figure 6.4: SAR distribution in the patient volume generated in
(a,c) the RF8 applicator with overlay boli and (b,d) in the
cavity slot applicator, (a,b) transversal and (c,d) sagittal
slice. The slices are taken centrally through the tumour.
Black and white indicate SAR values from 0 to 125 Wkg^{-1}
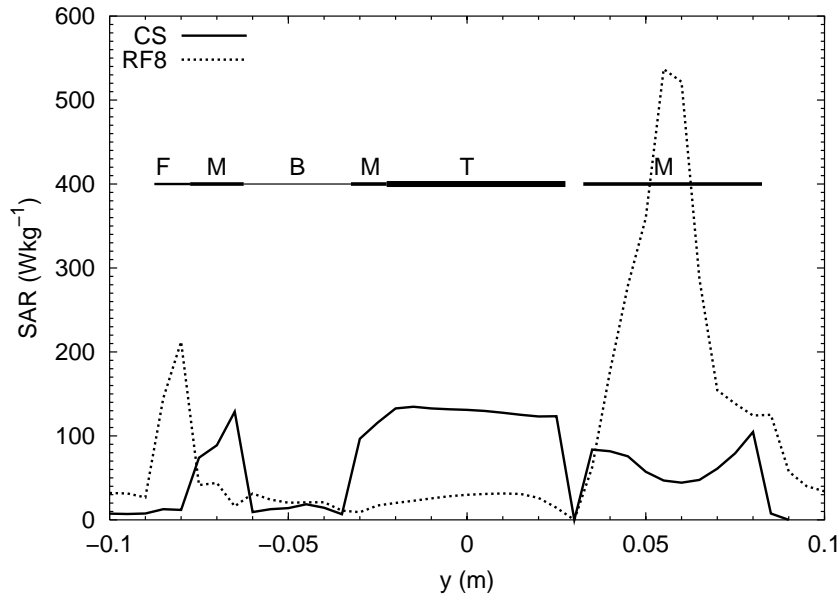
Figure 6.5: SAR profiles, anterior-posterior centrally in the tumour location in the patient model. Comparison of cavity slot (CS) applicator and RF8 applicator with overlay boli. Both SAR distributions normalized at 700 W total absorbed power.

Table 6.4: Performance indices, comparison of RF8 and cavity slot applicator

base	tissue	index	RF8	CS
SAR	tumour	Ti	2.2	4.5
	muscle	MMi	2.3	1.6
	fat	FMi	5.2	0.7
temperature	tumour	T_{90}	41.1	41.1
		T_{50}	42.0	42.1
		T_{10}	43.7	43.3
	muscle	T_{10}	43.0	39.3
		T_1	46.6	41.1
	fat	T_{10}	43.5	38.9
		T_1	48.7	40.2

(a)   (b)
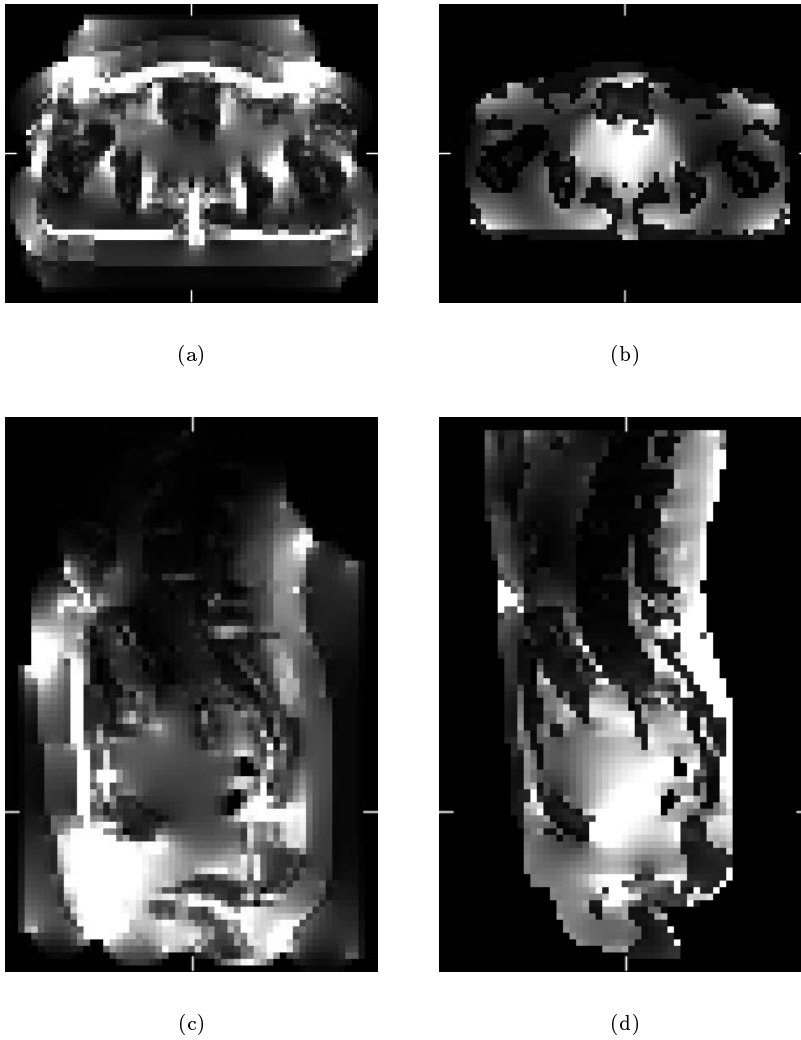
(c)   (d)   (e)
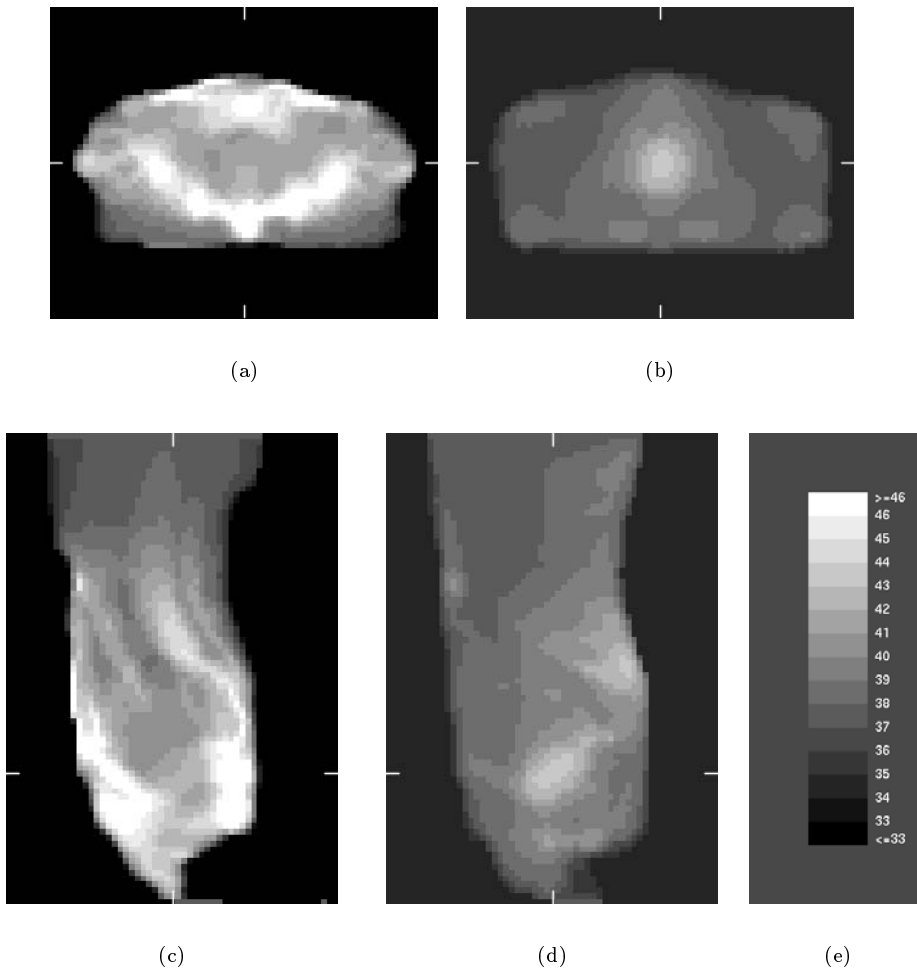
Figure 6.6: Temperature distribution in the patient volume gener-
ated in (a,c) the RF8 applicator and (b,d) in the cavity slot
applicator. (a,b) Transversal and (c,d) sagittal slice. The
slices are taken centrally through the tumour. (e) Tempera-
ture scale, for clarity the temperatures are truncated to 15
discrete levels from 32°C to 47°C.
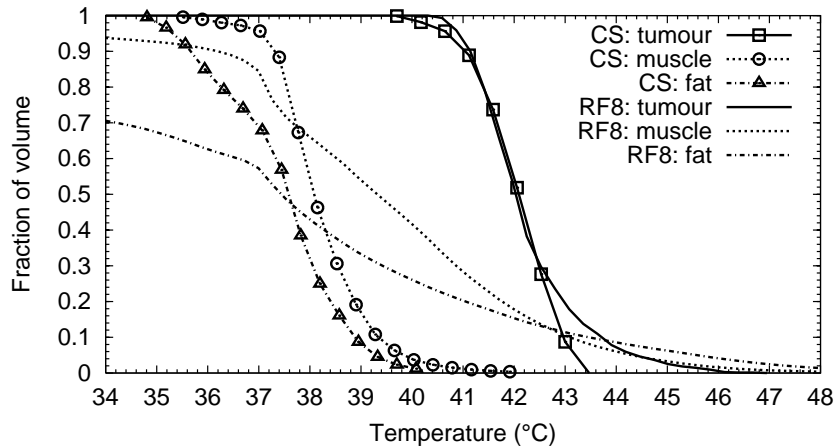
Figure 6.7: Cumulative histogram of the temperature distribution in the patient.

shown in the agar-bone phantom the configuration of the pelvic bone prevents optimal heating of a central tumour in a capacitive applicator. The isolating bone deflects the RF-current away from the centre, resulting in SAR maxima outside the tumour volume. The performance of the radiative applicators, however, is only partly influenced by the bone structure. The applicator is able to produce a distinct SAR maximum in the tumour volume.

A realistic patient anatomy, including fat layers, however, disturbs the SAR pattern in both applicator types. The orientation of the $\vec{E}$-field in a capacitive applicator is mainly perpendicular to the fat-muscle boundary, causing high SAR values in the fat layer despite the low conductivity of fat. The application of saline overlay bolus techniques (Kato *et al.*, 1997; Tomimatsu *et al.*, 1999a,b), body earthing techniques (Kosaka *et al.*, 1999) and impedance matching, or subtrap methods (Murata *et al.*, 1998) can be employed to circumvent this. However, comparison of the RF8 SAR track in the agar-bone phantom (figure 6.3) and in the patient model (figure 6.5) shows that even the relatively thin fat layers of this patient model cause a significant reduction of the SAR value in the tumour and an increase of the anterior and posterior SAR peaks, despite optimization using overlay boli.

The good SAR distribution obtained in the cavity slot applicator demonstrates

the favourable properties of multi-ring radiative annular phased array applicators (Wust *et al.* (1996); Paulsen *et al.* (1999) and Chapter 3). The $\vec{E}$-field orientation in the central transversal plane in a radiative applicator is oriented parallel to the fat-muscle boundary, resulting in very low SAR values in the superficial fat layer. However, outside the central transversal plane the $\vec{E}$-field is not everywhere oriented perfectly, causing unwanted maxima in the lumbo-sacral region, the perineum and near the omphalos. The optimization process is only partly able to suppress these maxima. Comparison of the cavity slot SAR track in the agar-bone phantom (figure 6.3) and in the patient model (figure 6.5) show also a reduction of the SAR value in the tumour caused by the fat structure, however, the ratio with the anterior and posterior peaks remains fair.

The marked difference in the SAR distributions in both applicator types naturally lead to different temperature distributions. The low SAR values in the tumour generated by the capacitive applicator lead to a high total absorbed power to obtain a median tumour temperature of 42°C. The high superficial SAR values cause temperature maxima outside the tumour volume that will probably cause sweating, thermoesthesia and fatigue, and limit the RF power (Nomoto *et al.*, 1999). The SAR maximum in the tumour generated by the radiative applicator allows a significant reduction of the total absorbed power needed to attain the tumour target temperature. This will reduce systemic stress and general discomfort. The unwanted SAR maxima outside the tumour volume cause only minor temperature maxima. The superficial temperature can be maintained low with minor skin cooling.

It has to be noticed, however, that the results obtained with the radiative applicator are theoretical and depend on the ability to optimize and control the SAR distribution. This implies full phase amplitude control of the system and accurate similarity of the patient position and posture in the applicator with the patient model used in the treatment planning process. Chapter 3 showed that a mere displacement of 2 cm of the patient already causes a deterioration of the performance indices. Seebass *et al.* (2001) investigated the influence of amplitude and phase errors at frequencies from 100 MHz to 200 MHz on the temperature distribution and found that this influence decreased with the increase of frequency.

6.5   Conclusion

New phase amplitude controlled radiative regional hyperthermia is a good alternative for capacitive techniques in the treatment of tumours in the pelvic region. The radiative coupling of the patient to the applicator avoids by nature some of the known disadvantages of capacitive systems, such as high superficial heating

and thermoesthesia. The large number of degrees of freedom enables the optimizing process to reduce treatment limiting SAR maxima. Whether these promising theoretical results can be obtained in daily clinical practice depends on progress in the field of phase amplitude control, applicator design and high-resolution hyperthermia treatment planning.

Chapter 7

Summary and general conclusions

7.1 Summary of this thesis

Hyperthermia is an adjuvant tumour therapy to radio- and/or chemotherapy, with the aim of enhancing the tumour-killing effect. It involves the elevation of the tumour temperature to ~42°C. Depending on the location and the volume of the tumour several heating modalities can be used to heat it, i.e. hot water tubes, ferro magnetic seeds, ultra sound, infra red radiation and electromagnetic waves in the radio frequent or microwave spectrum. Radio frequent electromagnetic radiation is the most extensively used hyperthermia modality; electromagnetic waves emanating from an external antenna array can penetrate the human body and cause a local temperature elevation. Microwave frequencies are used for superficial tumours, due to its limited penetration depth, where frequencies from 70 MHz up to 110 MHz are used to heat more deeply located tumours. The longer wavelength of the latter frequency band excludes a small absorption maximum and the method is called regional hyperthermia. Regional hyperthermia is applied to tumours in the pelvic region, like cervix, bladder, prostate and rectal carcinomas. Pelvic tumours can be heated with capacitive devices, operating at 8-13 MHz, and with radiative annular array applicators, operating from 70 MHz to 110 MHz. During regional hyperthermia treatment, in both applicator types, the occurrence of local pain, systemic heating and general discomfort limit the application of sufficient power to heat the tumour to its target temperature. The advent of numerical models to simulate the propagation and power deposition of electromagnetic waves in heterogeneous patient models and the temperature distribution in perfused tissue opened the way for accurate hyperthermia treatment planning and systematic research into hyperthermia equipment development.

This thesis addresses the use of electromagnetic and thermal simulation tools in order to investigate improvements in regional hyperthermia applicator devices and treatment techniques.

121

Chapter 1 gives a short introduction to clinical hyperthermia and discusses the physical means available to heat tumours. The limitations of the first generation applicator systems and treatment techniques for regional hyperthermia are reviewed.

In Chapter 2 the effect of rectangular, homogeneous absorbing blocks is discussed. Clinical experience in the Coaxial TEM applicator has shown that placement of absorbing blocks on local hot spots can reduce the pain and allow continuation of the treatment at the same power level. The absorbers are made of saline water that is solidified with agar. The effect of size and salinity of the absorber is evaluated on a phantom and on a patient model. An absorber can reduce the SAR in peripheral muscle and fat tissue by approximately a factor of 2. The presence of a fat layer between muscle and the absorber has a major influence on the attenuation pattern. More than 2 cm fat prevents the effective use of absorbers. Long absorbers (20 cm) have an effective depth up to 12 cm, so an attenuating effect on the central (i.e. tumour) region can be expected. Moreover, long absorbers can cause a disturbance of the global $\vec{E}$-field, resulting in SAR elevation in other regions. Short absorbers (10 cm) have a less penetrating effect, but the superficial effect is sufficient to obtain pain relieve. The effect on the central region is limited and global effects are small. Increasing the thickness and/or salinity of the absorbers also increases the effective depth. However, raising the salinity from 36 to 72 gram l^{-1} has hardly any additional effect. A significant SAR increase is induced at the edges of the absorber. This edge effect depends strongly on the thickness of the fat layer. The patient example showed that the SAR maximum under the absorber was successfully attenuated, but a new SAR maximum is induced at the lower edge of the absorber.

Chapter 3 investigates the performance of a next generation applicator system for Regional Hyperthermia with a multi ring annular array of antennas and an open water bolus. A cavity slot antenna is introduced to enhance the directivity and reduce mutual coupling between the antennas. Various design parameters: dimensions, number of antenna rings, number of antennas per ring and the operating frequency, have been evaluated using several patient models. A three ring applicator is clearly superior to one and two ring types. Six antennas per ring is sufficient for adequate SAR steering and hot spot avoiding. An upgrading to eight antennas per ring does not merit the cost. Evaluation of the SAR distribution in the patient models at 100 MHz, 150 MHz and 200 MHz indicate an optimal frequency of 150 MHz for the treatment of central pelvic tumours. Reduction of SAR in specific regions is also better achieved at 150 MHz. Additional evaluation of the temperatures obtained in the patient models confirmed this conclusion. Variation of the dielectric properties attributed to the patient tissues shows that the optimal performance at 150 MHz is not affected by a specific choice of the dielectric tissue properties. The effect of longitudinal and lateral patient shifts has been investi-

gated. The results show that uncertainty in the patient position can nullify the laboriously obtained advantages of applicator improvements and treatment optimization. This also indicates that the patient imaging has to be performed in an attitude similar to the patient posture in the applicator.

Chapter 4 investigates the effect of modification of shape, position and spatial composition of absorber blocks on the central attenuating effect and the SAR elevating effect at the edges. The effect of the various absorber types on the RF-current distribution is qualitatively analyzed using a quasi-static model. The quasi-static model indicates that the rerouting of current, with an inherent concentration at the edges, is the major consequence of the application of an absorber. With a sigma gradient absorber an optimal dispersion of this current can be obtained. A total annihilation of the edge effect is not possible. A phantom and a dipole ring applicator is used to enable 3-D FDTD simulation of the effect of modified absorbers at 4 mm resolution. The dipole ring applicator creates a central $\vec{E}$-field distribution similar to the Coaxial TEM applicator and operates at 70 MHz. It is shown that tapering of the absorber edge and the introduction of a water layer between the absorber and the skin can reduce the edge effect in the superficial fat layer by about 50% with respect to a rectangular absorber. A further reduction of 15% can be obtained by an absorber with an appropriate gradient of its conductivity in the direction of the dominant $\vec{E}$-field. In a patient model in the dipole ring applicator, operating at 70 MHz a similar behavior of the modified absorber types is observed. A reduction of about 30% can be obtained in the SAR peak ventral of the pubic bone, with a negligible reduction of the SAR in the tumour. The edge effect at the cranial side of the absorber is minimal with the sigma gradient absorber. The effect of the water layer and sigma gradient absorbers was also evaluated in the three ring cavity slot applicator, operating at 150 MHz. The effect of both absorber types is rather unlike its behaviour at 70 MHz. There is a marked difference in the effect on the SAR peak at the pubic bone. The water layer absorber produces a higher attenuation than the sigma gradient absorber. Furthermore the sigma gradient absorber causes a remarkable high edge effect. The quasi-static model of the absorber effect, i.e. rerouting of current is obviously not valid at 150 MHz Local SAR reduction by phase-amplitude control at 150 MHz can generate better results in terms of reduction ventral of the pubic bone, reduction of edge effect and SAR distribution in the tumor region.

In Chapter 5 a comprehensive treatment planning system, including a Specific Absorption Rate (SAR) and thermal model for capacitively coupled hyperthermia is described and demonstrated using a heterogeneous patient model. The Thermotron RF-8 is a capacitively coupled hyperthermia device that is in wide use, mainly in Asian countries. Asian patients are considered to be very suitable for capacitively coupled hyperthermia, due to their slender appearance, hence the patient model used in this study is of Asian origin. In order to accurately simulate a hyperther-

mia treatment, simulation at high resolution is mandatory. Using the quasi-static approximation, the electromagnetic problem can be solved at high resolution with a moderate computational effort. The validity of the quasi-static approximation is demonstrated by comparing the analytic solution of a phantom problem and an FDTD simulation to the quasi-static approximation. The basic characteristics of capacitive hyperthermia are related to the $\vec{E}$-field orientation perpendicular to the body surface and the low RF frequency. Simulation of capacitive hyperthermia of the prostate shows the difficulty of heating tumours located deeply in the pelvic region. Comparison of the SAR distribution in the heterogeneous patient model and a patient shaped agar phantom reveals a shielding effect of the pelvic bone and the influence of the fat-muscle distribution. It is shown that evaluation of capacitive hyperthermia with agar phantoms leads to overly optimistic conclusions. An adequate tumour temperature elevation can be obtained, however, not without causing very high temperatures in the superficial fat and muscle layers. The cooling effect of the bolus bags is only very superficial. The use of very cold overlay bolus bags has only a marginal influence on the superficial temperature distribution.

In Chapter 6 the performance of the Thermotron RF 8 applicator and the proposed open water bolus, cavity slot applicator operating at 150 MHz, is compared using an Asian patient model. The basic properties of both applicator types are demonstrated in a patient shaped agar-bone phantom. The configuration of the pelvic bone prevents optimal heating of a central tumour in the capacitive applicator. The isolating bone deflects the RF-current away from the centre, resulting in SAR maxima outside the tumour volume. The performance of the radiative applicators, however, is only partly influenced by the bone structure. The applicator is able to produce a distinct SAR maximum in the tumour volume. A realistic patient anatomy, including fat layers, however, disturbs the SAR pattern in both applicator types. The orientation of the $\vec{E}$-field in a capacitive applicator is mainly perpendicular to the fat-muscle boundary, causing high SAR values in the fat layer despite the low conductivity of fat. The use of saline overlay bolus bags can partly reduce this effect. The $\vec{E}$-field in the central transversal plane in a radiative applicator is oriented parallel to the fat-muscle boundary, resulting in very low SAR values in the superficial fat layer. This results in a good SAR distribution in the cavity slot applicator, that demonstrates the favourable properties of multi-ring radiative annular phased array applicators. The optimization process allows reduction of unwanted SAR maxima in normal tissue. The temperature distributions in both applicator types, with equal tumour temperatures, show very high superficial temperatures in the RF 8 applicator and a moderate temperature elevation in normal tissue in the radiative applicator. The SAR maximum in the tumour generated by the radiative applicator allows a significant reduction of the total

absorbed power needed to attain the tumour target temperature. This will reduce systemic stress and general discomfort.

7.2   General discussion

In general it can be concluded that simulation studies can improve the clinical application of hyperthermia, especially radiative regional hyperthermia. It is shown that the performance of both the first generation radiative applicators as well as the low frequency capacitive applicators can be improved significantly.

The performance of capacitive applicators can only be improved marginally by the application of overlay bolus bags (see Chapter 6) or the optimization of electrode location and size (Tsuda *et al.*, 1996). The basic $\vec{E}$-field orientation, i.e. perpendicular to the fat-muscle boundary and the low operating frequency prohibit further optimization of the capacitive applicator for the treatment of pelvic tumours.

Chapter 3 confirms the conclusion of several other studies (Wust *et al.*, 1996; Paulsen *et al.*, 1999; Seebass *et al.*, 2001) with respect to the number of antenna rings, the number of antennas per ring and the operating frequency of annular radiative applicators. The advantages of phase-amplitude control of the SAR distribution have been demonstrated on several patient models. It is, however, clear that a very fundamental problem remains in the practical application of regional hyperthermia, namely the positioning of the patient in the applicator. SAR optimization requires conformity of the simulated patient model and the actual patient. A practical way of solving this problem is the combination of a radiative applicator with a suitable imaging device. A Computed Tomography (CT) device can be used for position verification, however, the radiation dose excludes experiments with volunteers and places limits on the maximum number of scans during a treatment. There is no method available for non-invasive thermometry with a CT device. Magnetic Resonance Imaging (MRI) seems a more suitable candidate (Wust *et al.*, 2000), although the screening of the MRI receiving antennas from the radiating hyperthermia array and the limited space within the MRI magnet pose some hard problems. The outstanding advantage of combined hyperthermia treatment and MRI is the possibility of non invasive thermometry (Carter *et al.*, 1998). This technique can be readily demonstrated in phantoms, but is still problematic in perfused tissue and suffers from insufficient accuracy and resolution (Wlodarczyk *et al.*, 1998, 1999). Due to the spatial restrictions of the existing CT and MRI devices, integration of hyperthermia applicators is limited to the closed water bolus types. Integration with an open water bolus type applicator is not fundamentally impossible, but would require a totally new design of the CT or MRI device.

The capital question in the development of regional hyperthermia is hence: are we advancing to an open or a closed water bolus. A closed water bolus has several disadvantages, among which the bolus pressure, bolus edge effects due to fringing electric fields and insufficient cooling between the legs. Selection of MRI as means of thermometry depends on the future solution of the resolution problems in perfused tissue. On the other hand, in an open water bolus system, even the positioning problem is difficult to solve. Considering the advantages of open water bolus systems, the application of ultra sound as a positioning method should be further investigated. The open water bolus is an ideal medium for non contact ultrasound imaging. By selecting a suitable number of landmarks on bony structures in the planning image, the position of these landmarks can be verified in a number of ultrasound scans. Commercially available linear array and sector scanners are suitable for this task. Preliminary results indicate that non invasive thermometry is also possible using ultrasound (Seip and Ebbini, 1995; Ebbini, 2000). Hoffmann *et al.* (2000) performed ultrasonic temperature monitoring during transurethral microwave thermotherapy of the prostate.

Both imaging and non-invasive thermometry can also be performed with microwave techniques. Microwave tomographic reconstruction is especially interesting in the field of hyperthermia treatment planning, because it can map the complex permittivity of tissues (Franchois *et al.*, 1998). The application of microwave thermometry as a method of hyperthermia control was first described by Bolomey and Hawley (1990). Jacobsen and Staufer (2002) demonstrated microwave thermometry during superficial hyperthermia by measuring multi-band radiometric signals with a microwave dual-purpose body-contacting antenna. This method is, however, only capable of measuring temperatures up to a depth of a few centimeters. Hand *et al.* (2001) monitored deep brain temperatures in infants using multi-frequency microwave radiometry and thermal modelling. The antennas used for microwave radiometry can readily be incorporated in the design of the cavity slot array antenna, due to the small dimensions of the microwave antennas. The basic problem of microwave radiometry, i.e. the extremely low signal, can be partly solved by locating the microwave antenna array as close as possible to the patient (Jacobsen and Staufer, 2002).

The generator system needed to perform successful regional hyperthermia treatment in an open water bolus phased array applicator has to be designed to tight specifications. The maximal available power in the single generator Coaxial TEM system is 2500 W. This is hardly sufficient to reach a tumour temperature of 42 °C in a typical treatment. When we assume that the gain in tumour heating efficiency in the phased array applicator (see Chapter 3) is sufficient to obtain satisfactory tumour temperatures, we can take the same figure as the total power required at the antennas. In a typical treatment optimization with a power constraint per antenna of 10% of the total power, several antennas require this maximum power

setting, hence a power of 250 W per antenna has to be available. In the generator system, each channel has to be equipped with a circulator, in order to define the generator impedance (see Chapter 3). This circulator and the connecting cable between generator and antenna introduce an insertion loss of at least 1 dB, or about 20%, hence the final amplifier stage has to be specified at 300 W. Straightforward construction of an 18 channel generator system would call for a total RF power of 5400 W and, with a conservative estimate of the efficiency on the final RF stages of 50%, a total supply power in excess of 10 kW. A design, however, of a DC power distribution bus can reduce the total power supply power to 6 kW for a total available RF power of 3 kW, significantly reducing the cooling requirements of the generator system. The generator system has to be equipped with accurate measuring devices for forward and reflecting amplitude and phase. This will enable measurement of the antenna coupling with the patient inserted in the applicator. Measurement of this scattering matrix enables an improvement of phase-amplitude control (Raskmark *et al.*, 1994b). The measurement of phase at 150 MHz depends critically on the length of cables in the system. In a typical cable the wavelength is 1.2 m, so a length of 3 mm corresponds to a phase difference of 1 degree. Constant differences in cable length can be calibrated out, however, temperature differences in the system can change the electrical length of a cable due to changes of the permittivity of the dielectricum. Multi-path calibration techniques can cancel out the influence of variable cable length; the application of this technique needs to be investigated for implementation in regional hyperthermia generator systems. The general configuration of an ideal generator system would be a modular combination of amplifier channels, that can be assembled to any number of channels and modified to operate at frequencies in the range from 100 MHz to 200 MHz. Due to limitations in the bandwidth of circulators, it is in general not feasible to design a generator system with a variable operating frequency over this full range.

Quality control of regional hyperthermia treatments requires a check of the SAR distribution and a global comparison with the planning results at the start of the treatment. This is usually done with a single of double RF power pulse and the consecutive measurement of the temperature change (De Leeuw *et al.*, 1993). When the applicator is combined with any means of non-invasive thermometry, this measurement of a relatively small temperature change will be hampered by the limited accuracy and resolution of the available techniques. It would be useful to overcome this problem, to be able to apply an initial RF power pulse at an increased level. The technical feasibility of this power burst technique needs to be investigated.

As previously discussed (see Chapter 3), the positioning of the patient is the main problem of the design of a new applicator system. The new design needs to incorporate several partly conflicting innovations, among which: increased patient comfort, patient posture in applicator conformable with posture in imaging device,
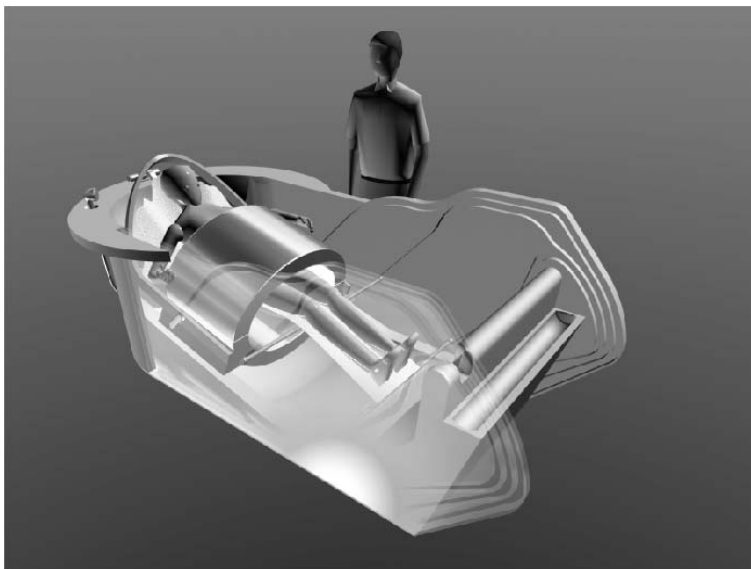
Figure 7.1: Impression of a new open water bolus regional hyper-
thermia applicator (by courtesy of E.B. van der Houwen).

repeatability of the patient posture over all treatment sessions, temperature man-
agement of the water bolus and possibly a combination with an imaging device
and a non-invasive thermometry system. To allow easy insertion of the patient,
the array of cavity slot antennas will have to be foldable or collapsible, which will
pose a problem due to the weight of the water-filled cavities. All design aspects
have been the subject of a preliminary design study (Van der Houwen, 1999), fig-
ure 7.1 gives an impression of the proposed new water bolus regional hyperthermia
applicator.

The design and commissioning of a new regional hyperthermia system can no
longer be the undertaking of a single research group or commercial enterprise,
due to the large costs and the multiple scientific and technical difficulties encoun-
tered. International cooperation and sharing of hardware and software resources is
mandatory. Our institute is fortunate to be able to join forces with groups in Japan,
the United States and Europe on its mission to improve regional hyperthermia.

Hoofdstuk 8

Samenvatting

Hyperthermie is een behandelwijze die kan worden toegevoegd aan radiotherapie en/of chemotherapie, met het doel het tumor-dodend effect te vergroten. Het behelst de verhoging van de tumortemperatuur tot $\sim 42°C$. Afhankelijk van de locatie en de afmetingen van de tumor zijn er verschillende verwarmingsmethoden beschikbaar, zoals warmwater slangen, ferro-magnetische zaadjes, ultrageluidsgolven, infrarood straling en electromagnetische golven in het radiofrequente of microgolf spectrum. Radiofrequente golven zijn de meest toegepaste hyperthermie methode: één of meer buiten het lichaam opgestelde antennes stralen golven uit, die het lichaam binnentreden en zo een locale temperatuurverhoging veroorzaken. Microgolf frequenties worden doorgaans alleen gebruikt voor het verwarmen van oppervlakkige tumoren, gezien de beperkte indringdiepte. De frequentieband van 70 MHz tot 110 MHz wordt gebruikt voor het verwarmen van dieper gelegen tumoren. De grotere golflengte van deze frequentieband sluit een klein absorptiemaximum uit, de methode wordt derhalve regionale hyperthermie genoemd. Regionale hyperthermie wordt toegepast op tumoren in het bekkengebied, zoals baarmoederhals, blaas, prostaat en rectale tumoren. Tumoren in het bekkengebied kunnen worden verwarmd met capacitief gekoppelde systemen, die in de frequentieband van 8 MHz tot 13 MHz werken, en met radiatieve ringvormige array applicators met een werkingsfrequentie van 70 MHz tot 110 MHz. In beide applicator types treden gedurende de hyperthermiebehandeling effecten op die het totaal toegediende vermogen beperken, zoals locale pijn, algehele verhoging van de lichaamstemperatuur en algemeen ongemak (misselijkheid en vermoeidheid). Door de beperking van het totale vermogen kan vaak niet de gewenste tumortemperatuur worden bereikt. De recente opkomst van numerieke modellen die het gedrag van electromagnetische golven in een heterogeen patiëntmodel en de temperatuurverdeling in doorbloed weefsel kunnen simuleren, maakt een nauwkeurige planning van de hyperthermie behandeling mogelijk. Tevens kunnen deze modellen, met name het FDTD SAR model, worden toegepast voor het ontwerpen van nieuwe hyperthermie apparatuur.

Dit proefschrift behandelt het gebruik van electromagnetische en thermische modellen voor het verbeteren van hyperthermie systemen en behandelingstechnieken.

Hoofdstuk 1 geeft een korte introductie van de klinische aspecten van hyperthermie. Het laat de beschikbare fysische methoden voor het verwarmen van tumoren de revue passeren. Tevens worden de beperkingen van de eerste generatie applicator systemen en behandelingstechnieken bediscussieerd.

In Hoofdstuk 2 wordt het effect van rechthoekige, homogene absorberende blokjes behandeld. Uit klinische ervaring met het Utrechtse Coaxiale TEM systeem blijkt dat het plaatsen van absorberende blokjes op locale 'hot spots' de pijn kan reduceren, waardoor de behandeling met het zelfde vermogen kan worden voortgezet. Deze absorberende blokjes bestaan uit zout water, dat met behulp van agar is gebonden tot een gel-achtige massa. Het effect van de afmetingen en de zoutgraad van de blokjes op de verzwakkende werking is modelmatig onderzocht in een homogeen fantoom en een heterogeen patiëntmodel. Het blijkt dat een absorberend blokje de specifieke vermogens absorptie (SAR) in oppervlakkig spier- en vetweefsel met een factor 2 kan reduceren. De aanwezigheid van een vetlaag tussen de spiermassa en het blokje heeft een belangrijke invloed op het verzwakkingspatroon. De aanwezigheid van meer dan 2 cm vet verhindert een effectief gebuik van absorberende blokjes. Blokjes met een lengte van 20 cm vertonen een effect tot een diepte van 12 cm, waardoor een ongewenst verzwakkend effect op de centraal gelegen tumor kan worden verwacht. Voorts kunnen lange blokjes een verstoring veroorzaken van het globale $\vec{E}$-veld, wat resulteert in SAR verhoging op andere locaties. Kortere blokjes, met een lengte van 10 cm hebben een minder diep doordringend effect, het oppervlakkige effect is echter voldoende voor locale pijnbestrijding. Het verzwakend effect in het centrale gebied is beperkt en de globale effecten zijn klein. Verhoging van de dikte en/of de zoutgraad van de blokjes verhoogt de werkingsdiepte, verhoging van de zoutgraad van 36 to 72 gram l^{-1} heeft echter nauwelijks enig toegevoegd effect. Aan de randen van de absorberende blokjes wordt een belangrijke toename van de SAR geïnduceerd. Dit randeffect hangt sterk af van de dikte van de vetlaag. In het patiëntmodel kan worden gedemonstreerd dat een SAR maximum onder het blokje succesvol wordt verzwakt, maar dat een nieuw SAR maximum wordt veroorzaakt aan de benedenrand van het blokje.

In Hoofdstuk 3 wordt de werking van een nieuw applicator systeem voor regionale hyperthermie, uitgevoerd met een meer-rings antenne array en een open waterbolus onderzocht. De introductie van een antenne array maakt electronische SAR sturing mogelijk door middel van fase-amplitude modulatie van de spanning op de antenneklemmen. Een cavity slot antenne wordt gebruikt ter verbetering van de richtbaarheid en ter vermindering van de wederzijdse koppeling van de antennes. Verschillende ontwerpparameters, zoals de afmetingen, het aantal antenne ringen, het aantal antennes per ring en de werkfrequentie worden geëvalueerd met gebruik-

making van verschillende patiëntmodellen. Een applicator met drie antenneringen is duidelijk superieur aan types met één of twee antenneringen. Zes antennes per ring is voldoende voor adequate SAR sturing en het vermijden van locale hot spots. Het toegevoegd effect van acht antennes per ring weegt niet op tegen de extra kosten. Beoordeling van de SAR verdeling in verschillende patiëntmodellen op 100 MHz, 150 MHz en 200 MHz geeft aan dat 150 MHz een optimale frequentie is voor de behandeling van centraal gelegen bekkentumoren. Nadere beoordeling van de verkregen temperatuurverdelingen bevestigen deze conclusie. Variatie van de diëlectrische eigenschappen die worden toegekend aan de verschillende weefseltypes toont aan dat de optimale werking bij 150 MHz niet wordt beïnvloed door een toevallige keuze van de diëlectrische eigenschappen uit de spreiding in de literatuur waardes. Het effect van longitudinale en laterale verschuivingen van de patiënt is onderzocht. Het blijkt dat onzekerheid in de positie van de patiënt de moeizaam verkregen verbetering van de applicator en de optimalisatie van de behandeling te niet kan doen. Hieruit wordt duidelijk dat de CT-beeldvorming van de patiënt moet worden uitgevoerd in dezelfde houding als welke de patiënt aanneemt in de applicator.

In Hoofdstuk 4 wordt het effect bestudeerd van verandering van de vorm, positie en ruimtelijke samenstelling van absorberende blokjes op de centrale verzwakkende werking en het SAR verhogende randeffect. Het effect van de verschillende types op de RF stroomverdeling wordt kwalitatief onderzocht met behulp van een quasi-statisch model. Uit deze studie blijkt dat de toepassing van een absorberend blokje een herverdeling van de stroomdichtheid tot gevolg heeft, met een onvermijdelijke concentratie nabij de randen van het blokje. Met behulp van een blokje met een langs de lengte variërend zoutgehalte, dus met een gradient van de electrische geleiding (σ), kan een optimale spreiding van de stroomdichtheid worden verkregen, het randeffect kan echter niet volledig te niet gedaan worden. Een fantoom en een ringvormige dipool applicator worden gebruikt om het effect van de gemodificeerde blokjes te bestuderen met een 3-D FDTD model op een resolutie van 4 mm. De ringvormige dipool applicator, werkend op 70 MHz, genereert een centrale $\vec{E}$-veld verdeling die gelijkvormig is aan de veldverdeling in de coaxial TEM applicator. Het blijkt dat afschuining van de rand van het blokje en het introduceren van een waterlaag tussen de huid en het blokje het randeffect kan halveren ten opzichte van een vergelijkbaar rechthoekig blokje. Een verdere reductie van 15% kan worden bereikt door het blokje een geschikte sigma-gradient in de richting van het dominante $\vec{E}$-veld te geven. In een patiëntmodel in de ringvormige dipool applicator, werkend op 70 MHz, kan een soortgelijk gedrag worden waargenomen. Een afname van 30% van de SAR piek voor het schaambeen kan worden verkregen met een verwaarloosbare verzwakking van de SAR in de tumor. Het randeffect van het blokje is minimaal bij toepassing van een sigma-gradient. Het effect van blokjes met een waterlaag of een sigma-gradient is eveneens geëvalueerd in de drie rings

cavity slot applicator, werkend op 150 MHz. Het effect van de blokjes op deze frequentie is sterk verschillend van het gedrag op 70 MHz, er is een duidelijk verschil in de verzwakking van de SAR piek voor het schaambeen. Het waterlaag blokje veroorzaakt een hogere verzwakking dan het sigma-gradient type, verder veroorzaakt het laatste blokje een opmerkelijk hoog randeffect. Het quasi-statische model van SAR verzwakking door het omleiden van stromen is kennelijk niet meer geldig op 150 MHz. Locale SAR reductie door middel van fase-amplitude sturing op 150 MHz is beter in termen van verzwakking voor het schaambeen, onderdrukking van het randeffect en de SAR verdeling in de tumor.

Een alternatief voor radiatieve hyperthermie handeling is capacitieve verwarming. De Thermotron RF-8 is een capacitief gekoppeld hyperthermie systeem met een werkfrequentie van 8 MHz, dat veel in Aziatische landen wordt gebruikt. Aziatische patiënten worden zeer geschikt geacht voor capacitief gekoppelde hyperthermie door hun slanke voorkomen. In Hoofdstuk 5 wordt een volledig plannings systeem beschreven voor capacitief gekoppelde hyperthermie, dat zowel een SAR model als een thermisch model omvat. Dit plannings systeem wordt gedemonstreerd met een patiëntmodel van Aziatische oorsprong. Ten einde nauwkeurige model resultaten te verkrijgen, is het noodzakelijk de simulatie op hoge resolutie uit te voeren. Met behulp van de quasi-statische benadering kan het betreffende electromagnetische probleem op hoge resolutie in betrekkelijk korte tijd worden opgelost, dankzij de gunstige verhouding van de golflengte in weefsel en de patiëntafmetingen. De geldigheid van deze quasi-statische benadering wordt aangetoond door de analytische oplossing van een fantoom probleem en een FDTD simulatie te vergelijken met de quasi-statische benadering. De basale eigenschappen van capacitief gekoppelde hyperthermie zijn gerelateerd aan het loodrecht op het lichaam georiënteerde $\vec{E}$-veld en de lage werkfrequentie. Simulatie van capacitief gekoppelde hyperthermie van een prostaattumor toont de moeilijkheid van het verwarmen van diep gelegen bekkentumoren met deze techniek. Uit een vergelijking van de SAR verdeling in het heterogene patiëntmodel en in een gelijkvormig, homogeen agar fantoom blijkt de afschermende werking van het schaambeen. Dit toont aan dat de beoordeling van capacitief gekoppelde hyperthermie systemen met behulp van homogene fantomen leidt tot veel te optimische conclusies. Het is mogelijk een voldoende tumor temperatuur te bereiken, echter niet zonder zeer hoge temperaturen te veroorzaken in de oppervlakkige spier- en vetlagen. Het koelend effect van de bolus zakken is zeer oppervlakkig. Het toepassen van zeer koude tussengevoegde bolus zakken heeft slechts een marginaal effect op de temperatuurverdeling in de oppervlakkige weefsellagen.

In Hoofdstuk 6 worden de eigenschappen van het Thermotron RF-8 systeem en het in Hoofdstuk 3 voorgestelde open waterbolus, cavity slot systeem vergeleken. Hierbij wordt gebruik gemaakt van een Aziatisch patiëntmodel. De basale eigenschappen van beide applicatoren worden gedemonstreerd met behulp van een agar-bot

fantoom, in de vorm van het patiëntmodel. De vorm van het bekkenbot verhindert effectieve capacitieve verwarming van een centraal gelegen tumor, omdat het bot de RF stromen afbuigt van het centrale gebied. Dit resulteert in SAR maxima buiten het tumor volume. De radiatieve applicator wordt veel minder beinvloed door de botstructuur en kan daardoor het SAR maximum in het tumorvolume leggen. In een realistisch patiëntmodel, compleet met vetlagen, wordt het SAR patroon van beide applicator types verstoord door de anatomie. In een capacitief gekoppelde applicator is het $\vec{E}$-veld hoofdzakelijk loodrecht op de vet-spier overgangen georienteerd. Dit veroorzaakt hoge SAR waardes in het vet, ondanks de lage geleiding van vet. Het gebruik van met zout water gevulde zakken tussen de electrode bolus zakken de de patiënt kan dit effect reduceren. Het $\vec{E}$-veld in het centrale vlak van de radiatieve applicator is evenwijdig aan de vet-spier overgangen georienteerd, hetgeen een zeer lage SAR waarde in de oppervlakkige vetlagen tot gevolg heeft. De goede SAR verdeling in de cavity slot applicator demonstreert de goede eigenschappen van meer-rings radiatieve, fase-amplitude gestuurde array applicatoren. Door middel van fase-amplitude sturing kunnen ongewenste SAR maxima in normaal weefsel worden verlaagd. Een vergelijking van de de temperatuurverdeling in beide applicator types met gelijke temperatuur in de tumor, laat zeer hoge oppervlakkige temperaturen zien in de capacitief gekoppelde applicator en een matige temperatuurstijging in het gezonde weefsel in de radiatieve applicator. Het goede SAR maximum in de tumor, dat wordt gegenereerd door de radiatieve applicator, laat een aanzienlijke daling van het totaal toegediend vermogen toe dat nodig is om de tumor tot de doeltemperatuur te verwarmen. Dit is gunstig voor de belasting en het algemeen welbevinden van de patiënt.

In het algemeen kan worden geconcludeerd dat modelstudies de klinische applicatie van hyperthermie, regionale hyperthermie in het bijzonder, kunnen verbeteren. De studies wijzen uit dat zowel de eerste generatie radiatieve applicatoren, als de laag frequente capacitief gekoppelde applicatoren aanzienlijk verbeterd kunnen worden. Deze verbetering is echter afhankelijk van de mogelijkheid om de patiënt in de applicator te positioneren in een houding die gelijk is aan de houding in de CT-scanner. Dit kan worden gerealiseerd door de applicator te combineren met een apparaat dat de patiënt kan afbeelden. Een MRI toestel is hiervoor zeer geschikt, mede omdat het mogelijk is tijdens de behandeling niet-invasief de temperatuur te meten. Het is echter zeer moeilijk om een MRI apparaat te combineren met een hyperthermie applicator met open waterbolus. Een applicator met gesloten waterbolus heeft helaas een aantal nadelen, zoals de druk van de waterbolus en de invloed van de boluszakken op de $\vec{E}$-veld verdeling.

Patiënt positionering in een open waterbolus systeem kan ook met ultrageluid apparatuur worden uitgevoerd. Een open waterbolus is een ideaal medium voor contactloze ultrageluid afbeeldingstechnieken. Commercieel verkrijgbare lineair array- en sectorscanners zijn geschikt voor deze taak. In het patiëntmodel kunnen een

geschikt aantal vaste punten op de botstructuur worden gekozen, die met behulp van de ultrageluids afbeeldingsapparatuur in de applicator worden gepositioneerd. Voorlopige resultaten geven aan dat met ultrageluid eveneens niet-invasieve thermometrie mogelijk is.

Om een hyperthermie behandeling met behulp van fase-amplitude sturing te kunnen geven is een generator systeem nodig dat de vereiste fase- en amplitudemodulatie kan uitvoeren. Het totaal benodigde RF vermogen kan op grond van ervaring met het coaxiale TEM systeem op 2500 W geschat worden. In het SAR optimalisatie algorithme wordt doorgaans het vermogen per kanaal beperkt tot 10% van het totale vermogen. Hieruit volgt dat per kanaal 250 W beschikbaar moet zijn. Rekening houdend met kabelverliezen wordt dit tot 300 W verhoogd. Een 18 kanaals generator zou dan 5400 W moeten leveren, hetgeen met een conservatieve schatting van het rendement van de eindtrappen van 50% op een totaal voedingsvermogen van meer dan 10 kW komt. Toepassing van een DC distributiebus kan het totaal voedingsvermogen terugbrengen tot 6 kW voor een total RF vermogen van 3 kW, hetgeen de vereiste koeling aanzienlijk reduceert. Het generator systeem moet uitgerust worden met een nauwkeurig meetsysteem voor fase en amplitude van het voorwaardse en gereflecteerde vermogen. De meting van fase op 150 MHz is sterk afhankelijk van kabellengtes in het systeem. De golflengte in een kabel is circa 1.2 m, dus een lengte van 3 mm correspondeert met een faseverschil van 1 graad. Constante lengteverschillen kunnen door middel van calibratie worden gecompenseerd, temperatuurverschillen kunnen echter de electrische lengte van kabels doen variëren. Door meervoudige meting langs verschillende kabelpaden kunnen deze fouten dynamisch worden gecompenseerd. De algemene opbouw van een hyperthermie generatorsysteem bestaat uit een modulaire combinatie van versterker elementen, die kunnen worden samengebouwd tot ieder gewenst aantal en dat kan worden geconfigureerd voor frequenties van 100 MHz tot 200 MHz. Door beperking van de bandbreedte van de gebruikte circulatoren is het ontwerp van een systeem met instelbare frequentie niet haalbaar.

Het ontwerp en de opbouw van een nieuw regionaal hyperthermie systeem is een project dat niet meer gedragen kan worden door een enkele onderzoeksgroep, door de hoge kosten en de veelzijdige wetenschappelijke en technische problemen. Ons instituut is in de gelukkige omstandigheid te kunnen samenwerken met groepen in Japan, de Verenigde Staten en Europa om te komen tot verbetering van regionale hyperthermie behandeling.

References

Anscher M S, Samulski T V, Dodge R, Prosnitz L R and Dewhirst M W 1997 Combined external beam irradiation and external regional hyperthermia for locally advanced adenocarcinoma of the prostate *International Journal of Radiation Oncology, Biology and Physics* **37** 1059–1065

Armitage D W, LeVeen H H and Pethig R 1983 Radiofrequency-induced hyperthermia: computer simulation of specific absorption rate distributions using realistic anatomical models *Physics in Medicine and Biology* **28** 31–42

Bardati F, Borrani A, Gerardino A and Lovisolo G 1995 SAR optimisation in a phased array radiofrequency hyperthermia system *IEEE Transactions on Biomedical Engineering* **42** 1201–1207

Ben-Yosef R, Sullivan D M and Kapp D S 1992 Peripheral neuropathy and myonecrosis following hyperthermia and radiation therapy for recurrent prostatic cancer: correlation of damage with predicted SAR pattern *International Journal of Hyperthermia* **8** 173–185

Berntsen S and Hornsleth S N 1994 Retarded time absorbing boundary conditions *IEEE Transactions on Antennas and Propagation* **42** 1059–1064

Berry J M, Michalsen A, Nagle V and Bull J M 1997 The use of esmolol in whole-body hyperthermia: cardiovascular effects *International Journal of Hyperthermia* **13** 261–268

Bolomey J C and Hawley M S 1990 Noninvasive control of hyperthermia in *Methods of Hyperthermia Control, Clinical Thermology, Subseries Thermotherapie*, ed. M Gautherie (Berlin, Germany: Springer-Verlag)

Brezovich I A, Meredith R F, Henderson R A, Brawner W R, Weppelmann B and Salter M M 1989 Hyperthermia with water-perfused catheters in *Hyperthermic Oncology 1988*, eds. T Sugahara and M Saito vol. 1 pp. 809–810 (London, UK: Taylor & Francis)

Carter D L, MacFall J R, Clegg S T, Wan X, Prescott D M, Charles H C and Samulski T V 1998 Magnetic resonance thermometry during hyperthermia for human high-grade sarcoma *International Journal of Radiation Oncology, Biology and Physics* **40** 815–822

Cetas T C, Gross E J and Contractor Y 1998 A ferrite core metallic sheath thermoseed for interstitial thermal therapies *TBE* **45** 68–77

Clegg S T, Das S K, Fullar E, Anderson S, Blivin J, Oleson J R and Samulski T V 1996 Hyperthermia treatment planning and temperature distribution reconstruction: a case study *International Journal of Hyperthermia* **12** 65–76

Cleton F J, Van Leer E M and Van Leeuwen F E 1999 Signaleringsrapport kanker 1999

Collin R E 1985 *Antennas and radiowave propagation* (New York, USA: McGraw-Hill)

Corry P M, Spanos W J, Tilchen E J, Barlogie B, Barkley H T and Armour E P 1982 Combined ultrasound and radiation therapy treatment of human superficial tumors *Radiology* **145** 165–169

Craciunescu O I, Raaymakers B W, Kotte A N T J, Das S K, Samulski T V and Lagendijk J J W 2001 Discretising large traceable vessels and using DE-MRI perfusion maps yields numerical temperature contours that match the MR non-invasive measurements. results of a collaboration between University Medical Center Utrecht and Duke University Medical Center *Medical Physics* **28** 2289–2296

Crezee J, Mooibroek J, Bos C K and Lagendijk J J W 1991 Interstitial heating: experiments in artificially perfused bovine tongues *Physics in Medicine and Biology* **36** 823–833

Dahl 0 1995 Interaction of heat and drugs *in vitro* and *in vivo* in *Thermoradiotherapy and Thermochemotherapy: Biology, Physiology and Physics*, eds. M H Seegenschmiedt, P Fessenden and C C Vernon vol. 1 pp. 103–121 (Berlin, Germany: Springer-Verlag)

Das S K, Clegg S T and Samulski T V 1999a Computational techniques for fast hyperthermia temperature optimization *Medical Physics* **26** 291–308

Das S K, Clegg S T and Samulski T V 1999b Electromagnetic thermal therapy power optimisation for multiple source applicators *International Journal of Hyperthermia* **15** 291–308

De Bree J 1998 *A 3-D anatomy based treatment planning system for interstitial hyperthermia* Ph.D. thesis Utrecht University

De Bree J, Van der Koijk J F and Lagendijk J J W 1996 A 3-D SAR model for current source interstitial hyperthermia *IEEE Transactions on Biomedical Engineering* **43** 1038–1045

De Leeuw A A C 1993 *The Coaxial TEM regional hyperthermia system* Ph.D. thesis Utrecht University

De Leeuw A A C, Crezee J and Lagendijk J J W 1993 Temperature and SAR measurements in deep-body hyperthermia with thermocouple thermometry *International Journal of Hyperthermia* **9** 685–697

De Leeuw A A C and Lagendijk J J W 1987 Design of a deep-body hyperthermia system based on the 'Coaxial TEM' applicator *International Journal of Hyperthermia* **3** 413–421

De Leeuw A A C, Mooibroek J and Lagendijk J J W 1991 SAR-steering by patient positioning in the 'Coaxial TEM' system: phantom investigation *International Journal of Hyperthermia* **7** 605–611

De Leeuw A A C, Mooibroek J, Wijrdeman H K and Lagendijk J J W 1994 Three-dimensional SAR steering by inhomogeneous bolus loading in the Coaxial TEM hyperthermia system in *ESHO-94: Abstracts* p. 27 Amsterdam, The Netherlands European Society for Hyperthermic Oncology

De Leeuw A A C, Van Vulpen M, Wárlám-Rodenhuis C C, Van de Kamer J B, Kroeze H and Lagendijk J J W 1999 Regulating the systemic temperature during regional hyperthermia in *ESHO-99: Abstracts* p. 72 Rotterdam, The Netherlands European Society for Hyperthermic Oncology

Deardorff D L, Diederich C J and Nau W H 1998 Air-cooling of direct-coupled ultrasound applicators for interstitial hyperthermia and thermal coagulation *Medical Physics* **25** 2400–2409

Diederich C J and Hynynen K H 1993 Ultrasound technology for interstitial hyperthermia in *Interstitial and Intracavitary Thermoradiotherapy*, eds. M H Seegenschmiedt and R Sauer pp. 55–61 (Berlin, Germany: Springer-Verlag)

Dinges S, Harder C, Wurm R, Buchali A, Blohmer J, Gellermann J, Wust P, Randow H and Budach V 1998 Combined treatment of inporable carcinomas of the uterine cervix with radiotherapy and regional hyperthermia *Strahlentherapie und Onkologie* **174** 517–521

Dirks H K 1988 *Kapazitätskoefficienten Nichtlinearer Dissipativer Systeme* chap. Quasistationäre elektromagnetische Felder, pp. 6–21 (Technischen Hochschule Aachen)

Ebbini E 2000 Non-invasive two dimensional temperature imaging using ultrasound in *ICHO-2000: Abstracts* p. 240 Kyŏngju, South-Korea International Congress of Hyperthermic Oncology

Egawa S, Tsukiyama I, Akine Y, Kajiura Y, Ogino T and Yamashita K 1988 Hyperthermic therapy of deep seated tumors: comparison of the heating efficiencies of an annular array applicator and a capacitively coupled radiofrequency system *International Journal of Radiation Oncology, Biology and Physics* **14** 512–528

Emami B, Myerson R J, Scott C, Gibbs F, Lee C and Perez C A 1991a PhaseI/II study, combination of radiotherapy and hyperthermia in patients with deep-seated malignant tumours: Report of a pilot study by radiation therapy oncology group *International Journal of Radiation Oncology, Biology and Physics* **20** 73–79

Emami B, Scott C, Perez C A, Asbell S, Swift P, Grigsby P, Montesano A, Rubin P, Curran W, Delrowe J, Arastu H, Fu K and Moros E 1996 Phase III study of interstitial thermoradiotherapy compared with interstitial radiotherapy alone in the treatment of recurrent or persistent human tumors: A prospectively controlled randomized study by the Radiation Therapy Oncology Group. *International Journal of Radiation Oncology, Biology and Physics* **34** 1097–1104

Emami B, Stauffer P, Dewhirst M W, Prionas S, Ryan T, Corry P, Herman T, Kapp D S, Myerson R J, Samulski T V *et al.* 1991b RTOG quality assurance guidelines for interstitial hyperthermia *International Journal of Radiation Oncology, Biology and Physics* **20** 1117–1124

ESHO Taskgroup Committee 1992 *Treatment Planning and Modelling in Hyperthermia, a Task Group Report of the European Society for Hyperthermic Oncology* (Rome, Italy: Tor Vergata)

Fenn A J and King G A 1996 Experimental investigation of an adaptive feedback algorithm for hot spot reduction in radio-frequency phased-array hyperthermia *IEEE Transactions on Biomedical Engineering* **43** 273–280

Franchois A, Joisel A, Pichot C and Bolomey J C 1998 Quantitative microwave imaging with a 2.45 GHz planar microwave camera *IEEE Transactions on Medical Imaging* **17** 550–561

Gabriel C 1996 Compilation of the dielectric properties of body tissues at rf and microwave frequencies *Brooks Air Force Technical Report AL/OE-TR-1996-0037*

Gabriel C, Gabriel S and Corthout E 1996 The dielectric properties of biological tissues: I. literature survey *Physics in Medicine and Biology* **41** 2231–2249

Gantenberg J, Mumme A, Zumtobel V and Werner J 2001 Assessment of the temperature distribution during hyperthermia treatment by isolated extremity perfusion *International Journal of Hyperthermia* **17** 189–206

Hand J W, Lagendijk J J W, Hajnal J V, Lau R W and Young I R 2000 SAR and temperature changes in the leg due to an RF decoupling coil at frequencies between 64 and 213 MHz *Journal of Magnetic Resonance Imaging* **12** 68–74

Hand J W, Machin D, Vernon C C and Whaley J B 1997 Analysis of thermal parameters obtained during phase III trials of hyperthermia as an adjunct to radiotherapy in the treatment of breast carcinoma *International Journal of Hyperthermia* **13** 343–364

Hand J W, Trembly B S and Prior M V 1991 Physics of interstitial hyperthermia, radiofrequency and hot water tube techniques in *Hyperthermia and Oncology*, eds. M Urano and E Douple vol. 3 pp. 1–14 (Zeist, The Netherlands: VSP)

Hand J W, Van Leeuwen G M J, Mizushina S, Van de Kamer J B, Maruyama K, Sugiura T, Azzopardi D V and Edwards A D 2001 Monitoring of deep brain temperature in infants using multi-frequency microwave radiometry and thermal modelling *Physics in Medicine and Biology* **46** 1885–1903

Harima Y, Nagata K, Harima K, , Ostapenko V V, Tanaka Y and Sawada S 2001 A randomised clinical trial of radiation therapy versus thermoradiotherapy in stage IIIB cervical carcinoma *International Journal of Hyperthermia* **17** 97–105

Harima Y, Nagata K, Harima K, Atsutoshi O, Ostapenko V V, Shikata N, Ohnishi T and Tanaka Y 2000 Bax and Bcl-2 protein expression following radiation therapy versus radiation plus thermoradiotherapy in stage IIIb cervical carcinoma *Cancer* **88** 132–138

Hiraoka M, Jo S, Akuta K, Y Nishimura, Takahashi M and Abe M 1987 Radiofrequency capacitive hyperthermia for deep-seated tumours *Cancer* **60** 121–127

Hoffmann A L, De la Rosette J J and H Wijkstra 2000 Intraprostatic temperature monitoring during transurethral microwave thermotherapy: status and future developments *Journal of Endourology* **14** 637–642

Hornsleth S N 1996 *Radiofrequency regional hyperthermia* Ph.D. thesis Aalborg University

Hornsleth S N, Mella O and Dahl O 1996 A new CT segmentation algorithm for finite difference based treatment planning systems in *Hyperthermic Oncology 1996*, eds. C Franconi, G Arcangeli and R Cavaliere vol. 2 pp. 521–523 Rome, Italy Tor Vergata

Hynynen K 1995 Ultrasound heating technology in *Thermoradiotherapy and Thermochemotherapy: Biology, Physiology and Physics*, eds. M H Seegenschmiedt, P Fessenden and C C Vernon vol. 1 pp. 253–277 (Berlin, Germany: Springer-Verlag)

Jackson J D 1975 *Classical Electrodynamics* (John Wiley & Sons) 2nd edn.

Jacobsen S and Staufer P 2002 Non-invasive temperature profile estimation in a lossy medium based on multi-band radiometric signals sensed by a microwave dual-purpose body-contacting antenna *International Journal of Hyperthermia* **18** 86–103

James B J and Sullivan D M 1992 Creation of three-dimensional patient models for hyperthermia treatment planning *IEEE Transactions on Biomedical Engineering* **39** 238–242

Jia X, Paulsen K D, Buechler D N, Gibbs, Jr F A and Meaney P M 1994 Finite element simulation of Sigma 60 heating in the Utah phantom: computed and measured data compared *International Journal of Hyperthermia* **10** 755–774

Johnson C C and Guy A W 1972 Nonionizing electromagnetic wave effects in biological materials and systems *Proceedings of the IEEE* **60** 692–718

Kato H, Hiraoka M, Nakajima T and Ishada T 1985 Deep-heating characteristics of an RF capacitive heating device *International Journal of Hyperthermia* **1** 15–28

Kato H, Hyodo K, Akassa N, Nishimura K, Uchida N, Kasai T and Sugimura K. 1997 Optimization of bolus for capacitive type heating *Japanese Journal of Hyperthermic Oncology* **13** 10–17 (Japanese)

Konings A W 1995 Interaction of heat and radiation *in vitro* and *in vivo* in *Thermoradiotherapy and Thermochemotherapy: Biology, Physiology and Physics*, eds. M H Seegenschmiedt, P Fessenden and C C Vernon vol. 1 pp. 89–102 (Berlin, Germany: Springer-Verlag)

Kosaka K, Imada H, Tomimatsu A, Nomoto S, Kusano S, Ostapenko V V and Terashima H 1999 Effectiveness of body earthing in hyperthermia using an 8 MHz RF capacitive heating device *Japanese Journal of Hyperthermic Oncology* **15** 1–7

Kotte A N T J 1998 *Design of a numerical model describing the heat transfer of vascular trees* Ph.D. thesis Utrecht University

Kotte A N T J, Van Leeuwen G M J, De Bree J, Van der Koijk J F, Crezee J and Lagendijk J J W 1996 A description of discrete vessel segments in thermal modelling of tissues *Physics in Medicine and Biology* **41** 865–884

Kotte A N T J, Van Leeuwen G M J and Lagendijk J J W 1999 Modelling the thermal impact of a discrete vessel tree *Physics in Medicine and Biology* **44** 57–74

Lagendijk J J W 2000 Hyperthermia treatment planning *Physics in Medicine and Biology* **45** R61–R76 topical review

Lagendijk J J W, Crezee J and Mooibroek J 1995a Principles of treatment planning in *Thermoradiotherapy and Thermochemotherapy: Biology, Physiology and Physics*, eds. M H Seegenschmiedt, P Fessenden and C C Vernon vol. 1 pp. 439–452 (Berlin, Germany: Springer-Verlag)

Lagendijk J J W and De Leeuw A A C 1986 The development of applicators for deep-body hyperthermia in *Recent Results in Cancer Reserach* pp. 18–35 (Springer Verlag)

Lagendijk J J W, Van Rhoon G C, Hornsleth S N, Wust P, De Leeuw A A C, Schneider C J, Van Dijk J D P, Van der Zee J, Van Heek-Romanowski R, Rahman S A and Gromoll C 1998 ESHO quality assurance guidelines for regional hyperthermia *International Journal of Hyperthermia* **14** 125–133

Lagendijk J J W, Visser A G, Kaatee R S J P, Crezee J, Van der Koijk J F, De Bree J, Kotte A N T J, Kanis A P, Kroeze H, Levendag P C and Battermann J J 1995b Interstitial hyperthermia and treatment planning: the 27 MHz multi-electrode current source method *Activity International Nucletron-Oldelft Radiotherapy Journal* **Special Report** 83–90

Lang J, Erdmann B and Seebass M 1999 Impact of nonlinear heat transfer on temperature control in regional hyperthermia *IEEE Transactions on Biomedical Engineering* **46** 1129–1138

Lee C K, Song C W, Rhee J G, Foy J A and Levitt S H 1995 Clinical experience using 8 MHz Radiofrequency capacitive hyperthermia in combination with radiotherapy: results of a phase I/II study *International Journal of Radiation Oncology, Biology and Physics* **32** 733–745

Lee E R 1995 Electromagnetic superficial heating technology in *Thermoradiotherapy and Thermochemotherapy: Biology, Physiology and Physics*, eds. M H Seegenschmiedt, P Fessenden and C C Vernon vol. 1 pp. 193–217 (Berlin, Germany: Springer-Verlag)

Mack C F, Stea B, Kittelson J M, Shimm D S, Sneed P K, Phillips T L, Swift P S, Luk K, Vora N, Stauffer P R *et al.* 1993 Interstitial thermoradiotherapy wit ferromagnetic implants for locally advanced and recurrent neoplasms *International Journal of Radiation Oncology, Biology and Physics* **27** 109–115

McGough R J, Ebbini E S and Cain C A 1992 Direct computation of ultrasound phased-array driving signals from a specified temperature distribution for hyperthermia *IEEE Transactions on Biomedical Engineering* **39** 825–835

Mooibroek J, Crezee J and Lagendijk J J W 1993 Thermal modeling of vascular patterns and their impact on interstitial heating technology and temperature monitoring in *Interstitial and Intracavitary Thermoradiotherapy*, eds. M H Seegenschmiedt and R Sauer pp. 131–137 (Berlin, Germany: Springer-Verlag)

Murata T, Akagi K, Ostapenko V V, Isoda H, Nagata K, Nasu R, Shiga T, Tanaka Y and Yamamoto I 1998 Relevance of a new impedance matching, or subtrap method for the reduction of pain during hyperthermia *Acta Oncologica* **37** 485–488

Nikita K S, Maratos N G and Uzunoglu 1993 Optimal steady-state temperature distribution for a phased array hyperthermia system *IEEE Transactions on Biomedical Engineering* **40** 1299–1306

Nomoto S, Imada H, Tomimatsu A, Kosaka K, Kusano S, Ostapenko V V and Terashima H 1999 Side effects of Hyperthermia for intrathorac tumors using an 8 MHz RF capacitive heating device *Japanese Journal of Hyperthermic Oncology* **15** 9–14

Oleson J R, Samulski T V, Leopold K A, Clegg S T, Dewhirst M W, Dodge R K and George S L 1993 Sensitivity of hyperthermia trial outcomes to temperature and time: implications for thermal goals of treatment *International Journal of Radiation Oncology, Biology and Physics* **25** 289–297

Omiya M, Hikage T, Ohno N, Horiguchi K and Itoh K 1998 Design of cavity-backed slot antennas using the finite-difference time-domain technique *IEEE Transactions on Antennas and Propagation* **46** 1853–1858

Orcutt N and Gandhi O P 1990 Use of the impedance method to calculate 3-D power deposition patterns for hyperthermia with capacitive plate electrodes *IEEE Transactions on Biomedical Engineering* **37** 36–43

Overgaard J, Gonzalez-Gonzalez D, Hulshof M C C M, Arcanangeli G, Dahl O, Mella O and Bentzen S M 1995 Randomised trial of hyperthermia as adjuvant to radiotherapy for recurrent or metastatic malignant melanoma *Lancet* **345** 540–543

Paulsen K D 1990 Calculation of power deposition patterns in hyperthermia in *Thermal Dosimetry and Treatment Planning*, ed. M Gautherie Clinical Thermology, Subseries Thermotherapy pp. 57–117 (Berlin, Germany: Springer-Verlag)

Paulsen K D, Geimer S, Tang J and Boyse W E 1999 Optimization of pelvic heating rate distributions with electromagnetic phased arrays *International Journal of Hyperthermia* **15** 157–186

Paulsen K D and Ross M P 1990 Comparison of numerical calculations with phantom experiments and clinical measurements *International Journal of Hyperthermia* **6** 333–349

Paulsen K D, Strohbehn J W and Lynch D R 1984 Theoretical temperature distributions produced by an annular phased array-type system in CT-based patient models *Radiation Research* **100** 536–552

Peller M, Baur A, Löffler R, Turner P, Futschik G, Abdel-Rahman S, Santl M, Issels R and Reiser M 2000 Simultaneous mr Imaging and T1-relaxation time determination during regional hyperthermia in *ICHO-2000: Abstracts* p. 239 Kyŏngju, South-Korea International Congress of Hyperthermic Oncology

Pennes H H 1948 Analysis of tissue and arterial blood temperature in the resting human forearm *Journal of Applied Physiology* **1** 93–122

Piket-May M, Taflove A and Baron J 1994 FD-TD modeling of digital signal propagation in 3-D circuits with passive and active loads *IEEE Transactions on Microwave Theory and Technique* **42** 1514–1523

Press W H, Flannery B P, Teukolsky S A and Vetterling W T 1988 *Numerical Recipes in C* (Cambridge, USA: Cambridge University Press)

Prionas S D, Fessenden P, Kapp D S, Goffinet D R and Hahn G M 1989 Interstitial electrodes allowing longitudinal control of SAR distributions in *Hyperthermic Oncology 1988*, eds. T Sugahara and M Saito vol. 2 pp. 707–710 (London, UK: Taylor & Francis)

Prionas S D, Kapp D S, Goffinet D R, Ben-Yosef R, Fessenden P and Bagshaw M A 1994 Thermometry of interstitial hyperthermia given as an adjuvant to brachytherapy for the treatment of carcinoma of the prostate *International Journal of Radiation Oncology, Biology and Physics* **28** 151–162

Raaymakers B W, Kotte A N T J and Lagendijk J J W 2000 How to apply a discrete vessel model in thermal simulations when only incomplete vessel data is available *Physics in Medicine and Biology* **45** 3385–3401

Raaymakers B W, Van Vulpen M, Lagendijk J J W, De Leeuw A A C, Crezee J and Battermann J J 2001 Determination and validation of the actual 3D temperature distribution during interstitial hyperthermia of prostate carcinoma *Physics in Medicine and Biology* **46** 3115–31

Raskmark P 1995 Power amplifier design using quadrature hybrids *RF Design* **1995-6** 70–74

Raskmark P, Hornsleth S N, Salling L N, Lindegaard J C and Overgaard J 1994a Deep heating using a movable applicator phased array hyperthermia system. a pre-clinical feasibility study *Acta Oncologica* **33** 451–455

Raskmark P, Larsen T and Hornsleth S N 1994b Multi-applicator hyperhermia system description using scattering parameters *International Journal of Hyperthermia* **10** 143–151

Rau B, Wust P, Hohenberger P, Loffel J, Hunerbein M, Below C, Gellermann J, Speidel A, Vogl T, Riess H, Felix R and Schlag P M 1998 Preoperative hyperthermia combined with radiochemotherpay in locally advanced rectal cancer *Annals of Surgery* **227** 380–389

Rhee J G, Lee C K K, Osborn J, Levitt S H and Song C W 1991 Precooling prevents overheating of subcutaneous fat in the use of RF Capacitive heating *International Journal of Radiation Oncology, Biology and Physics* **20** 1009–1015

Rietbroek R C, Bakker P J M, Schilthuis M S, Postma A J, Zum Vörde Sive Vörding P J, Gonzalèz Gonzalèz D, Kurth K H, Bakker A J and Veenhof C H N 1996 Feasibility, toxicity, and preliminary results of weekly loco-regional hyperthermia and cisplatin in patients with previously irradiated recurrent cervical carcinoma or locally advanced bladder cancer *International Journal of Radiation Oncology, Biology and Physics* **34** 887–893

Rietbroek R C, Schilthuis M S, Bakker P J M, Van Dijk J D, Postma A J, Gonzalèz Gonzalèz D, Bakker A J, Van der Velden J, Helmerhorst T J and Veenhof C H N 1997 Phase ii trial of weekly locoregional hyperthermia and cisplatin in a previously irradiated recurrent carcinoma of the uterine cervix *Cancer* **79** 935–943

Rietveld P M J, Van de Kamer J B, Van der Zee J, Hornsleth S N and Van Rhoon G C 2000 Influence of variations in position, form and contents of semi-simple phantoms in the BSD-2000 Sigma-60 applicator on SAR distributions in *ICHO-2000: Abstracts* p. 145 Kyŏngju, South-Korea International Congress of Hyperthermic Oncology

Robins H I, Rushing D, Kutz M, Tutsch K D, Tiggelaar C L, Paul D, Spriggs D, Kraemer C, Gillis W, Feierabend C, Arzoomanian R Z, Longo W, Alberti D, d'Oleire F, Qu R P, Wilding G and Stewart J A 1997 Phase I clinical trial of melphalan and 41.8 degrees C whole-body hyperthermia in cancer patients *Journal of Clinical Oncology* **15** 158–164

Ryan T P 1991 Comparison of six microwave antennas for hyperthermia treatment of cancer: SAR results for single antennas and arrays. *International Journal of Radiation Oncology, Biology and Physics* **21** 403–413

Ryan T P, Trembly B S, Roberts D W, Strohbehn J W, Coughlin C T and Hoopes P J 1994 Brain hyperthermia: I. Interstitial microwave antenna array techniques–the Darthmouth experience *International Journal of Radiation Oncology, Biology and Physics* **29** 1065–1078

Schneider C J, Van Dijk J D P, De Leeuw A A C, Wust P and Baumhoer W 1994 Quality assurance in various radiative hyperthermia systems applying a phantom with LED matrix *International Journal of Hyperthermia* **10** 733–747

Schreier K, Budihna M, Lesnicar H, Handl-Zeller L, Hand J W, Prior M V, Clegg S T and Brezovich I A 1990 Preliminary studies of interstitial hyperthermia using hot water *International Journal of Hyperthermia* **6** 431–444

Seebass M, Beck R, Gellermann J, Nadobny J and Wust P 2001 Electromagnetic phased arrays for regional hyperthermia: optimal frequency and antenna arrangement *International Journal of Hyperthermia* **17** 321–36

Seegenschmiedt M H, Martus P, Fietkau R, Iro H, Brady L W and Sauer R 1994 Multivariate analysis of prognostic parameters using interstitial thermoradiotherapy (IHT-IRT): tumor and treatment variables predict outcome *International Journal of Radiation Oncology, Biology and Physics* **29** 1049–1063

Seip R and Ebbini E S 1995 Nonivasive estimation of tissue temperature response to heating fields using diagnostic ultrasound *IEEE Transactions on Biomedical Engineering* **42** 828–839

Sneed P K, Dewhirst M W, Samulski T, Blivin J and Prosnitz L R 1998 Should interstitial thermometry be used for deep hyperthermia? *International Journal of Radiation Oncology, Biology and Physics* **40** 1015–1017

Song C W, Rhee J G, Lee C K K and Levitt 1986 Capacitive heating of phantom and human tumors with an 8 MHz Radiofrequency applicator (Thermotron RF-8) *International Journal of Radiation Oncology, Biology and Physics* **12** 365–372

Sowinski M J and Van den Berg P M 1990 A three-dimensional iterative scheme for an electromagnetic capacitive applicator *IEEE Transactions on Biomedical Engineering* **37** 975–986

Stauffer P R, Cetas T C and Jones R C 1984 Magnetic induction heating of ferromagnetic implants for inducing localized hyperthermia in deep seated tumors *IEEE Transactions on Biomedical Engineering* **31** 235–251

Stogryn A 1971 Equations for calculating the dielectric constant of saline water *IEEE Transactions on Microwave Theory and Technique* **19** 733–736

Sullivan D M 1991 Mathematical methods for treatment planning in deep regional hyperthermia *IEEE Transactions on Microwave Theory and Technique* **39** 864–872

Sullivan D M, Ben-Yosef R and Kapp D S 1993 Stanford 3D hyperthermia treatment planning system. Technical review and clinical summary *International Journal of Hyperthermia* **9** 627–643

Sullivan D M, Buechler D and Gibbs F A 1992 Comparison of measured and simulated data in an annular phased array using an inhomogeneous phantom *IEEE Transactions on Microwave Theory and Technique* **40** 600–604

Taflove A 1995 *Computational Electrodynamics, The Finite-Difference Time-Domain Method* (Boston, USA: Artech House)

Tanaka H, Kato H, Nishida T, Kano E, Sugahara T and Ishida T 1981 Physical basis of RF hyperthermia for cancer therapy (2) Measurement of distribution of absorbed power from radiofrequency exposure in agar phantom *Journal of Radiation Research* **22** 101–108

Tomimatsu A, Imada H, Kosaka K, Nomoto S, Kusano S, Ostapenko V V and Terashima H 1999a Advantage of an external cooling unit in deep hyperthermia using an 8 MHz RF capacitive heating device *Japanese Journal of Hyperthermic Oncology* **15** 65–70

Tomimatsu A, Imada H, Kosaka K, Nomoto S, Kusano S, Ostapenko V V and Terashima H 1999b Refinement of circulating liquid of overlay bolus in hyperthermia using an 8 MHz RF capacitive heating device *Japanese Journal of Hyperthermic Oncology* **15** 71–77

Tsuda N, Koruda K and Y Suzuki 1996 An inverse method to optimize heating conditions in RF-capacitive hyperthermia *IEEE Transactions on Biomedical Engineering* **43** 1029–1037

Turner P F 1984 Regional hyperthermia with an annular phased array *IEEE Transactions on Biomedical Engineering* **31** 106–114

Turner P F 1999 Dodek 12 chanel solid state amplifier with the BSD-2000-3D hyperthermia system in *ESHO-99: Abstracts* p. 76 Rotterdam, The Netherlands ESHO

Turner P F and Schaeffermeyer T 1989 BSD-2000 approach for deep local and regional hyperthermia *Strahlentherapie und Onkologie* **165** 738–741

Turner P F, Youd T, Lauritzen R, Latta M, Ellis D, Schaefermeyer T, Hanka S and Terry P 2000 Deep heating EM phased array BSD-2000-3D with an elliptical dipole array in *ICHO-2000: Abstracts* p. 130 Kyong-Ju, Korea ICHO

Van de Kamer J B, De Leeuw A A C, Hornsleth S N, Kroeze H, Kotte A N T J and Lagendijk J J W 2001a Development of a regional hyperthermia treatment planning system *International Journal of Hyperthermia* **17** 207–220

Van de Kamer J B, De Leeuw A A C, Kroeze H and Lagendijk J J W 2001b Quasistatic zooming for regional hyperthermia treatment planning *Physics in Medicine and Biology* **46** 1017–1030

Van de Kamer J B, Kroeze H, De Leeuw A A C and Lagendijk J J W 2001c Quasistatic zooming of FDTD $\vec{E}$-field computations: The impact of down-scaling techniques *Physics in Medicine and Biology* **46** 1539–1551

Van de Kamer J B, Lagendijk J J W, De Leeuw A A C and Kroeze H 2001d High-resolution SAR modelling for regional hyperthermia: Testing quasistatic zooming at 10 MHz *Physics in Medicine and Biology* **46** 183–196

Van de Kamer J B, Van Vulpen M, De Leeuw A A C, Kroeze H and Lagendijk J J W 2002a CT-resolution regional hyperthermia treatment planning *International Journal of Hyperthermia* **18** 104–116

Van de Kamer J B, Van Vulpen M, De Leeuw A A C, Kroeze H and Lagendijk J J W 2002b CT-resolution regional hyperthermia treatment planning *International Journal of Hyperthermia* **18** 104–116

Van de Kamer J B, Van Wieringen N, De Leeuw A A C and Lagendijk J J W 2001e The significance of accurate dielectric tissue data for hyperthermia treatment planning *International Journal of Hyperthermia* **17** 123–142

Van der Houwen E B 1999 *Ergonomisch en constructief conceptontwerp van een klinisch regionaal open bolus hyperthermiesysteem* Master's thesis Faculty of Industrial Design, Technical University Delft (Dutch)

Van der Koijk J F 1997 *The MECS-IHT system* Ph.D. thesis Utrecht University, the Netherlands

Van der Koijk J F, Crezee J, Van Leeuwen G M J, Battermann J J and Lagendijk J J W 1996 Dose uniformity in MECS interstitial hyperthermia: the impact of longitudinal control in model anatomies *Physics in Medicine and Biology* **41** 429–444

Van der Koijk J F, Lagendijk J J W, Crezee J, De Bree J, Kotte A N T J, Van Leeuwen G M J and Battermann J J 1997 The influence of vasculature on temperature distributions in MECS interstitial hyperthermia: importance of longitudinal control *International Journal of Hyperthermia* **13** 365–385

Van der Zee J 2001 personal communication

Van der Zee J and Gonzalez Gonzalez D 2002 The Dutch deep hyperthermia trial: results in cervical cancer *International Journal of Hyperthermia* **18** 1–12

Van der Zee J, Gonzalez Gonzalez D, Van Rhoon G C, Van Dijk J D P, Van Putten W L J and Hart A A M 2000 Comparison of radiotherapy alone with radiotherapy plus hyperthermia in locally advanced pelvic tumours: a prospective, randomised, multicentre trial *The Lancet* **355** 1119–1125

Van Dijk J D P, Gonzalez-Gonzalez D and Blank L E C M 1989 Deep local hyperthermia with a four aperture array system of large waveguide radiators. Results of simulation and clinical application in *Hyperthermic Oncology 1988*, eds. T Sugahara and M Saito vol. 1 Summary Papers pp. 573–575 London, UK Taylor & Francis

Van Es C A, Wijrdeman H K, De Leeuw A A C, Mooibroek J, Lagendijk J J W and Battermann J J 1995 Regional hyperthermia of pelvic tumours using the Utrecht Coaxial TEM system: a feasibility study *International Journal of Hyperthermia* **11** 173–186

Van Leeuwen G M J, Hand J W, Mizushina S, Van de Kamer J B and Edwards A D 2000a Retrieval of brain temperatures from radiometric brightness temperature measurements using 3-D EM and thermal modelling in *Proceedings Third International Conference on Bioelectromagnetism* pp. 135–136 Bled, Slovenia International Society for Bioelectromagnetism

Van Leeuwen G M J, Kotte A N T J, Raaymakers B W and Lagendijk J J W 2000b Temperature simulations in tissue with a realistic computer generated vessel network *Physics in Medicine and Biology* **45** 1035–1049

Van Leeuwen G M J, Lagendijk J J W, Van Leersum B J A M, Zwamborn A P M, Hornsleth S N and Kotte A N T J 1999 Calculation of change in brain temperatures due to exposure to a mobile phone *Physics in Medicine and Biology* **44** 2367–2379

Van Rhoon G C, Van der Zee J, Broekmeyer-Reurink M P, Visser A G and Reinhold H S 1992 Radiofrequency capacitive heating of deep-seated tumours using pre-cooling of the subcutaneous tissues: results on thermometry in Dutch patients *International Journal of Hyperthermia* **8** 843–854

Van Vulpen M, De Leeuw A A C, Hofman P, Van de Kamer J B, Boon T A, Battermann J J and Lagendijk J J W 2000 Regional hyperthermia combined with external beam radiotherapy for T3 and T4a prostate carcinoma, a feasibility study in *ICHO-2000: Abstracts* p. 213 Kyŏngju, South-Korea International Congress for Hyperthermic Oncology

Van Vulpen M, De Leeuw A A C, Van de Kamer J B, Kroeze H, Boon T A, Wárlám-Rodenhuis C C, Lagendijk J J W and Battermann J J 2002a Regional Hyperthermia combined with radiotherapy for locally advanced prostate carcinoma, a feasibility study with special attention to the use of invasive thermometry *International Journal of Hyperthermia* (submitted)

Van Vulpen M, Raaymakers B W, De Leeuw A A C, Van de Kamer J B, Van Moorselaar R J A, Hobbelink M G G, Battermann J J and Lagendijk J J W 2002b Prostate perfusion in patients with locally advanced prostate carcinoma, measured during different hyperthermia techniques *Journal of Urology* (accepted)

Van Vulpen M, Raaymakers B W, Lagendijk J J W, Crezee J, De Leeuw A A C, Van Moorselaar R J A, Ligtvoet C M and Battermann J J 2002c 3D controlled interstitial hyperthermia combined with radiotherapy for locally advanced prostate carcinoma, a feasibility study *International Journal of Radiation Oncology, Biology and Physics* **53** 116–126

Van Wieringen N, Kotte A N T J, Van Leeuwen G M J, Lagendijk J J W, Van Dijk J D P and Nieuwenhuys G J 1998 Dose uniformity of ferromagnetic seed implants in tissue with discrete vasculature: a numerical study on the impact of seed characteristics and implantation techniques *Physics in Medicine and Biology* **43** 121–138

Van Wieringen N, van Dijk J D P, Nieuwenhuys G J, Snel C E and Cetas T C 1996 Power absorption and temperature control of multi-filament palladium-nickel thermoseeds for interstitial hyperthermia *Physics in Medicine and Biology* **41** 2367–2380

Van Wieringen N, van Dijk J D P, Van Veldhuizen J and Nieuwenhuys G J 1997 3-Dimensional temperature control of palladium-nickel thermoseeds: a computer aided and experimental evaluation *International Journal of Hyperthermia* **13** 269–286

Vernon C C, Hand J W, Field S B, Machin D, Whaley J B, Van der Zee J, Van Putten W L J, van Rhoon G C, van Dijk J D P, Gonzalez Gonzalez D, Liu F F, Goodman P and Sherar M 1996 Radiotherapy with or without hyperthermia in the treatment of superficial localised breast cancer: results from five randomised controlled trials *International Journal of Radiation Oncology, Biology and Physics* **35** 731–744

Webb S 1998 *The physics of medical imaging* Medical Sience Series (Bristol, UK: IOP Publishing Ltd)

Westermann A M, Grosen E A, Katschinski D M, Jager D, Rietbroek R, Schink J C, Tiggelaar C L, Jager E, Zum Vorde sive Vording P, Neuman A, Knuth A, Van Dijk J D, Wiedemann

G J and Robins H I 2001 A pilot study of whole body hyperthermia and carboplatin in platinum-resistant ovarian cancer *European Journal of Cancer* **37** 1111–1117

Wiersma J, Van Dijk J D P, Sijbrands J and Schneider C J 1998 The measurement of fringing fields in a radio-frequency hyperthermia array with emphasis on bolus size *International Journal of Hyperthermia* **14** 535–551

Wlodarczyk W, Boroschewski R, Hentschel M, Wust P, Monich G and Felix R 1998 Three-dimensional monitoring of small temperature changes for therapeutic hyperthermia using MR *Journal of Magnetic Resonance Imaging* **8** 165–174

Wlodarczyk W, Hentschel M, Wust P, Noeske R, Hosten R, Rinneberg H and Felix R 1999 Comparison of four magnetic resonance methods for mapping small temperature changes *Physics in Medicine and Biology* **44** 607–624

Wlodarczyk W, Wust P, Fähling H, Nadobny J, Auer G, Mönich G and Felix R 1997 Short antennas as radiating elements for segmented phased-array hyperthermia system in *ESHO-97: Abstracts* p. 81 Berlin, Germany European Society for Hyperthermic Oncology

Wust P, Fähling H, Gellermann J, Wlodarczyk W, Seebass M, Nadobny J and Felix R 2000 The next technological step in hyperthermia - are we succesfull in *ICHO-2000: Abstracts* p. 146 Kyŏngju, South-Korea International Congress of Hyperthermic Oncology

Wust P, Fähling H, Helzel T, Kniephoff M, Wlodarczyk W, G Mönich and Felix R 1998a Design and test of a new multi-amplifier system with phase and amplitude control *International Journal of Hyperthermia* **14** 459–477

Wust P, Nadobny J, Seebass M, Dohlus J M, John W and Felix R 1993 3-D computation of E fields by the volume-surface integral equation (VSIE) method in comparison with the finite-integration theory (FIT) method *IEEE Transactions on Biomedical Engineering* **40** 745–759

Wust P, Nadobny J, Seebass M, Stalling D, Gellermann J, Hege H C, Deuflhard P and Felix R 1999 Influence of patient models and numerical methods on predicted power deposition patterns *International Journal of Hyperthermia* **15** 519–540

Wust P, Rau B, Gellerman J, Pegios W, Loffel J, Riess H, Felix R and Schlag P M 1998b Radiochemotherapy and hyperthermia in the treatment of rectal cancer. *Recent Results in Cancer Research* **146** 175–191

Wust P, Seebass M, Nadobny J, Deuflhard P, G Mönich and Felix R 1996 Simulation studies promote technological development of radiofrequency phased array hyperthermia *International Journal of Hyperthermia* **12** 477–494

Yee K S 1966 Numerical solutions of initial boundary value problems involving Maxwell's equations in isotropic media *IEEE Transactions on Antennas and Propagation* **14** 302–307

Zwamborn A P M, Van den Berg P M and Koenis F T C 1991 *Computation of the electromagnetic field distribution inside 3-D biological tissue using the weak form of the Conjugate Gradient FFT method* chap. 4.1, pp. 30–37 no. 7 in Hyperthermia Bulletin (Amsterdam: Radiotherapy Department, Academisch Medisch Centrum)

Publications

Full papers

- Kroeze H 1994 RC active filters *Elector* **20-6** 22–24
- Kroeze H 1995 Filtres passe-bas réalisés à l'aide de condensateurs de la série E12 *Elector (France)* **18-9** 24–27
- Kroeze H, Van Vulpen M, De Leeuw A A C, Van de Kamer J B and Lagendijk J J W 2001 The use of absorbing structures during regional hyperthermia treatment *International Journal of Hyperthermia* **17** 240–257
- Kroeze H, Van de Kamer J B, De Leeuw A A C and Lagendijk J J W 2001 Regional hyperthermia applicator design using FDTD modelling *Physics in Medicine and Biology* **46** 1919–1935
- Kroeze H, Van de Kamer J B, De Leeuw A A C, Kikuchi M and Lagendijk J J W 2002 Treatment planning for capacitive regional hyperthermia *International Journal of Hyperthermia* **(in press)**
- Kroeze H, Kokubo M, Van de Kamer J B, De Leeuw A A C, Kikuchi M, Hiraoka M and Lagendijk J J W 2002 Comparison of a capacitive and a cavity slot radiative applicator for regional hyperthermia *Japanese Journal of Hyperthermic Oncology* **18(2)** 75–91
- Kroeze H, Van Vulpen M, De Leeuw A A C, Van de Kamer J B and Lagendijk J J W 2002 Improvement of absorbing structures used in regional hyperthermia *International Journal of Hyperthermia* **(submitted)**

- Gussenhoven E J, Van der Lugt A, Van Streijen M, Li W, Kroeze H, The S H K, Van Egmond F C, Honkoop J, Peters R J G, De Feyter P J, Van Urk H and Pieterman H 1993 Displacement sensing device enabling accurate documentation of catheter top position in *Intravascular ultrasound*, eds. J Roelandt, E J Gussenhoven and N Bom vol. 1 pp. 157–162 (Kluwer)
- Lagendijk J J W, Visser A G, Kaatee R S J P, Crezee J, Van der Koijk J F, De Bree J, Kotte A N T J, Kanis A P, Kroeze H, Levendag P C and Battermann J J 1995 Interstitial hyperthermia and treatment planning: the 27 MHz multi-electrode current source method *Activity International Nucletron-Oldelft Radiotherapy Journal* **Special Report** 83–90
- Van de Kamer J B, De Leeuw A A C, Hornsleth S N, Kroeze H, Kotte A N T J and Lagendijk J J W 2001 Development of a regional hyperthermia treatment planning system *International Journal of Hyperthermia* **17** 207–220

- Van de Kamer J B, Lagendijk J J W, De Leeuw A A C and Kroeze H 2001 High-resolution SAR modelling for regional hyperthermia: Testing quasistatic zooming at 10 MHz *Physics in Medicine and Biology* **46** 183–196
- Van de Kamer J B, De Leeuw A A C, Kroeze H and Lagendijk J J W 2001 Quasistatic zooming for regional hyperthermia treatment planning *Physics in Medicine and Biology* **46** 1017–1030
- Van de Kamer J B, Kroeze H, De Leeuw A A C and Lagendijk J J W 2001 Quasistatic zooming of FDTD $\vec{E}$-field computations: The impact of down-scaling techniques *Physics in Medicine and Biology* **46** 1539–1551
- Van de Kamer J B, Van Vulpen M, De Leeuw A A C, Kroeze H and Lagendijk J J W 2002 CT-resolution regional hyperthermia treatment planning *International Journal of Hyperthermia* **18** 104–116
- Van Vulpen M, De Leeuw A A C, Van de Kamer J B, Kroeze H, Boon T A, Wárlám-Rodenhuis C C, Lagendijk J J W and Battermann J J 2002 Regional Hyperthermia combined with radiotherapy for locally advanced prostate carcinoma, a feasibility study with special attention to the use of invasive thermometry *International Journal of Hyperthermia* (**submitted**)

Dankwoord

Op de laatste pagina's van dit boekje wil ik graag iedereen bedanken die mij de afgelopen jaren op enige wijze heeft gesteund bij het wordingsproces ervan.

Allereerst mijn promotor Jan Lagendijk, die, toen ik ooit voorzichtig informeerde of ik misschien in aanmerking zou kunnen komen voor een AIO-plaats, minder aarzeling vertoonde dan ikzelf. Ook op momenten van grote existentiële twijfels kon ik altijd bij hem terecht voor een zelfverzekerde duw in de goede richting. Mijn bewondering is groot voor de rol die hij speelt in de internationale hyperthermie wereld en zijn grote creativiteit in het vergaren van de financiële middelen voor het hyperthermie onderzoek.

Kees Ligtvoet moet worden beschouwd als de eigenlijke initiator van mijn promotieonderzoek. Al sinds zijn komst naar Utrecht heeft hij mij aangemoedigd verder te kijken dan de projecten van de Instrumentele Dienst. Ik ben dan ook zeer gelukkig hem, samen met Joost Ansems, aan mijn zijde te hebben als paranimf. Dit ondanks ons fundamenteel verschil van inzicht over het Nederlandse voetbal.

Astrid de Leeuw wil ik bedanken voor de grote vasthoudendheid en het vele geduld dat zij heeft betoond bij haar moeilijke taak om een eigenwijze technicus om te scholen tot onderzoeker en klinisch hyperthermist. Jeroen van de Kamer heeft veel bijgedragen aan dit boekje door talrijke discussies en het kritisch lezen van mijn manuscripten. Tevens was hij een veelgebruikte vraagbaak voor 'kleine' C^{++} en LaTeX 2_ε vraagjes. In Nico van den Berg heeft het hyperthermieteam een gewaardeerde uitbreiding gevonden.

Van Carla Wárlám en Marco van Vulpen heb ik veel geleerd over de klinische aspecten van de hyperthermiebehandeling. Deze behandelingen zouden niet mogelijk zijn geweest zonder de hulp van achtereenvolgens Geralda, Natasja, Andrea en Heleen. Met Marco kon ik bovendien steeds een prettige discussie voeren over onze wederzijdse concept-artikelen.

Met Aart Nederveen heb ik de afgelopen jaren een werkkamer gedeeld. Naast het delen van het promotieleed hadden we vele discussies over meer meta-fysische zaken. Jammer genoeg gaat Aart vertrekken naar de het Bijvoetcentrum.

Bas Raaymakers was de meest uitgesproken exponent van het 'jonge honden' team, die deze 'old dog' toch als paranimf koos. Die HuBa buggy of de onoverwinnelijke War Robot moeten we toch nog eens bouwen. Met de overige ganggenoten Marion van Gellekom, Eleftheria Astreinidou, Bram van Asselen, Maria Sastre Padró, Martijn Ketelaars en (verdieping lager) Uulke vd. Heide, Rajko Topolnjak en Anna Petoukhova waren het steeds weer levendige lunches.

Hans Crezee was lange tijd mijn historisch klankbord, dat ik moest missen na zijn vertrek naar het AMC.

Met Jan Kok heb ik vele malen letterlijk onder hoogspanning gewerkt om de oude Henry generator aan de praat te houden. Al doende stookten we Kees Imhof en Erik Westzaan dagenlang hun werkkamer uit en bliezen we daar zelfs de drie-fase aansluiting op.

Ric Exterkate stond altijd klaar om netwerkprobleempjes op te lossen en zoekgeraakte files terug te vinden in het feilloze backup systeem. Alexis Kotte was een grote hulp bij $\LaTeX 2_\varepsilon$ en METAPOST problemen en het genereren van .gof files. Gijsbert Bol maakte het prachtige isoTool, dat gebruikt werd voor het omslag van dit boekje.

Jack de Koning sleepte voor mij een afgedankte waterbak met positioneringsmechanisme voor de poorten van hel weg, zodat ik eenvoudig antenne metingen kon uitvoeren.

My special thanks go to Waldemar Wlodarczyk and his invitation for me to visit the Berlin group. The meetings with (among others) Jacek Nanobny, Martin Seebass, Peter Wust and Horst Fähling were very instructive. Neither of them showed their bewilderment over my 'Steinkessel Deutsch'.

An accidental meeting with prof. Kikuchi at a Korean dinnertable, where he had to endure and even judge my karaoke singing, lead to the fruitful cooperation between him, Dr. Kokubo, prof. Kato and prof. Hiraoka and our group that resulted in the chapters on capacitive hyperthermia. The help of Masaki Kokubo was indispensable in the preparation of Chapter 6. I am looking forward to our continued cooperation.

Alle collega's van de dienst Medische Technologie en Multimedia (voorheen Instrumentele Dienst) bedankt voor de belangstelling en de steun met diverse kleine klusjes en (Han Essers) bestellingen. Ed Duiveman, Henk te Biesebeek, Erwin Bakker, Kees vd. Linden, Kees Machielse en Harry van Rossum leverden een grote bijdrage aan het Rasta project, waardoor 'de ton' een robuuste tuner verkreeg. Sander Terbruggen tekende figuur 5.1(b) en dacht, samen met Ward van der Houwen, mee over de toekomstige inrichting van hyperthermie applicatoren. Voorts de onmisbare werkgroep collegialiteit en de mechanische collega's, die ik ieder voorjaar weer lastig viel met niet nader te noemen somatische projecten.

Door de goede zorgen van Peter Driebergen van de Bike In (fietsenkelder AZU) bleven de tweewielers probleemloos rollen; zonder zijn telefoontjes om 16:50 uur had ik vaak zonder fiets gezeten.

Ik bedank mijn ouders voor het vele goede dat zij mij hebben meegeven en met name mijn moeder voor de vele steun en vrijheid die zij mij heeft geven tijdens mijn opleiding.

Ten slotte: dit proefschrift zou niet tot stand zijn gekomen zonder Marion, die mijn vele afwezigheid, letterlijk en figuurlijk, moest verdragen. Volgens haar was ik dan ook geen AIO maar een OLIO. Door mij veel uit handen te nemen kon ik mij goed concentreren op mijn onderzoek. Dat is nu voorbij, er breken andere tijden aan.

Curriculum Vitae

Hugo Kroeze werd op 4 augustus 1955 geboren te Naarden, volgde lager onderwijs aan de Marnixschool te Hilversum en behaalde in 1972 het MAVO diploma aan de Snellius MAVO te Hilversum. In 1977 behaalde hij het HTS diploma, afstudeerrichting Electrotechniek-Informatietransport aan de Chr. HTS te Hilversum. Het afstudeer onderzoek, uitgevoerd samen met ing. M. Doorn, betrof het ontwerp van een demonstratieapparaat voor Puls Code Modulatie, onder begeleiding van ir. V.H. Meyer en ir. M.A. Rakier. Van 1980 tot 1981 was hij tewerkgesteld als erkend gewetensbezwaarde militaire dienst bij het kinderrevalidatiecentrum 'de Trappenberg' te Huizen en werkte aan een project voor electronische communicatie hulpmiddelen voor dubbel gehandicapte kinderen met behulp van het Bliss symbolen systeem. Van 1981 tot heden is hij werkzaam bij de dienst Medische Technologie en Multimedia (voorheen Instrumentele Dienst) van het UMC Utrecht, afdeling ontwikkeling Electronica. Hij was o.a. verantwoordelijk voor het ontwerp van het 196 kanaals thermometrie systeem (De Leeuw *et al.*, 1993) en was projectleider van het ontwerp- en realisatie team van het Multi Electrode Current Source interstitieel hyperthermie systeem (Van der Koijk, 1997). Vanaf 1997 is hij gedetacheerd bij de afdeling Radiotherapie van het UMC Utrecht om te werken aan het NKB project 'Improvement of the Coaxial TEM Regional Hyperthermia system'. Dit onderzoek vormde de basis voor dit proefschrift.